TAMPEREEN TEKNILLINEN YLIOPISTO
TAMPERE UNIVERSITY OF TECHNOLOGY

Janne Honkakorpi

MEMS-based Motion State Estimation and Control of Hydraulic Manipulators

Julkaisu 1219 • Publication 1219

Tampere 2014

Tampereen teknillinen yliopisto. Julkaisu 1219
Tampere University of Technology. Publication 1219

Janne Honkakorpi

MEMS-based Motion State Estimation and Control of Hydraulic Manipulators

Thesis for the degree of Doctor of Science in Technology to be presented with due permission for public examination and criticism in Konetalo Building, Auditorium K1702, at Tampere University of Technology, on the 27th of June 2014, at 12 noon.

Tampereen teknillinen yliopisto - Tampere University of Technology
Tampere 2014

ISBN 978-952-15-3310-5 (printed)
ISBN 978-952-15-3327-3 (PDF)
ISSN 1459-2045

Abstract

This thesis considers the application of low-cost micro-electro-mechanical system (MEMS) inertial sensors to the motion state estimation and closed-loop motion control of heavy-duty hydraulic manipulators used in mobile machines. Currently, the sensor solutions potentially suitable for advanced robotic motion control, condition monitoring, and fault diagnostics systems suffer from poor performance and limited availability. This has hindered the ability of Finnish mobile machine manufacturers to differentiate themselves with innovative products and features on the increasingly competitive global market. Inertial sensors based on MEMS technology offer an attractive alternative to existing sensing solutions due to their low cost, low power requirements, small size, and straightforward surface installation capability. Although this technology has been widely available for some time now, MEMS inertial sensors have yet to be successfully applied on mobile machine manipulators on a larger scale, because the proper motion state estimation models and required signal processing methods are not generally known or well understood. The various error sources of the individual inertial measurements and the effects of accelerative motions are major contributing factors prohibiting the direct use of the sensor readings for feedback in a robotic motion control system, for example. Thus, the motivation for this thesis has been to develop a novel hydraulic manipulator motion state estimation approach based on low-cost MEMS inertial sensors, which can be applied on a large scale to existing mobile machines, and to provide the necessary real-time measurements for the aforementioned systems.

At its core, the motion state estimation approach proposed in this thesis is based on well-known rigid body motion kinematics, which are used to derive recursive forward kinematics of a generic serial link manipulator. The manipulator forward kinematics are coupled with complementary filtering, which is a powerful signal processing method ideally suited for the fusion of relatively low-resolution inertial measurements. This forms the theoretical basis for producing low-delay, low-noise smoothed estimates of the manipulator motion states with MEMS inertial sensors. The proposed motion state estimation model is experimentally verified on a small-scale test bench, after which it is evaluated as an integral part of the closed-loop

motion control system on a full-size heavy-duty hydraulic manipulator. Comparative results are obtained using very accurate, high-resolution, and high-cost incremental encoders as reference sensors on the manipulator joints.

This thesis shows that by combining rigid body motion kinematics with an understanding of efficient yet straightforward signal processing methods, even low-cost and relatively low-resolution components can be used to create an innovative solution for hydraulic manipulator motion state sensing. This is a clear advantage over traditional sensor solutions, which are typically difficult to install, prone to failure, and incur high design and manufacturing costs. The novel technology developed in this thesis is expected to provide Finnish mobile machine manufacturers a substantial operational advantage in after-sales services and maintenance markets.

Preface

This study was carried out at the Department of Intelligent Hydraulics and Automation (IHA) at Tampere University of Technology (TUT).

I would like to express my sincere gratitude to Prof. Jouni Mattila for his support, guidance, and valuable comments during the course of this thesis process. I would also like to thank the Head of IHA, Prof. Kalevi Huhtala, for providing the laboratory facilities necessary for this study. The comments and criticism of the preliminary examiners, Dr. Marcus Rösth and Prof. Dr. Jonas Buchli as well as the suggestions by Prof. Jouko Halttunen are greatly appreciated.

I am grateful to the staff of IHA as a whole, and particularly to the laboratory staff for their invaluable help with the experimental installations. I would especially like to thank research fellow Juho Vihonen from the Department of Signal Processing (DSP) for the team work and constructive criticism which significantly contributed towards the completion of this thesis. Thanks are also due to researchers Tuomo Kivelä, Janne Koivumäki, Jarmo Nurmi, and Erkki Lehto from TUT/IHA. Special thanks to my friends and colleagues of the "Kavitaatio" room for the good working atmosphere and many fruitful scientific discussions over the years.

This thesis was partly funded by the Tampere Graduate School of Concurrent Engineering (GSCE). I gratefully acknowledge the GSCE led by Prof. Erno Keskinen for the financial support. Partial funding was also received from the K.F. and Maria Dunderberg foundation, and from the Academy of Finland under the grant number 133273: "Sensor network based intelligent condition monitoring of mobile machinery". This funding is most greatly appreciated.

Finally, I wish to thank my family and friends for their continued support throughout the years and especially Elina, my love, for the understanding and motivation particularly during the final stages of my doctoral studies.

Contents

Acronyms

CAN	controller area network
DH	Denavit-Hartenberg
DOF	degree of freedom
GMA	geometric moving average
IMU	inertial measurement unit
LQR	linear quadratic regulator
MCU	microcontroller unit
MEMS	micro-electro-mechanical system
PAE	peak absolute error
PI	proportional-integral
PID	proportional-integral-derivative
RMSE	root-mean-square error

Nomenclature

For some symbols, sub- and superscripts i, j and k vary locally depending on the context.

Latin alphabet

a^x	accelerometer x axis output
a^y	accelerometer y axis output
a^z	accelerometer z axis output
${}^i a^x_{P_i^j}$	x axis component of ${}^i\mathbf{a}_{P_i^j}$
${}^i a^y_{P_i^j}$	y axis component of ${}^i\mathbf{a}_{P_i^j}$
${}^i a^z_{P_i^j}$	z axis component of ${}^i\mathbf{a}_{P_i^j}$
${}^i\mathbf{a}_{P_i^j}$	linear acceleration of $\{P_i^j\}$ with respect to $\{I\}$ expressed in $\{B_i\}$
${}^B_I\mathbf{a}_B$	linear acceleration of $\{B\}$ with respect to $\{I\}$ expressed in $\{B\}$
A	motion amplitude
$A(k)$	optimal derivative coefficient
b	inclination estimate bias
$\hat{b}$	bias estimate
$\hat{b}^x$	gyroscope bias estimate
$\mathbf{b}_\alpha^i$	angular acceleration estimate bias
$\hat{\mathbf{b}}_\alpha^i$	estimate of $\mathbf{b}_\alpha^i$
$\mathbf{b}_a$	accelerometer bias
$\mathbf{b}_g$	gyroscope bias
$\hat{\mathbf{b}}_{g_i}$	estimate of $\mathbf{b}_g$ for ith gyroscope
${}^B\mathbf{b}_m$	magnetic disturbance in $\{B\}$
$\mathbf{b}_v^i$	linear acceleration estimate bias

$\{B\}$	body coordinate frame
$B(k)$	optimal derivative coefficient
$C(k)$	optimal derivative coefficient
$C(s)$	feedback controller
d_i	DH-parameter for joint i distance
${}^{G}\mathbf{d}_B$	position of moving origin relative to fixed global origin
${}^{G}\dot{\mathbf{d}}_B$	velocity of moving origin relative to fixed global origin
${}^{G}\ddot{\mathbf{d}}_B$	acceleration of moving origin relative to fixed global origin
e_c	tracking error
$\mathbf{e}_3$	coordinate system unit vector
f	frequency of motion
$F(s)$	low-pass filter transfer function
$\mathbf{g}$	gravitational field
g_k	geometric moving average filter output
$\{G\}$	global coordinate frame
I	identity matrix
$\{I\}$	inertial reference frame
$I_{\mathbf{x}}$	mass moment of inertia
$J(\mathbf{q})$	Jacobian matrix
$J^{-1}(\mathbf{q})$	inverse Jacobian matrix
${}^{0}\hat{k}_{i-1}$	unit vector of joint i axis
K	feedback gain vector
K_a	acceleration feedback gain
K_{qa}	velocity gain
k_{I}	integral gain
k_{P}	proportional gain
K_v	velocity feedback gain
l_i	length of link i
L_{cm}	suspended load centre of mass distance
m_P	total mass of suspended load assembly
${}^{I}\mathbf{m}$	Earth's magnetic field in $\{I\}$
${}^{B}_{I}\mathbf{m}_B$	magnetic field of $\{B\}$ with respect to $\{I\}$ expressed in $\{B\}$
$\bar{N}$	weighting scalar

o	moving origin
O	global origin
P	rigid body point
Q	weighting matrix
r	controller reference input
r_i^x	polynomial path coefficient
r_i^y	polynomial path coefficient
${}_j^i\mathbf{r}_k$	position of $\{B_k\}$ with respect to $\{B_j\}$ expressed in $\{B_i\}$
${}_j^i\dot{\mathbf{r}}_k$	velocity of $\{B_k\}$ with respect to $\{B_j\}$ expressed in $\{B_i\}$
${}_j^i\ddot{\mathbf{r}}_k$	acceleration of $\{B_k\}$ with respect to $\{B_j\}$ expressed in $\{B_i\}$
${}^GR_B$	relative rotation of $\{B\}$ with respect to $\{G\}$
R_i	relative rotation of $\{B_i\}$ with respect to $\{I\}$
$\hat{R}_i$	estimate of R_i
S_a	accelerometer scale factor error
S_g	gyroscope scale factor error
T_s	sample time
$u(k)$	moving average filter input
$\mathbf{u}_v$	valve control output
$U(s)$	control input
${}^G\mathbf{r}_P$	global position of body point P
${}^i\mathbf{r}_{P_i^0}$	position vector of $\{P_i^0\}$ with respect to $\{I\}$ expressed in $\{B_i\}$
${}^G\dot{\mathbf{r}}_P$	global velocity of body point P
${}^G\ddot{\mathbf{r}}_P$	global acceleration of body point P
${}^i\dot{\mathbf{v}}_{P_i^0}$	linear acceleration of $\{P_i^0\}$ with respect to $\{I\}$ expressed in $\{B_i\}$
${}^i\hat{\dot{v}}_{P_i^0}^y$	y axis component of ${}^i\hat{\dot{\mathbf{v}}}_{P_i^0}$
${}^i\hat{\dot{v}}_{P_i^0}^z$	z axis component of ${}^i\hat{\dot{\mathbf{v}}}_{P_i^0}$
${}^i\hat{\dot{\mathbf{v}}}_{P_i^0}$	estimate of ${}^i\dot{\mathbf{v}}_{P_i^0}$
$\mathbf{q}$	manipulator joint position vector
$\dot{\mathbf{q}}$	manipulator joint velocity vector
$\dot{\mathbf{q}}^{ref}$	joint velocity reference
u	system input
$\dot{\mathbf{v}}$	true instantaneous linear acceleration
$\mathbf{v}_m$	magnetic direction vector

$V(s)$	velocity input
$\ddot{x}$	end-effector horizontal acceleration
x_1	first complementary filter input
x_2	second complementary filter input
x_{cm}	centre of mass horizontal position
$\dot{x}_{cm}$	centre of mass velocity
x_{cm}^{ref}	load centre of mass reference position
x_d	desired end-effector x coordinate
$\mathbf{x}$	manipulator end-effector position vector
$\dot{\mathbf{x}}$	manipulator end-effector velocity vector
$\dot{\mathbf{x}}^{ref}$	end-effector velocity reference
$\mathbf{x_c}$	cylinder position vector
$\mathbf{x_c}^{ref}$	cylinder position reference
$\dot{\mathbf{x}}_\mathbf{c}$	cylinder velocity vector
$\mathbf{x}_{SL}$	suspended load motion state vector
$X(s)$	position input
y_d	desired end-effector y coordinate
$\hat{y}$	complementary filter output
$Y(s)$	position output

Greek alphabet

${}_G\boldsymbol{\alpha}_B$	angular acceleration of $\{B\}$ with respect to $\{G\}$
${}^i\boldsymbol{\alpha}_i$	angular velocity of $\{B_i\}$ with respect to $\{I\}$ expressed in $\{B_i\}$
${}^i_j\boldsymbol{\alpha}_k$	angular acceleration $\{B_k\}$ with respect $\{B_j\}$ expressed in $\{B_i\}$
${}^i_j\hat{\boldsymbol{\alpha}}_k$	estimate of ${}^i_j\boldsymbol{\alpha}_k$
${}^i_j\hat{\boldsymbol{\alpha}}^{\mathrm{I}}_k$	integral-type filtered estimate of ${}^i_j\boldsymbol{\alpha}_k$
γ	moving average filter forgetting factor
δ_n	natural damping ratio
δ_n'	modified natural damping ratio
$\Delta\theta_i$	inclination estimate error
$\Delta\phi_i$	joint angle estimate error
θ	inclination angle

$\hat{\theta}$	inclination angle estimate
μ	inclination estimate noise
$\boldsymbol{\mu}_{\alpha}^{i}$	angular acceleration estimate noise
$\boldsymbol{\mu}_{a}$	additive accelerometer measurement noise
$\boldsymbol{\mu}_{m}$	additive magnetometer measurement noise
$\boldsymbol{\mu}_{g}$	additive gyroscope measurement noise
$\boldsymbol{\mu}_{v}^{i}$	linear acceleration estimate noise
ρ_i	measurement weight
τ	time constant
$\hat{\phi}_i$	joint angle estimate
$\hat{\dot{\phi}}$	joint angular velocity estimate
ω_n	natural frequency
$\omega_n^{'}$	modified natural frequency
${}^{i}\omega_{i}^{x}$	x axis component of ${}^{i}\boldsymbol{\omega}_i$
${}^{i}\omega_{i}^{y}$	y axis component of ${}^{i}\boldsymbol{\omega}_i$
${}^{i}\omega_{i}^{z}$	z axis component of ${}^{i}\boldsymbol{\omega}_i$
${}^{i}\boldsymbol{\omega}_i$	angular velocity of $\{B_i\}$ with respect to $\{I\}$ expressed in $\{B_i\}$
${}_{G}\boldsymbol{\omega}_{B}$	angular velocity of $\{B\}$ relative to $\{G\}$
${}_{j}^{i}\boldsymbol{\omega}_k$	angular velocity of $\{B_k\}$ relative to $\{B_j\}$ expressed in $\{B_i\}$
${}_{j}^{i}\hat{\boldsymbol{\omega}}_k$	estimated angular velocity of $\{B_k\}$ relative to $\{B_j\}$ expressed in $\{B_i\}$
${}_{j}^{i}\dot{\boldsymbol{\omega}}_k$	angular acceleration of $\{B_k\}$ relative to $\{B_j\}$ expressed in $\{B_i\}$
Ω^x	gyroscope x axis output
${}_{I}^{B}\boldsymbol{\Omega}_{B}$	gyroscope-measured angular velocity of $\{B\}$ with respect to $\{I\}$ expressed in $\{B\}$

Chapter 1

Introduction

The recent widespread availability of micro-electro-mechanical system (MEMS) components has led to the development of a wide product range of low-cost, light-weight, low-power miniaturized inertial measurement units. MEMS components combine surface micromachined polysilicon structures and signal conditioning circuitry on the same substrate. The size of the mechanisms is measured in the micrometre range, which leads to a very small component package size. These characteristics have made MEMS inertial sensors successful in a variety of industries, such as automotive, consumer electronics and military/aerospace, and for a number of uses, including aerial vehicle attitude estimation, road vehicle stability systems, motion-enabled user interfaces for mobile phones and portable devices, gaming and virtual reality systems, robotic toys, and inclinometers. When considering the field of heavy-duty hydraulic manipulators used in mobile work machines, which is one of the most significant industry branches in Finland, there is substantial potential for the application of MEMS inertial sensors, which is still largely unknown. High quality, rapid responses to quickly changing market needs, innovative products, and low costs are vital to successful operations on the increasingly competitive global mobile machine market. This race leads to a higher density of functionality in products, and it becomes necessary to integrate different technologies, such as mechanical, electrical and fluid subsystems, with embedded software. The increased amount of functionality in the form of machine life-cycle management and service, advanced robotic controls, fault diagnosis, and condition-based maintenance, has become a major competition advantage for mobile work machine manufacturers (see e.g. Jardine et al. [1] and Peng et al. [2]). Thus, the challenge for machine manufacturers is to be distinguished by these value-adding services and products in the highly competitive industrial branch.

The thesis has the following motives. Traditionally, the problem of controlling mobile

working machines has essentially been solved on the individual machine level. Skilled operators have a key role in this scenario since typical non-instrumented machines are operated by controlling each hydraulic actuator separately via operator visual feedback. To obtain the optimal operation speed and loading configuration for the machine, the operator requires an extensive period of practise to become familiar with the non-intuitive, open-loop control system. This makes the machine operation prone to human errors which, according to Lovgren [3], cause 73% of all crane-related accidents. In addition, intelligent machines are expected to provide business-level services in the near future by collaborating autonomously in teams with humans as a critical part of a multi-company business process (see e.g. Saarinen et al. [4], Halbach and Halme [5], Bergkvist et al. [6], and Hallonborg [7]). Current research efforts are targeted towards autonomously operating mobile machines that rely on a multitude of sensors to perceive the working environment and allow robotic control of the machine functions (see e.g. Billingsley et al. [8], Ringdahl [9], Hellström et al. [10], Berns et al. [11]), as well as towards the realisation of safety- and efficiency-boosting systems (see e.g. Zhang and Hammad [12]). This implies that better instrumented machines with novel sophisticated functionality are needed. Since the machines are highly critical to businesses, they should also be monitored and maintained online under the control of enterprise resource management. Unfortunately, current control systems fail to satisfy these requirements.

Advanced robotic control and condition monitoring systems fundamentally depend on multi-sensor instrumentation to be available on the mobile machines. The aim of the instrumentation is to reveal the state of the machinery. For this information to be suitable for a closed-loop motion controller, highly accurate real-time measurements of positions, angles, rates and accelerations are needed. Most importantly, only minor delays are acceptable. Thus, the performance of the multi-sensor instrumentation is critical for the performance of the control system. From an applicability point of view, this multi-sensor instrumentation must be low-cost and easy to install. Further demands on the components are posed by the harsh environmental working conditions of mobile machines. The sensors must be prepared to withstand heat, very low temperatures, heavy impacts and vibrations as well as water and ice. Due to the mobile nature of the work, an emergency service team will not be quickly available in case of a sensor malfunction or break-down. Consequently, a long-standing problem has been the poor availability of easy-to-install robust motion sensors for robotic control and condition monitoring systems.

A traditionally used solution for measuring hydraulic manipulator motion states is to use a rotary-type optical incremental encoder or a resolver (Figure 1.1), which directly measures the angular position of the manipulator joint pins. Velocity and acceleration, which are the first- and second-order derivatives of motion and are

required for high-performance robotic control of the manipulator, are typically derived by differentiating the encoder position signal. Since differentiation is a noise amplifying process, the resulting velocity and acceleration signals have very limited bandwidth and suffer from quantization noise during slow motions.

For an incremental encoder to be suitable for the harsh environmental working conditions of mobile machines, it must be enclosed in a metal case with special surface protection and large, resilient bearings that can endure high axial and radial loads. Additional special axial seals are needed for hollow-shaft type encoders, and enhanced electrical insulation is required to prevent damage from possible shaft currents to the ball bearings and running surfaces. The installation of incremental encoders on hydraulic manipulators requires a high degree of co-axiality between the encoder shaft and the manipulator joint pin. The permissible radial shaft movement during rotation is typically in the sub-millimetre range. Consequently, the hydraulic manipulator joint structures must be designed to consider the sensor's high-precision mounting and shielding requirements. Considering the intended use of a mobile machine, it is more desirable to be able to design the joint mechanisms purely based on the required forces and torques set by the application domain. Retrofitting encoders on existing machines requires designing custom, high-precision mechanisms, which leads to increased system costs. Moreover, the installation of joint encoders on existing hydraulic manipulator structures may be considered extremely difficult for purely practical reasons, as noted by Keskinen et al. [13], or completely infeasible for certain types of widely-used hydraulic manipulators due to structural support bars moving over the joint centres during operation (see Cheng et al. [14]).

Figure 1.1: Heidenhain ECN/EQN/ERN 400 series incremental encoder [15].

Alternatively, the rotary and prismatic joint positions of a hydraulic manipulator can be derived from measured cylinder piston positions. The position reading may be obtained using a linear potentiometer, a linear variable differential transformer or

a magnetostrictive transducer (see e.g. [16]) installed inside the hydraulic cylinder, for example. While this type of transducer is feasible e.g. for measuring the position of a telescopic extension of a forestry crane, which is typically controlled by a single cylinder, a loader crane might have a telescopic extension link consisting of ten separate sections that are each controlled by a dedicated cylinder. Furthermore, the use of this type of sensor requires the complete re-design of the cylinder during the manufacturing phase and again forces the design to account for a precision instrument inside a mechanism originally designed to transmit large forces. In the case of a sensor malfunction, the mobile machine experiences substantial production down-time since the manipulator structure must be disassembled to replace the cylinder containing the faulty sensor.

As a key advantage over traditionally used sensor solutions, no mechanical coupling to rotating joint pins is required with MEMS sensors. An inertial measurement unit (IMU) can be constructed by combining MEMS accelerometers with angular rate gyroscopes and optional magnetometers to obtain physical orientation, velocity and acceleration measurements – all with a single compact sensor module. Despite the wide availability of MEMS components, observation models and measurement data processing methods suitable for mobile machine manipulator motion state estimation and subsequent closed-loop control are not generally known or well understood. Frequently encountered problems in manipulator motion state estimation with IMUs relate to large transient errors experienced during accelerative motions as well as substantial drift observed in the position readings. This can be attributed to insufficient treatment of the fundamental kinematic principles to ensure correct complementary nature of inertial readings prior to sensor fusion. This makes several of the proposed solutions infeasible for transfer onto full-scale systems for long-term use (see e.g. Giansanti et al. [17], Luinge and Veltink [18], Luinge et al. [19], Quigley et al. [20] and El-Gohary and McNames [21]). Consequently, current commercial examples of MEMS inertial sensors applied to heavy-duty mobile machines are limited to quasi-static situations and open-loop user assisting functions (see e.g. Novatron Oy [22], Scanlaser Oy [23]).

1.1 Control problem of hydraulic manipulators

The heavy-duty manipulators used on mobile machines are almost exclusively powered by hydraulic actuators due to their high power-to-weight ratio, high acceleration and force/torque capability, low cost and flexible mounting options within the manipulator structure. Since the power to the actuators is transmitted via high-pressure fluid from a central power unit outside the manipulator, there is no need to mount bulky power

generating components or gear assemblies on the manipulator structure itself, as would be the case with electrical motors and linear actuators. Thus, the manipulator structure can be kept relatively light while still being able to handle loads greater than the manipulator mass itself.

When the hydraulic actuators are brought under the control of an automated closed-loop motion control system, a hydraulic servo system is formed, which is widely used for high-performance position, velocity and force control of the manipulator. However, hydraulic servo systems typically have highly non-linear characteristics due to, for example, the variable effective bulk modulus and pressure-flow dependency in turbulent orifice flow. Additionally, the high friction force of the cylinder in particular has a significant effect on the system damping, making accurate control of the manipulator difficult.

Although it is a simplification, the inherently non-linear hydro-mechanical system is typically represented by a linear model for motion control purposes by examining its Taylor series expansion at a certain operating point. Assuming a linear time-invariant system and treating all gravitational, inertial, centripetal and frictional terms as external disturbances, a hydraulic valve and actuator combination can be modelled with a linear second-order open-loop transfer function between the valve control input and actuator velocity as

$$H(s) = \frac{V(s)}{U(s)} = \frac{K_{qa} \cdot \omega_n^2}{s^2 + 2\delta_n \omega_n s + \omega_n^2}, \tag{1.1}$$

where $V(s)$ and $U(s)$ are the output velocity and control input, K_{qa} is the velocity gain, δ_n is the natural damping ratio and ω_n is the natural frequency of the system (see e.g. Watton [24]).

A traditional control approach is the linear output feedback controller, which has a well-established theoretical background in many control engineering books (see e.g. Dorf and Bishop [25]). The basic structure is illustrated in Figure 1.2, where $C(s)$ denotes a feedback controller, $X(s)$ is the reference position input and $Y(s)$ is the position output. Obtaining an outer unity feedback loop is typically a mere scaling problem in servo systems. Proportional-integral-derivative (PID) controllers are effective and still widely used in many applications. The simple proportional controller is robust against modelling errors and easy tune, which makes it a common starting point for controller design (see e.g. Jelali and Kroll [26]) for details.

As modern industry operations demand ever-increasing performance from motion control systems, the PID controller may become insufficient because the dynamics of a hydraulic positioning servo system are of the third order (see e.g. Åström and

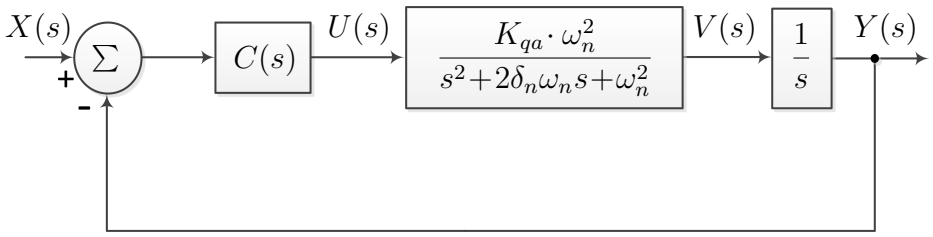

Figure 1.2: Output feedback controller for a hydraulic positioning servo system.

Hägglund [27]). The inherent low damping of hydraulic systems limits the gain margin of the output feedback controller, which in turn limits the obtainable closed-loop motion control tracking performance. Increasing the controller gains naturally leads to improved tracking performance; however, an increase in system damping is required to maintain stability. This problem can be addressed on the system level by i) over-sizing the hydraulic actuators; ii) introducing additional leakages; or iii) using additional actuators as passive damping elements. The general trend is to avoid installing new separate actuators because it increases costs and becomes particularly extensive for mobile machines due to the required additional installation and control effort. It is therefore preferable to use the existing actuators in an active role to achieve an increase in damping (see Rahmfeld and Ivantysynova [28]).

In the domain of linear control theory, closed-loop pole placement is a well-established approach for improving the performance of a hydraulic servo positioning system. Pole placement is used, because the locations of the transfer function poles on the s-plane correspond directly to the eigenvalues of the system, which in turn define the system response characteristics. Also termed state feedback control, this control approach requires feedback from the system state variables, which for the hydraulic servo system in Figure 1.2 imply feedback from velocity, acceleration and actuator position. Assuming ideal feedbacks on position, velocity and acceleration, the controller structure allows the placement of the closed-loop transfer function poles by adjusting the state feedback (controller) gains, which leads to more manipulability of the system dynamics. A closed-loop position control system with state feedback control is shown in Figure 1.3.

The control system consists of an inner second-order velocity control loop with feedback gains K_v and K_a, an outer unity feedback and a gain K_p for the position error. After incorporating the feedback gains K_v and K_a into the transfer function (1.1), the inner velocity control loop becomes:

$$H_{vel}(s) = \frac{V(s)}{U(s)} = \frac{K_{qa} \cdot \omega_n^2}{s^2 + (2\delta_n\omega_n + K_a K_{qa}\omega_n^2)s + (1 + K_v K_{qa})\omega_n^2}. \tag{1.2}$$

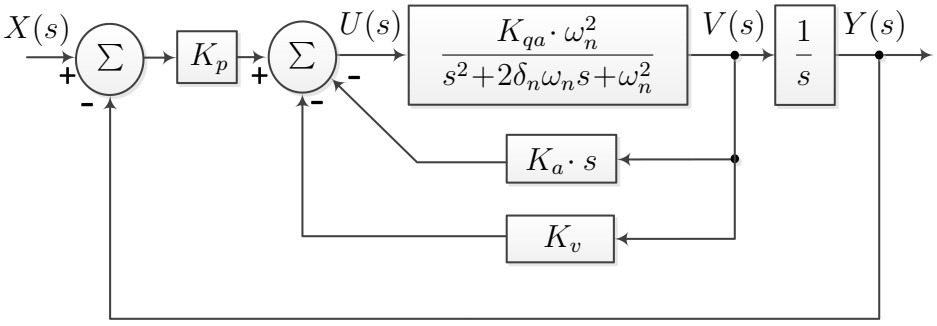

Figure 1.3: State feedback controller

Comparing transfer functions (1.1) and (1.2), it can be seen that the servo system with state feedback has a new damping ratio:

$$\delta_n^{'} = \frac{2\delta_n + K_a K_{qa} \omega_n}{2\sqrt{1 + K_v K_{qa}}} \tag{1.3}$$

and a new natural frequency:

$$\omega_n^{'} = \omega_n \sqrt{1 + K_v K_{qa}}. \tag{1.4}$$

From (1.3) and (1.4), it can be seen that the system damping increases with the acceleration feedback gain K_a. The natural frequency of the state feedback control system increases with the feedback gain K_v; however, the damping ratio simultaneously becomes smaller.

Generally, obtaining full motion state information (position, velocity and acceleration) on a multi-axis system has proven to be problematic, especially regarding the measurement of relative acceleration between the hydraulic manipulator links. The traditional approach using incremental encoders is to compute the first- and second-order time derivatives indirectly by single/double differentiation of the encoder position signal and to use predictive post-filtering on the differentiated signals. Calculated at high sampling rates, this approach amplifies high-frequency perturbations and quantization effects on the resulting signals to a large extent. For this reason, direct acceleration feedback is frequently avoided altogether (see e.g. Han et al. [29], Muhammad et al. [30], Jabbour et al. [31], Sirouspour and Salcudean [32]) and alternative state-observer-based methods are used instead, which rely on modelling of the entire hydro-mechanical system dynamics. The velocity and acceleration are estimated from system input and position output measurements, which are typically readily available. However, the required modelling and controller design effort for

these approaches can be considered extensive. When a state observer is used as part of a hydraulic manipulator closed-loop control system, the stability of the controller must be proven for both the nominal and uncertain plant models since the highly non-linear hydraulic manipulator typically works under large load uncertainties (see e.g. Zhai [33], Pi and Wang [34]). Alternative time derivative estimation techniques, such as proposed by Merry et al. [35], use time-based encoder pulse counting and require high-resolution time stamps of encoder pulse count events, which typically leads to the use of external timer/counter hardware and increases the system cost further.

Ovaska and Väliviita [36] summarize typical indirect differentiation and filtering methods for producing low-noise motion derivatives from joint angular velocity or position measurements. The reviewed methods are often very successful provided that the sampling rate is low. However, today's sampling rates (and especially quantization) noise may reach levels at which these types of filtering techniques become ineffective in producing usable feedback for closed-loop motion control applications. Since the quantization step in an angular acceleration signal, which is directly double-differentiated from position, increases quadratically as the sample time shortens, the control system may become unstable quickly when the position change between sample points is very small. An alternative approach published by Harrison and Stoten [37] provides an estimation method for derivatives of arbitrary order from velocity or position measurements for a given combination of signal-to-noise ratio and sampling-to-signal frequency ratio. The provided optimal coefficients of the discrete derivative minimise the error between the derivative and its Taylor series expansion representation. For modern control systems, even this type of velocity and acceleration estimation may limit the controller's performance.

In addition to the previously described high-performance motion control of the hydraulic manipulator, motion state feedback is also used with suspended load anti-sway control systems. A payload suspended from a manipulator exhibits pendulum-like characteristics with prominent uncontrolled oscillation during acceleration and deceleration of the manipulator end-effector. This type of system is underactuated by nature since the position and velocity of the manipulator end-effector can be controlled while the load swing angle and angular velocity can only be controlled indirectly. While a highly skilled operator may be able to control the load swaying, the need for an automated control system lessening the burden of the human operator is justified. Presently, such assisting control systems are already widely available for overhead gantry cranes. However, only a few applicable control concepts have been proposed for more complex articulated multi-link cranes (see e.g. Bak et al. [38], Kjelland et al. [39, 40]). In the works of Kim et al. [41] and Neupert et al. [42], which describe full-scale realisations of such operator assisting systems, the

measurement of the load swing angle and angular velocity has been reported as a main challenge. For this reason, several alternative approaches in load sway suppression systems use an open-loop technique of input command shaping, in which the manipulator operator control commands are filtered to remove components that induce load oscillations. However, if disturbance rejection and accurate positioning of the load is desired, augmentation of the system with a feedback loop comes into question (see e.g. Sorensen et al. [43], Garrido et al. [44], Ahmad et al. [45], Vaughan et al. [46]).

Considering the challenges in realising the discussed motion state feedback systems, the small size, surface mounting capability and type of inertial measurements provided by MEMS sensors make them ideally suitable for the task. This implies both straightforward retrofitting onto existing hydraulic manipulator structures and full motion state sensing capability of the complete kinematic chain, which may include e.g. a suspended load to be transported. In particular, the advantages of MEMS inertial sensors in estimating the joint angular velocities and angular accelerations are two-fold: i) a MEMS angular rate gyroscope measures the link angular rate directly; and ii) the link angular acceleration can be derived from accelerometer readings without noise-amplifying differentiation or lag-inducing post-filtering by applying well-known rigid body motion kinematics.

1.2 MEMS-based motion sensing

A MEMS accelerometer measures dynamic and constant accelerations with the force of gravity representing a special case of constant acceleration. If the accelerometer is fully stationary, i.e. no lateral or vertical accelerations are present, the inclination angle can be calculated from the measured gravity component. A horizontally mounted accelerometer with two orthogonal xy axes allows two-degree-of-freedom (DOF) inclination sensing up to approximately 45 degrees of tilt with respect to the local gravity direction. Since the axis outputs of the accelerometer follow the sine and cosine functions as a function of the tilt angle, the output sensitivity in response to a change in tilt rapidly decreases if the angle becomes higher than 45 degrees, thus prohibiting accurate inclination sensing up to 90 degrees of tilt with this configuration. Furthermore, the absence of a z axis prevents the detection of an inverted sensor posture. If the dual-axis accelerometer is mounted vertically, the 1-DOF inclination angle can now be measured throughout a 360 degree range, since the 90-degree difference in the sensing axes orientation keeps the output sensitivity constant. Adopting a three-axis xyz accelerometer, the 2-DOF rotation matrix of the sensor can be estimated throughout a 360-degree range. The 2-DOF

estimates of the hydraulic manipulator joint angles can now be constructed by mounting accelerometers on the manipulator links and subtracting the successive link inclination estimates from each other. However, because the output of a linear MEMS accelerometer also contains the instantaneous linear accelerations of motion, this type of straightforward and "traditional" inclination estimation (see e.g. Łuczak et al. [47]) gives erroneous readings during accelerative motions. If the accelerometer outputs are low-pass filtered, ultra low-noise inclination sensing is possible with the disadvantage of significant phase delay and bandwidth limitations to typically less than 1 Hz. While this approach may be used for low-bandwidth manipulator link inclination estimation, it is infeasible for supplying the high-bandwidth low-delay feedback required for the real-time closed-loop motion control of a hydraulic manipulator. Moreover, this approach leaves unsolved the problem of link velocity and angular acceleration estimation, which are of critical importance for high-performance motion control of hydraulic manipulators.

The MEMS gyroscope measures the angular velocity around one to three orthogonal axes. The angular velocity is sensed by observing a change induced by the Coriolis effect on a vibrating proof mass. Integrating the angular rate output of a MEMS gyroscope gives a reliable short-term estimate of the inclination angle, which is also robust against acceleration effects. Unfortunately, the output of a gyroscope is perturbed by a low-frequency bias term, which makes long-term integration of the rate signal unsuitable for keeping track of the inclination angle. As an improvement to purely accelerometer-based sensing, "gyro-aided" methods combine accelerometer readings with gyroscope angular rate data. A widely used solution for the fusion of MEMS accelerometer and gyroscope data is the classic forward-predicting Kalman filter, which can be used to combine several redundant noisy measurements to produce a statistically optimal estimate the underlying system state. The use of the Kalman filter requires a process model and quantifying the statistical noise characteristics of the process model and the individual measurement sources. Complementary filtering is a general term describing estimation techniques that combine several measurements while simultaneously minimising individual error sources without knowledge of the exact frequency content of individual error sources. However, for a class of filtering problems, the assumption that the measurements are corrupted by stationary white noise produces a stationary Kalman filter that is identical in form to a complementary filter, which does not require a time-domain statistical description for the noise corrupting its input signals. The noise variation dependent steady-state Kalman gains can therefore be viewed as a means of shaping the frequency response of the (complementary) filter as desired.

To enforce "traditional" gravity-based inclination sensing during accelerative motion, linear accelerations acting on the accelerometer's sensing axes must be determined

and compensated for. Thus, "geometry-aided" inclination sensing refers to a type of robust motion sensing in which a complete forward kinematics model of the studied system is constructed. Simplified motion kinematics models allow the compensation of the acceleration effects on the inclination readings to some degree, but in order to arrive at a widely applicable approach, the kinematic relationships must be further investigated and understood. This is especially relevant for high-velocity manipulators consisting of multiple joints and links. Accelerometers mounted on the links of such a manipulator will undergo high-acceleration manoeuvres and be subject to acceleration components, which fall outside the category of random noise corrupting the accelerometer signals.

1.3 Earlier research on MEMS-based manipulator motion sensing and control

Since the accelerometer-based inclination estimate is susceptible to large errors from acceleration effects during motion and the integrated gyroscope angle estimate drifts over time, a properly constructed inclination estimate should account for both of these facts simultaneously. As an initial improvement to the overall static accuracy of the accelerometer-based inclination estimate and the amount of gyro drift, the calibration of MEMS accelerometer and gyroscope bias values as well as the output scale factors has been considered in works of Frosio et al. [48], Bekkeng [49], Aggarwala et al. [50] and Amirsadri et al. [51], among others. Although an improvement to the static inclination estimate accuracy may be obtained, the gyroscope bias drift cannot be completely eliminated by one-time calibration since the bias is slowly time-varying and temperature-dependant. Naturally, the problem of motion-induced perturbations on the accelerometer inclination estimate still remains.

A key disadvantage of purely accelerometer-based rotation estimates are the singularity conditions that arise if the joint axis of rotation becomes parallel to gravity. For this reason it is more desirable to use the integrated gyroscope angular velocity for the rotation estimate, since it does not suffer from singularities, and use other redundant measurement sources for bounding the drift caused by the gyro bias. This sensor fusion between MEMS accelerometers, gyroscopes and other optional measurement sources is frequently performed with the classic Kalman filter or with the non-linear extended Kalman filter (see e.g. Brigante et al. [52], Lee et al. [53], Zhu and Zhou [54], Zhu et al. [55], Leavitt et al. [56] and Petruska and Meek [57]). The extended Kalman filter can be used to approximate a non-linear process model, which is typically the case with motion kinematics, by linearising the process model with the Taylor series expansion. This, however, brings about the added difficulty of

guaranteeing the global convergence of the filter; additionally, the filter performance may be poor if the dynamics are highly non-linear (see e.g. Brown and Hwang [58]). Furthermore, the underlying assumptions of both the classic and the extended Kalman filters regarding sensor output linearity and Gaussian statistics may work well for high-grade, high-cost sensors, but they do not fit as well to low-cost, low-quality MEMS sensors. In this case, the complementary filter is a computationally effective alternative that makes no assumptions about the statistics or linearity of the signals. It has been applied for the fusion of low-cost MEMS sensor data by Weinberg et al. [59], Kubus et al. [60] and Mahony et al. [61], among others. Recently, Euston et al. [62] applied complementary filtering for the attitude estimation of a fixed-wing unmanned aerial vehicle.

Fourati et al. [63] considered estimating 3-DOF rotations by including a MEMS magnetometer and adopting the quaternion representation since it is known to be computationally efficient and it avoids the singularities of the Euler angle representation. While a magnetometer can be used to provide a reliable long-term reference of the z axis rotation (heading angle), Caruso [64] found it very sensitive to magnetic disturbances from external sources that cause significant errors to the heading estimate. Although the disturbances can be compensated for to some degree in controlled and limited conditions, as proposed by Roetenberg et al. [65], a magnetometer can be considered an unrealistic option for surface mounting onto the large metallic structures of hydraulic manipulators since they operate in uncontrolled environments and the constantly changing manipulator geometry of the articulated machine causes time-varying soft-iron effects to the surrounding magnetic field.

Since the magnetometer is an infeasible option for heavy-duty hydraulic manipulators, the accelerometer-based long-term reference should be adopted. Roan et al. [66] propose this type of gyro-aided rotation estimation approach for multi-link manipulators. However, since a kinematic model was not used, the manipulator motions must be assumed to be slow to prevent significant error accumulation to the accelerometer-based gyro bias estimate. Consequently, a properly constructed accelerometer-based long-term reference for bounding the gyro drift should be motion compensated to be disturbance free. In view of Newtonian mechanics, most of the relevant kinematic quantities are non-linear functions of angular velocity and angular acceleration, which are not easy to define without rate gyroscopes (see Cardou et al. [67]). If simplified motion kinematics models are constructed, such as proposed by Dejnabadi et al. [68] and Wang et al. [69], the motion perturbations on the accelerometer-based reference can be compensated for to some degree. Cheng and Oelmann [70] compare several gyro-aided methods for joint angle sensing in which the motion effects are compensated for using simplified kinematic models with common-mode and differential rejections of disturbing accelerations. However, to

arrive at a widely applicable estimation approach, the velocities and accelerations must be propagated from link to link with a complete multi-body manipulator forward kinematics model. This type of complete kinematics model was adopted in the work of El-Gohary and McNames [21]; however, the chosen inertial sensor fusion method limited the results to an unacceptable level for hydraulic manipulator closed-loop motion control.

Despite the large amount of research conducted on the various aspects of MEMS-based motion sensing, there are still relatively few published works solely concerning MEMS-based closed-loop control of multi-link manipulators. To the author's knowledge, the existing works have yet to combine all the previously discussed key points in a single feasible motion state feedback solution. For example, Quigley et al. [20] note that a solely accelerometer-based closed-loop motion control system of a multi-link robotic manipulator quickly becomes unstable in dynamic situations without the use of stabilizing encoder position measurements. Ghassemi et al. [71] assume transient accelerations as mere superimposed noise on the accelerometer-based estimates, which necessitates delay-inducing low-pass filtering of the joint angle readings and leads to oscillatory behaviour of the control system. Aref et al. [72] apply MEMS sensors and quaternion-based complementary filtering to estimate and control the boom and fork angles of a forklift truck. The assumption that a complementary (or Kalman) filter alone is sufficient to remove the perturbations from the inclination estimate may work well provided that i) the manipulator is small in size and the angular velocities and linear link accelerations are low; and ii) transient accelerations are mainly vibrations on a higher frequency spectrum than the actual motion of the manipulator. However, in the example of a forest harvester hydraulic manipulator, where the harvester head moves several meters per second, the linear accelerations exerted on surface-mounted accelerometers are significant; additionally, the perturbing accelerations occupy the same frequency band as the motion of the manipulator. Since the complementary filter applies a low-pass filter on the accelerometer readings, the two acceleration sources become inseparable. A forward kinematics model of the manipulator is therefore required to decouple the kinematic quantities before applying any filtering.

1.4 Objectives of the thesis

The main objective of this thesis is to produce a novel method for applying low-cost MEMS inertial sensors to the motion state sensing and closed-loop control of heavy-duty hydraulic manipulators. Since the model is to be applied to a variety of manipulator geometries consisting of an arbitrary amount of rigid links connected by rotary joints, it must be general in nature. To achieve this, the output characteristics

of the individual sensors need to be characterised and the measurements from multiple sensors must be seamlessly combined using signal processing methods to create low-noise, drift-free, low-delay estimates of link positions, velocities and accelerations.

To facilitate the required multi-sensor fusion, a complete forward kinematics model of the manipulator system is required in order to compensate for the linear, centripetal and centrifugal acceleration effects from the accelerometer readings. This kinematic modelling is a prerequisite for obtaining complementary inertial measurements of the manipulator motion. By then fusing the motion compensated accelerometer readings with the gyroscope angular rate data, smoothed high-bandwidth, low-delay and low-noise estimates of the manipulator motion states may be constructed. Sensor reading fusion using complementary filtering allows the use of the complementary good portions of the spectrum of both components while minimising error sources. Thus, the novel contributions of this thesis relate to the class of "geometry-aided" motion state estimation methods where the underlying forward kinematics model lays a theoretically sound foundation for the fusion of redundant inertial measurements. Table 1.1 provides a comparison of the discussed motion sensing approaches. Note that the comparison is made here only with respect to the link inclination sensing properties. If considering the full manipulator motion state estimation problem, which also includes the link velocity and acceleration state estimates, only the "geometry-aided" approach can be considered a feasible solution.

Table 1.1: Inclination sensing methods in accelerative angular motion

Estimation method	traditional	traditional + low-pass filter	gyro-aided	geometry-aided
Accuracy	low	medium	medium	high
Bandwidth	high	low	high	high
Noise level	high	very low	low	low

The individual objectives of this thesis are summarized as follows:

- To create a motion state estimation model based on MEMS inertial sensors, which combines rigid body motion kinematics of hydraulic manipulators with powerful signal processing methods;
- To show by experimental verification that the performance of the motion state estimation model is comparable and in certain respects superior to traditional instrumentation solutions; and
- To demonstrate on a full-scale heavy-duty hydraulic manipulator that a closed-loop motion control system utilising the surface-mounted low-cost inertial sensors achieves comparable motion control tracking performance compared to high-accuracy reference sensors.

1.5 Research methods and restrictions

The research begins by constructing a theoretical framework allowing the use of low-cost inertial sensors for multi-link manipulator motion sensing. The theoretical discussion and results regarding serial-link manipulator rigid body motion kinematics and complementary filtering of inertial measurements have been kept general without restrictions on any particular manipulator. The purpose is to allow wider applications of the results and relevance for future developments. However, the emphasis of this thesis is on manipulators with rotary joints. Later in the experimental section, custom-made single- and multi-link test benches are used along with a commercial HIAB 031 heavy-duty hydraulic manipulator.

The observation model is experimentally verified in an incremental manner beginning with a single-link case using one MEMS inertial sensor followed by multi-body motion experiments. The manipulator motion state estimation based on low-cost inertial sensors is referenced against high-cost, high-accuracy rotary encoder readings. After model verification, closed-loop motion control experiments are used to evaluate the performance of low-cost inertial sensing in manipulator motion control. Reference solutions are obtained here using the same high-accuracy encoder-type sensors.

The effects of temperature have not been included in the inertial sensor models due to the nearly constant ambient temperature during the experiments. If a wide range of temperatures is to be expected, the internal temperature reading provided by the MEMS sensors (see [73]) can be readily used to implement any necessary corrections.

Although MEMS accelerometers and angular rate gyroscopes allow 2-DOF inclination sensing based on the force of gravity, the experimental validation is restricted to 1-DOF joints in a vertical plane. The limitation on experimental validation is justified when considering the operation of forest harvesters and other mobile machine manipulators, for which load lifting and lowering tasks, i.e. vertical manipulator motions, are frequent and therefore of the most practical interest. Furthermore, heavy-duty hydraulic manipulators almost exclusively have 1-DOF joints. However, it should be noted that the underlying observation model itself is not restricted to 1-DOF joints. Thus, the MEMS-based motion sensing and its error propagation is founded on the exact same principles in a full 3-DOF case.

For completeness, however, a valid magnetometer model is also given (see Section 2.3), but its use is omitted for the sake of clarity. This is mostly because metallic structures typical in heavy-duty manipulators disrupt the Earth's magnetic field, thereby hindering the full 3-DOF rotation matrix estimation. Neither the kinematic modelling nor the associated complementary data fusion principles are actuator specific or limited to hydraulic manipulators.

1.6 Outline and contributions of the thesis

This thesis is divided into five chapters. The contents of each chapter are summarized below.

Chapter 1 is an introduction into the field of hydraulic manipulators and how MEMS inertial sensors relate to their motion state sensing and closed-loop motion control. The background and motivation for the study are given, followed by the objectives, research methods, restrictions and contributions of the thesis.

Chapter 2 contains a derivation of forward motion kinematics for serial-link manipulators and details the MEMS-based motion state estimation model, which is closely tied to complementary filtering of inertial measurements.

Chapter 3 presents the experimental validation of the proposed observation model in a test bench and application case examples of hydraulic manipulator closed-loop motion control.

Chapter 4 provides a commentary and an explanation of the results, and discusses their relevance.

Chapter 5 places the major findings of the research into a larger context and indicates the conclusions that can be drawn from the results. The chapter ends on recommendations for future work.

The main contributions of this research are as follows:

- A novel observation model for the full motion state estimation of serial link hydraulic manipulators based on low-resolution, low-cost MEMS inertial sensors;
- Thorough verification and characterisation of the observation model performance; and
- Case examples of MEMS-based closed-loop motion control systems for heavy-duty manipulators, which demonstrate control performance comparable to high-resolution, high-cost reference sensors.

The author has conducted all the controller design, experiments, and analysis of results relating to the motion control experiments, which have been reported in Honkakorpi et al. [74, 75, 76, 77]. The motion state estimation model and the related signal processing methods have been developed in co-operation with D.Sc. Juho Vihonen from TUT/DSP. The estimation model has been published with analysis in Vihonen et al. [78, 79], after which it has been reformulated by the author in accordance with standard robotics conventions and notations. Researchers Janne Koivumäki and

Erkki Lehto from TUT/IHA have contributed notably to the design and manufacture of the small-scale test bench and the MEMS sensor module. Prof. Jouni Mattila has acted as the supervisor of this thesis and has provided support, guidance and access to the necessary laboratory infrastructure for the experimental work.

Chapter 2

Multi-body motion state estimation with inertial sensors

In order to apply the inertial sensors to the motion state estimation of a serial-link hydraulic manipulator system, the velocities and accelerations of the interlinked mechanical bodies must be propagated through the kinematic chain to enable high-bandwidth, low-noise and low-delay sensing of the link rotations, angular velocities and angular accelerations. Thus, it becomes necessary to form generic expressions for the relevant kinematic quantities in a systematic way to arrive at a widely applicable approach. The following section provides the necessary serial-link manipulator forward kinematics, which are derived from widely known generic rigid-body motion kinematics. In Section 2.2, the novel multi-body observation model is formulated based on the previously derived manipulator kinematics. The use of MEMS inertial sensors is integrated with the observation model in Section 2.3, where the key theoretical findings of the proposed model are also presented. Finally, Section 2.4 discusses the fusion of the inertial measurements with complementary filtering.

2.1 Multi-link manipulator rigid body kinematics

As a starting point, this section presents a general rigid body motion kinematics model for an open-chain serial manipulator consisting of an arbitrary amount of rigid links. A more detailed discussion of the derivation of the motion kinematics can be found in Jazar [80] or Sciavicco and Siciliano [81], among others.

First, consider a rigid body with a fixed local coordinate frame $\{B\}$ $(oxyz)$ moving freely in a fixed global coordinate frame $\{G\}$ $(OXYZ)$ (see Figure 2.1). The position

vector ${}^{G}\mathbf{r}_P$ of a body point P with respect to the reference frame $\{G\}$ can be expressed using a unique rotation and translation:

$$ {}^{G}\mathbf{r}_P = {}^{G}R_B \, {}^{B}\mathbf{r}_P + {}^{G}\mathbf{d}_B, \tag{2.1} $$

where ${}^{B}\mathbf{r}_P$ is the position of P in $\{B\}$, ${}^{G}\mathbf{d}_B$ denotes the position of the moving origin o relative to the fixed global origin O and ${}^{G}R_B$ is a (3×3) rotation matrix, $\det(R) = 1$ and $R^{\mathrm{T}} = R^{-1}$, describing the relative rotation of the local frame $\{B\}$ with respect to $\{G\}$.

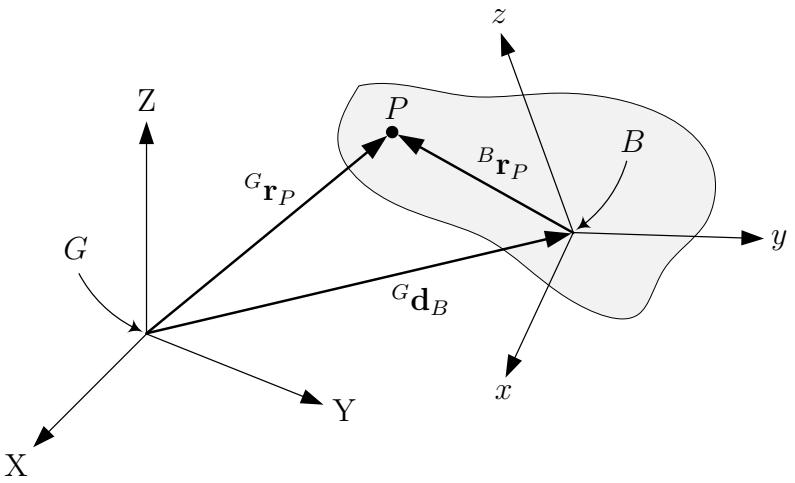

Figure 2.1: Ridig body point P represented in global and body frame.

Assuming the body frame in Figure 2.1 can rotate and translate freely in the global frame and the body point P is moving in frame $\{B\}$, the global velocity ${}^{G}\mathbf{v}_P$ of point P is derived by differentiating the body point position (2.1), which results in

$$ \begin{aligned} {}^{G}\mathbf{v}_P = {}^{G}\dot{\mathbf{r}}_P &= {}^{G}\dot{R}_B \, {}^{B}\mathbf{r}_P + {}^{G}R_B \, {}^{B}\dot{\mathbf{r}}_P + {}^{G}\dot{\mathbf{d}}_B \\ &= {}_{G}\boldsymbol{\omega}_B \times {}^{G}R_B \, {}^{B}\mathbf{r}_P + {}^{G}_{B}\dot{\mathbf{r}}_P + {}^{G}\dot{\mathbf{d}}_B \\ &= {}_{G}\boldsymbol{\omega}_B \times {}^{G}_{B}\mathbf{r}_P + {}^{G}_{B}\dot{\mathbf{r}}_P + {}^{G}\dot{\mathbf{d}}_B, \end{aligned} \tag{2.2} $$

where ${}_{G}\boldsymbol{\omega}_B$ denotes the instantaneous angular velocity of frame $\{B\}$ relative to $\{G\}$ and ${}^{G}_{B}\mathbf{r}_P$ is the position of P in frame $\{B\}$ expressed in the global frame $\{G\}$. Similarly, the acceleration can be derived by differentiating ${}^{G}\mathbf{v}_P$ to yield

$$
\begin{aligned}
{}^{G}\ddot{\mathbf{r}}_P = {}& {}_{G}\dot{\boldsymbol{\omega}}_B \times {}^{G}R_B\, {}^{B}\mathbf{r}_P + {}_{G}\boldsymbol{\omega}_B \times {}^{G}\dot{R}_B\, {}^{B}\mathbf{r}_P + {}_{G}\boldsymbol{\omega}_B \times {}^{G}R_B\, {}^{B}\dot{\mathbf{r}}_P \\
& + {}^{G}\dot{R}_B\, {}^{B}\dot{\mathbf{r}}_P + {}^{G}R_B\, {}^{B}\ddot{\mathbf{r}}_P + {}^{G}\ddot{\mathbf{d}}_B \\
= {}& {}_{G}\boldsymbol{\alpha}_B \times {}^{G}_{B}\mathbf{r}_P + {}_{G}\boldsymbol{\omega}_B \times ({}_{G}\boldsymbol{\omega}_B \times {}^{G}\mathbf{r}_P) + 2\,{}_{G}\boldsymbol{\omega}_B \times {}^{G}\dot{\mathbf{r}}_P \\
& + {}^{G}_{B}\dot{\mathbf{r}}_P + {}^{G}\ddot{\mathbf{d}}_B, \qquad (2.3)
\end{aligned}
$$

where ${}_{G}\boldsymbol{\alpha}_B$ is the instantaneous angular acceleration of $\{B\}$ with respect to $\{G\}$. If the body point P is fixed in $\{B\}$, the linear acceleration simplifies to

$$
{}^{G}\ddot{\mathbf{r}}_P = {}_{G}\boldsymbol{\alpha}_B \times {}^{G}_{B}\mathbf{r}_P + {}_{G}\boldsymbol{\omega}_B \times ({}_{G}\boldsymbol{\omega}_B \times {}^{G}_{B}\mathbf{r}_P) + {}^{G}\ddot{\mathbf{d}}_B. \qquad (2.4)
$$

Now, consider an open-chain serial manipulator consisting of $n+1$ rigid links connected by n 1-DOF prismatic or revolute joints. The base link 0 is immobile and fixed to the ground while link n is the end-effector link. By rigidly attaching body coordinate frames $\{B_i\}$ to each link i of the manipulator, the forward kinematics of the manipulator may be computed to determine the position, orientation, velocity and acceleration of each link with respect to the base coordinate frame. In general, the frames $\{B_i\}$ may be chosen arbitrarily as long as they are attached to the links they refer to. The frame placement adopted in Figure 2.2, however, follows the

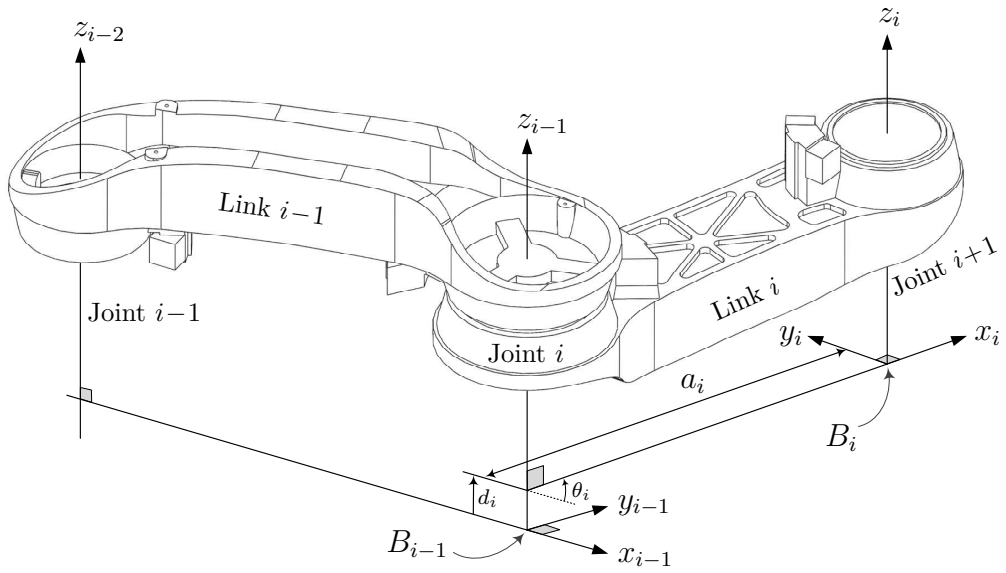

Figure 2.2: Characterisation of a serial link manipulator using the Denavit-Hartenberg (DH) method (link twist α_i is omitted for clarity).

widely adopted Denavit-Hartenberg (DH) standard method [82], in which the body frame $\{B_i\}$ is attached on link i at joint $i+1$. The relations between the link frames are characterised by joint angle θ_i, link length a_i, joint distance d_i and link twist α_i, which is the angle between the z_i and z_{i-1} axes about the x_i axis.

Now consider a generic link i of the manipulator where, according to the DH method, the base frame $\{B_i\}$ is attached to the link with its origin along the axis of joint $i+1$, while the frame $\{B_{i-1}\}$ has its origin along the axis of joint i, as shown in Figure 2.3.

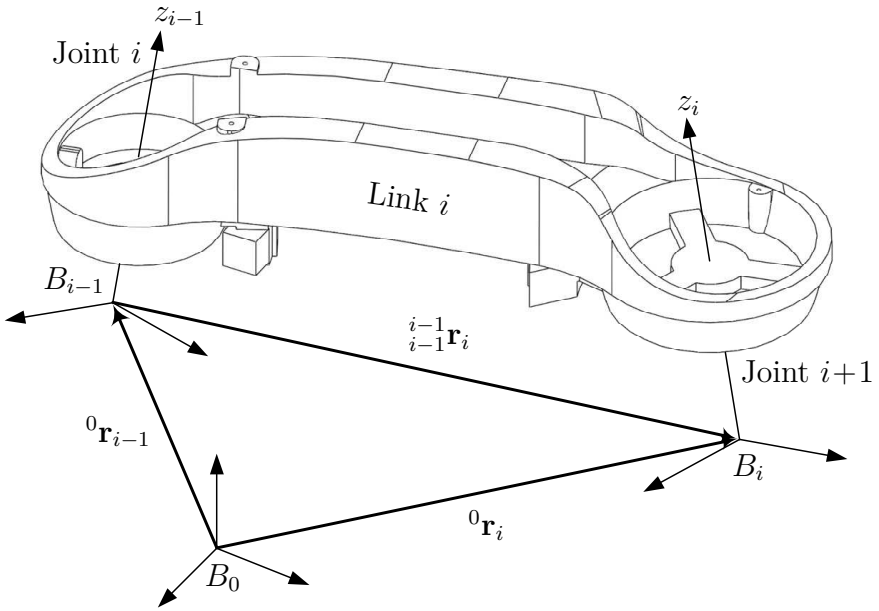

Figure 2.3: Characterisation of general link i of a serial manipulator.

According to the coordinate transform (2.1) one may write

$$ {}^0\mathbf{r}_i = {}^0\mathbf{r}_{i-1} + {}^0R_{i-1}\, {}^{i-1}_{i-1}\mathbf{r}_i, \tag{2.5} $$

where ${}^{i-1}_{i-1}\mathbf{r}_i$ denotes the position of frame $\{B_i\}$ with respect to $\{B_{i-1}\}$ expressed in frame $i-1$. The linear velocity of link i can now be expressed in the global frame using (2.2), which results in

$$ {}^0\dot{\mathbf{r}}_i = {}^0\dot{\mathbf{r}}_{i-1} + {}_0\boldsymbol{\omega}_{i-1} \times {}^0_{i-1}\mathbf{r}_i + {}^0_{i-1}\dot{\mathbf{r}}_i, \tag{2.6} $$

where ${}^{0}_{i-1}\dot{\mathbf{r}}_i$ denotes the velocity of frame $\{B_i\}$ with respect to frame $\{B_{i-1}\}$. The angular velocity of link i is derived by differentiating the composite rotation ${}^0R_i = {}^0R_{i-1}\,{}^{i-1}R_i$, which can be shown to lead to the recursive formula

$$ {}^{0}_{0}\boldsymbol{\omega}_i = {}^{0}_{0}\boldsymbol{\omega}_{i-1} + {}^{0}_{i-1}\boldsymbol{\omega}_i \tag{2.7} $$

or equivalently

$$ {}^{0}_{0}\boldsymbol{\omega}_i = \sum_{j=1}^{i} {}^{0}_{j-1}\boldsymbol{\omega}_j, \quad j \leq i. \tag{2.8} $$

Depending on the joint type, the angular velocity (2.7) has different expressions. For a revolute joint, the only rotation is about the z_{i-1} axis, and for a prismatic joint the orientation of frame $\{B_i\}$ with respect to frame $\{B_{i-1}\}$ does not change. This leads to

$$ {}^{0}_{0}\boldsymbol{\omega}_i = \begin{cases} {}^{0}_{0}\boldsymbol{\omega}_{i-1} + \dot{\theta}_i\,{}^0\hat{k}_{i-1} & \text{if joint } i \text{ is revolute} \\ {}^{0}_{0}\boldsymbol{\omega}_{i-1} & \text{if joint } i \text{ is prismatic,} \end{cases} \tag{2.9} $$

where θ_i is the revolute joint angle DH parameter and ${}^0\hat{k}_{i-1}$ is the unit vector of the joint i axis.

The linear velocity (2.6) may be expressed in a similar manner for different joint types. For a revolute joint the linear motion ${}^{0}_{i-1}\dot{\mathbf{r}}_i$ is due to the rotation of $\{B_i\}$ with respect to $\{B_{i-1}\}$ given by

$$ {}^{0}_{i-1}\dot{\mathbf{r}}_i = {}_{i-1}\boldsymbol{\omega}_i \times {}^{0}_{i-1}\mathbf{r}_i. \tag{2.10} $$

Because the only possible translation for a prismatic joint is along the z_{i-1} axis, the linear velocities can be given in view of (2.7) as

$$ {}^{0}_{0}\dot{\mathbf{r}}_i = \begin{cases} {}^0\dot{\mathbf{r}}_{i-1} + {}^{0}_{0}\boldsymbol{\omega}_i \times {}^{0}_{i-1}\mathbf{r}_i & \text{if joint } i \text{ is revolute} \\ {}^0\dot{\mathbf{r}}_{i-1} + \dot{d}_i\,{}^0\hat{k}_{i-1} + {}^{0}_{0}\boldsymbol{\omega}_i \times {}^{0}_{i-1}\mathbf{r}_i & \text{if joint } i \text{ is prismatic,} \end{cases} \tag{2.11} $$

where d is the DH parameter of the prismatic joint. The link angular acceleration is derived by differentiating the velocity (2.9) to yield

$$ {}^{0}_{0}\dot{\boldsymbol{\omega}}_i = \begin{cases} {}^{0}_{0}\dot{\boldsymbol{\omega}}_{i-1} + \ddot{\theta}_i\, {}^{0}\hat{k}_{i-1} + {}^{0}_{0}\boldsymbol{\omega}_{i-1} \times \dot{\theta}_i\, {}^{0}\hat{k}_{i-1} & \text{if joint } i \text{ is revolute} \\ {}^{0}_{0}\dot{\boldsymbol{\omega}}_{i-1} & \text{if joint } i \text{ is prismatic.} \end{cases} \tag{2.12} $$

Similarly, the linear acceleration is obtained by differentiating (2.11), which results in

$$ {}^{0}_{0}\ddot{\mathbf{r}}_i = \begin{cases} {}^{0}\ddot{\mathbf{r}}_{i-1} + {}^{0}_{0}\dot{\boldsymbol{\omega}}_i \times {}^{0}_{i-1}\mathbf{r}_i + {}^{0}_{0}\boldsymbol{\omega}_i \times ({}^{0}_{0}\boldsymbol{\omega}_i \times {}^{0}_{i-1}\mathbf{r}_i) & \text{if joint } i \text{ is revolute} \\ {}^{0}\ddot{\mathbf{r}}_{i-1} + \ddot{d}_i\, {}^{0}\hat{k}_{i-1} + 2\dot{d}\, {}^{0}_{0}\boldsymbol{\omega}_i \times {}^{0}\hat{k}_{i-1} + {}^{0}_{0}\boldsymbol{\omega}_i \times ({}^{0}_{0}\boldsymbol{\omega}_i \times {}^{0}_{i-1}\mathbf{r}_i) & \text{if joint } i \text{ is prismatic.} \end{cases} \tag{2.13} $$

Now, if all manipulator joints are revolute, in view of (2.8) the linear acceleration of frame $\{B_i\}$ can be expressed using relative link velocities and accelerations as

$$ {}^{0}_{0}\ddot{\mathbf{r}}_i = \sum_{j=1}^{i} \Big(\sum_{m=1}^{j} {}^{0}_{m-1}\dot{\boldsymbol{\omega}}_m \times {}^{0}_{j-1}\mathbf{r}_j + \sum_{m=1}^{j} {}^{0}_{m-1}\boldsymbol{\omega}_m \times \Big(\sum_{m=1}^{j} {}^{0}_{m-1}\boldsymbol{\omega}_m \times {}^{0}_{j-1}\mathbf{r}_j \Big) \Big), \tag{2.14} $$

where ${}^{0}_{m-1}\dot{\boldsymbol{\omega}}_m$ denotes the angular acceleration of frame $\{B_m\}$ with respect to $\{B_{m-1}\}$.

2.2 Multi-body observation model

The derived multi-body manipulator kinematics can now be applied to construct a "geometry-aided" observation model that can be used to solve the link rotations, angular velocities and angular accelerations with respect to the inertial reference frame.

Consider again an open-chain manipulator fixed to a stationary base platform with $n+1$ rigid links connected by n rotary joints. Resembling the previously discussed DH method, body coordinate frames $\{B_i\}$ of rectangular (xyz) axes are rigidly attached to the distal end of each link i at joint $i+1$. The orientation of the axes is chosen such that the y axis of frame $\{B_i\}$ intersects the origin of $\{B_{i-1}\}$. The kinematic chain is illustrated in Figure 2.4, and the lengths of the links are denoted by l_i.

Let ${}^{I}R_i$ denote the (3×3) body-fixed rotation matrix, $\det({}^{I}R_i)=1$ and ${}^{I}R_i^{\mathrm{T}} = {}^{I}R_i^{-1}$, relating the orientation of $\{B_i\}$ to the inertial reference frame $\{I\}$. If all joint angular

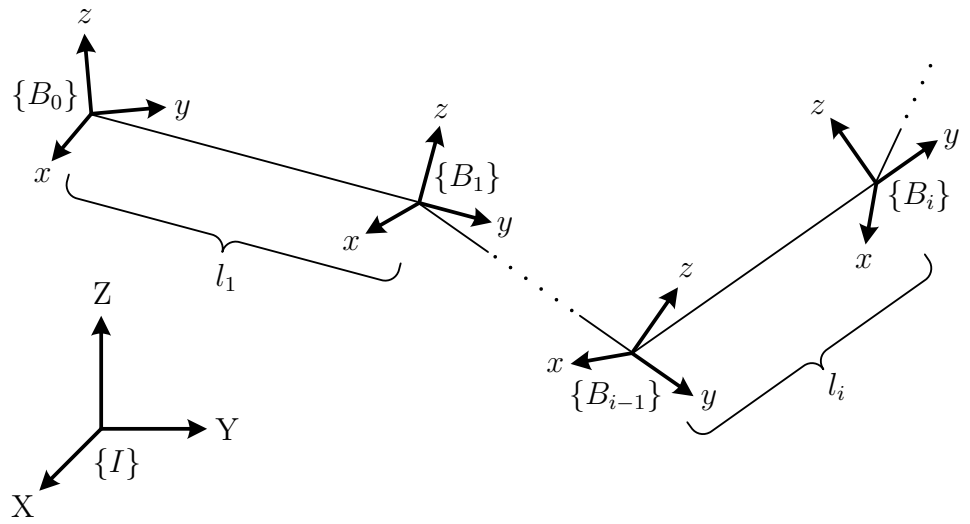

Figure 2.4: Open chain manipulator rigid body observation model.

velocities are expressed in their respective body-fixed frames, the ith link velocity (2.8) with respect to $\{I\}$ may be written as[1]

$$ {}^{i}\boldsymbol{\omega}_i = {}^{i}_{i-1}\boldsymbol{\omega}_i + \sum_{m=1}^{i-1} R_i^{\mathrm{T}} R_m \, {}^{m}_{m-1}\boldsymbol{\omega}_m \tag{2.15} $$

denoting that the angular velocity of the ith link, expressed in frame $\{B_i\}$, consists of the angular velocity of the ith joint and of a summation of the joint angular velocities up to $i-1$. Now assume a second body-fixed frame $\{P_i^0\}$ is rigidly attached on link i at a fixed distance from $\{B_{i-1}\}$ and rotated to the same orientation as $\{B_i\}$, as shown in Figure 2.5. Since the rigid body angular velocity and angular acceleration of $\{P_i^0\}$ and $\{B_i\}$ are the same, in view of (2.14) the linear acceleration of $\{P_i^0\}$ with respect to $\{I\}$, expressed in $\{B_i\}$, can be given using body-referenced angular velocities and accelerations as

$$ \begin{aligned} {}^{i}\dot{\mathbf{v}}_{P_i^0} = \sum_{j=1}^{i} \Bigg(\sum_{m=1}^{j} R_i^{\mathrm{T}} R_m \, {}^{m}_{m-1}\boldsymbol{\alpha}_m \times R_i^{\mathrm{T}} R_j \, {}^{j}_{j-1}\mathbf{r}_j + \sum_{m=1}^{j} R_i^{\mathrm{T}} R_m \, {}^{m}_{m-1}\boldsymbol{\omega}_m \\ \times \Big(\sum_{m=1}^{j} R_i^{\mathrm{T}} R_m \, {}^{m}_{m-1}\boldsymbol{\omega}_m \times R_i^{\mathrm{T}} R_j \, {}^{j}_{j-1}\mathbf{r}_j \Big) \Bigg), \end{aligned} \tag{2.16} $$

[1]Hereafter in this section, sub- and superscripts "I" are omitted for quantities referred to the inertial reference frame $\{I\}$.

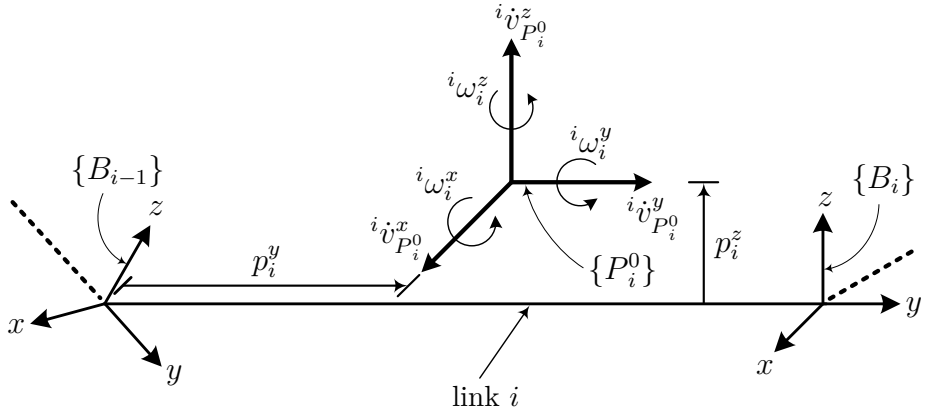

Figure 2.5: Secondary frame $\{P_i^0\}$ rigidly attached on the ith link with linear acceleration and angular velocity axial components shown. Note that ${}^{i}\boldsymbol{\omega}_{P_i^0} = {}^{i}\boldsymbol{\omega}_i$.

where ${}^{m}_{m-1}\boldsymbol{\omega}_m$ is the mth joint angular velocity expressed in frame $\{B_m\}$ and ${}^{m}_{m-1}\boldsymbol{\alpha}_m$ denotes the angular acceleration of joint m given by

$$ {}^{m}_{m-1}\boldsymbol{\alpha}_m = {}^{m}_{m-1}\dot{\boldsymbol{\omega}}_m, \tag{2.17} $$

and the distance between frames, denoted by ${}^{j}_{j-1}\mathbf{r}_j$, is defined as

$$ {}^{j}_{j-1}\mathbf{r}_j = \begin{cases} [0 \; l_j \; 0]^{\mathrm{T}}, & j < i \\ [0 \; p_i^y \; p_i^z]^{\mathrm{T}}, & j = i. \end{cases} \tag{2.18} $$

2.2.1 Direct algebraic solution of joint angular acceleration

Recall that calculating the differential (2.17) on a real-world system to obtain the joint angular acceleration causes a considerable density of superimposed high-frequency perturbations on the resulting angular acceleration as previously discussed in Section 1.1. Therefore, it is desirable to derive the angular acceleration directly without noise-amplifying differentiation. This section provides a direct algebraic solution for the joint angular acceleration, inspired by Padgaonkar et al. [83], based on linear accelerations and angular velocities.

Assume two further body-fixed frames $\{P_i^1\}$ and $\{P_i^2\}$ are rigidly attached on link i at known distances from $\{B_{i-1}\}$ in the same orientation as $\{B_i\}$. For the direct angular acceleration solution, only three additional linear acceleration components are required: along the z axis of frame $\{P_i^1\}$ and along the yz axes of frame $\{P_i^2\}$,

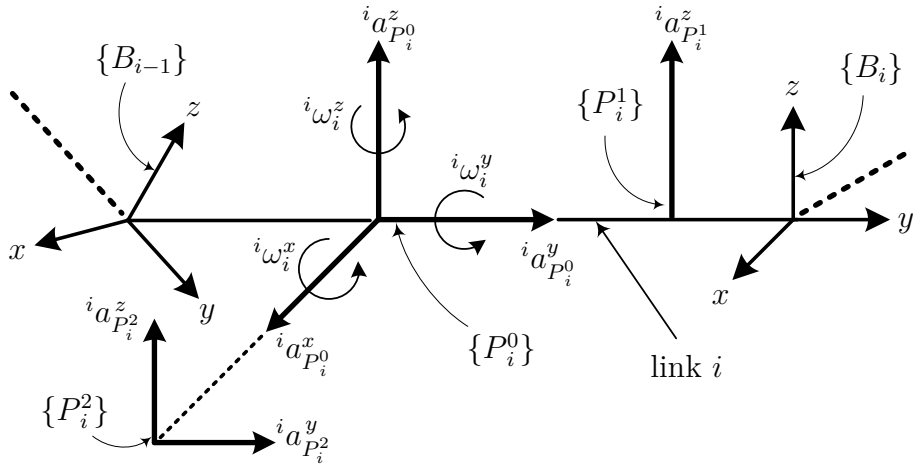

Figure 2.6: A configuration of additional body-fixed frames $\{P_i^1\}$ and $\{P_i^2\}$ rigidly attached to the ith link. Here $p_i^z = 0$ for clarity.

which is illustrated in Figure 2.6. In view of (2.4), the linear accelerations of $\{P_i^j\}$ expressed in $\{B_i\}$ are

$$^{i}\mathbf{a}_{P_i^j} = {}^{i}\ddot{\mathbf{r}}_i + {}^{i}\boldsymbol{\alpha}_i \times ({}^{i}\mathbf{r}_{P_i^j} - {}^{i}\mathbf{r}_i) + {}^{i}\boldsymbol{\omega}_i \times ({}^{i}\boldsymbol{\omega}_i \times ({}^{i}\mathbf{r}_{P_i^j} - {}^{i}\mathbf{r}_i)), \quad j = 0, 1, 2, \tag{2.19}$$

where $^{i}\ddot{\mathbf{r}}_i$ denotes the linear acceleration of $\{B_i\}$ and $({}^{i}\mathbf{r}_{P_i^j} - {}^{i}\mathbf{r}_i)$ equals the local position vector in (2.4). The angular acceleration of link i can be given in view of (2.12) as

$$^{i}\boldsymbol{\alpha}_i = {}^{i}\boldsymbol{\alpha}_{i-1} + {}^{i}_{i-1}\boldsymbol{\alpha}_i + {}^{i}\boldsymbol{\omega}_{i-1} \times {}^{i}\boldsymbol{\omega}_i. \tag{2.20}$$

Substituting (2.20) into (2.19) and solving for $^{i}\ddot{\mathbf{r}}_i$ yields

$$\begin{aligned} {}^{i}\ddot{\mathbf{r}}_i = {}^{i}\mathbf{a}_{P_i^j} - ({}^{i}\boldsymbol{\alpha}_{i-1} + {}^{i}_{i-1}\boldsymbol{\alpha}_i + {}^{i}\boldsymbol{\omega}_{i-1} \times {}^{i}\boldsymbol{\omega}_i) \times ({}^{i}\mathbf{r}_{P_i^j} - {}^{i}\mathbf{r}_i) \\ - {}^{i}\boldsymbol{\omega}_i \times ({}^{i}\boldsymbol{\omega}_i \times ({}^{i}\mathbf{r}_{P_i^j} - {}^{i}\mathbf{r}_i)). \end{aligned} \tag{2.21}$$

Equating the expression of $^{i}\ddot{\mathbf{r}}_i$ for frames $\{P_i^0\}$, $\{P_i^1\}$ and for $\{P_i^0\}$, $\{P_i^2\}$ results in

$$\begin{aligned} {}^{i}\mathbf{a}_{P_i^j} - {}^{i}\mathbf{a}_{P_i^0} = {}^{i}\boldsymbol{\alpha}_{i-1} \times ({}^{i}\mathbf{r}_{P_i^j} - {}^{i}\mathbf{r}_{P_i^0}) + {}^{i}_{i-1}\boldsymbol{\alpha}_i \times ({}^{i}\mathbf{r}_{P_i^j} - {}^{i}\mathbf{r}_{P_i^0}) \\ + {}^{i}\boldsymbol{\omega}_{i-1} \times {}^{i}\boldsymbol{\omega}_i \times ({}^{i}\mathbf{r}_{P_i^j} - {}^{i}\mathbf{r}_{P_i^0}) + {}^{i}\boldsymbol{\omega}_i \times {}^{i}\boldsymbol{\omega}_i \times ({}^{i}\mathbf{r}_{P_i^j} - {}^{i}\mathbf{r}_{P_i^0}), \quad j = 1, 2. \end{aligned} \tag{2.22}$$

By virtue of the placement of the frames illustrated in Figure 2.6, the position vectors are

$$ {}^{i}\mathbf{r}_{P_i^1} = {}^{i}\mathbf{r}_{P_i^0} + \begin{bmatrix} 0 \\ d_i^{y_1} \\ 0 \end{bmatrix}, {}^{i}\mathbf{r}_{P_i^2} = {}^{i}\mathbf{r}_{P_i^0} + \begin{bmatrix} d_i^{x_2} \\ 0 \\ 0 \end{bmatrix}, \tag{2.23} $$

where $d_i^{y_1} > 0$ and $d_i^{x_2} > 0$. Now, substituting the respective position vectors (2.23) into (2.22) and considering the available acceleration axis components at $\{P_i^1\}$ and $\{P_i^2\}$, the component-wise direct algebraic solution of the joint i angular acceleration becomes

$$ {}^{i}_{i-1}\boldsymbol{\alpha}_i = \begin{bmatrix} ({}^{i}a^z_{P_i^1} - {}^{i}a^z_{P_i^0})/d_i^{y_1} - {}^{i}\omega_i^y\,{}^{i}\omega_i^z - {}^{i}\omega_{i-1}^y\,{}^{i}\omega_i^z \\ -({}^{i}a^z_{P_i^2} - {}^{i}a^z_{P_i^0})/d_i^{x_2} + {}^{i}\omega_i^x\,{}^{i}\omega_i^z + {}^{i}\omega_{i-1}^x\,{}^{i}\omega_i^z \\ ({}^{i}a^y_{P_i^2} - {}^{i}a^y_{P_i^0})/d_i^{x_2} - {}^{i}\omega_i^x\,{}^{i}\omega_i^y - {}^{i}\omega_{i-1}^x\,{}^{i}\omega_i^y \end{bmatrix} - {}^{i}\boldsymbol{\alpha}_{i-1}, \tag{2.24} $$

where the superscripts x, y and z denote the respective axis components of the kinematic quantities and

$$ {}^{i}\boldsymbol{\alpha}_{i-1} = \sum_{m=1}^{i-1} R_i^{\mathrm{T}} R_m \, {}^{m}_{m-1}\boldsymbol{\alpha}_m. \tag{2.25} $$

Note that the angular acceleration axis components in (2.24) require prior knowledge of the angular velocities about the xyz axes, but only three extra linear acceleration components co-directional with the y and z axis of frame $\{P_i^0\}$ are needed.

2.3 Motion sensing with inertial sensors

A typical IMU contains a 3-axis accelerometer, a 3-axis gyroscope and often a 3-axis magnetometer providing heading information. The reference frame of the IMU is the body-fixed frame $\{B\}$, which is central in inertial measurements. The inertial reference frame in which Newtonian mechanics are used is denoted by $\{I\}$, as before.

A *gyroscope* measures the angular velocity in the body-frame $\{B\}$ with respect to the inertial frame $\{I\}$. By integrating the angular velocity, the relative orientation between the frames in $\{B\}$ with respect to a chosen initial value is obtained.

In practice, the angular rate output of a 3-axis MEMS gyroscope can be characterized (see e.g. Mahony et al. [61]) by an additive bias term and noise component as

$$ {}^{B}_{I}\boldsymbol{\Omega}_{B} = (I + S_g)\,{}^{B}_{I}\boldsymbol{\omega}_{B} + \mathbf{b}_g + \boldsymbol{\mu}_g \in \mathbb{R}^{3\times 1}, \tag{2.26} $$

where ${}^{B}_{I}\boldsymbol{\omega}_{B}$ denotes the true angular rate of $\{B\}$ with respect to $\{I\}$ expressed in the body frame $\{B\}$, I is the identity matrix, S_g is a scale factor error expressed as a percentage of $\boldsymbol{\omega}$, $\mathbf{b}_g$ denotes a constant or slowly varying gyro bias and $\boldsymbol{\mu}_g$ denotes additive measurement noise.

An *accelerometer* measures the instantaneous linear accelerations $\dot{\mathbf{v}}$ in the body-fixed frame $\{B\}$ relative to $\{I\}$ minus the local gravitational acceleration field $\mathbf{g}_0$ in $\{I\}$. The linear acceleration output of a 3-axis MEMS accelerometer can be expressed by

$$ {}^{B}_{I}\mathbf{a}_{B} = (I + S_a)({}^{B}_{I}\dot{\mathbf{v}}_{B} - {}^{I}R^{\mathrm{T}}_{B}\,{}^{I}\mathbf{g}) + \mathbf{b}_a + \boldsymbol{\mu}_a \in \mathbb{R}^{3\times 1}, \tag{2.27} $$

where S_a is a scale factor error, $\dot{\mathbf{v}}$ denotes the true instantaneous linear acceleration, ${}^{I}R_{B}$ describes the rotation of $\{B\}$ with respect to $\{I\}$, $\mathbf{b}_a$ is a bias term and $\boldsymbol{\mu}_a$ denotes additive measurement noise. In a static situation, the gravitational field $\mathbf{g} = |\mathbf{g}_0|\mathbf{e}_3$, where $|\mathbf{g}_0| \approx 9.8$ m/s^2, dominates the value of $\mathbf{a}$. Thus, it is common to use

$$ \frac{{}^{B}_{I}\mathbf{a}_{B}}{\|{}^{B}_{I}\mathbf{a}_{B}\|} \approx -\,{}^{I}R^{\mathrm{T}}_{B}\,\mathbf{e}_3 \tag{2.28} $$

as a low-frequency estimate of the inertial frame $\{I\}$ z axis expressed in the body-fixed frame $\{B\}$.

A *magnetometer* measures the Earth's magnetic field

$$ {}^{B}_{I}\mathbf{m}_{B} = {}^{I}R^{\mathrm{T}}_{B}\,{}^{I}\mathbf{m} + {}^{B}\mathbf{b}_m + \boldsymbol{\mu}_m \in \mathbb{R}^{3\times 1}, \tag{2.29} $$

where ${}^{I}\mathbf{m}$ is the Earth's magnetic field in the inertial frame $\{I\}$, ${}^{B}\mathbf{b}_m$ is a magnetic disturbance in the body-fixed frame $\{B\}$ and $\boldsymbol{\mu}_m$ denotes additive measurement noise. Since only the direction of the magnetometer output is relevant, the output is normalised as

$$ \mathbf{v}_m = \frac{{}^{B}_{I}\mathbf{m}_{B}}{\|{}^{B}_{I}\mathbf{m}_{B}\|} \tag{2.30} $$

to a direction vector. The measurement noise $\boldsymbol{\mu}_m$ can usually be considered low, but the local magnetic disturbance ${}^{B}\mathbf{b}_m$ can be significant, especially in indoor

environments or if electric motors are operated in the immediate vicinity of the magnetometer.

The measured vectors (2.28) and (2.30) can be used to estimate the rotation ${}^{I}R_{B}$ (see Markley [84]). However, due the difficult characterization multi-sensor measurement error sources, a direct algebraic solution of the rotation would lead to a complex optimization problem. On the other hand, the operating environment may render accelerometer and magnetometer readings unusable, due to e.g. magnetic anomalies and accelerative motions. In this case, resolving the vectorial measurements into a unique instantaneous algebraic measurement of attitude would become infeasible. Since accelerometer and magnetometer readings are imprecise, the performance of the gyroscope of becomes vital.

Consider again Figure 2.5, and assume now that a triaxial MEMS accelerometer and a triaxial MEMS gyroscope is attached to the origin of $\{P_i^0\}$ with the sensitive axes coincident with the axes of $\{P_i^0\}$. Given that the base frame $\{B_0\}$ is stationary, it is assumed that $R_0 = I$ and ${}^{0}\boldsymbol{\omega}_0 = {}^{0}\boldsymbol{\alpha}_0 = [0\ 0\ 0]^{\mathrm{T}}$ for clarity. Additionally, the z axis rotation of R_i is taken for granted since it is not observable from the accelerometer readings as previously discussed. To construct a 2-DOF estimate of the true rotation R_i from the accelerometer readings (2.27), a complete definition of (2.16) is required. For a high-bandwidth low-delay estimate, identifying the gyroscope bias in (2.26) is also necessary. As a step toward perfecting both at once, the postulated model is applied in a suboptimal manner since the signals (2.26) and (2.27) may not be modelled as random processes with fully known spectral characteristics as previously discussed. Subsequently, the Earth's angular rate (15 deg/h) is neglected because of the low MEMS sensitivity and large noise density.

Applying (2.15), an estimate of the angular velocity of the ith joint, as sensed by a MEMS angular rate gyroscope attached to the origin of $\{P_i^0\}$, can be given by

$$ {}^{i}_{i-1}\hat{\boldsymbol{\omega}}_i = {}^{i}\boldsymbol{\Omega}_i + \hat{\mathbf{b}}_{g_i} - \sum_{m=1}^{i-1} \hat{R}_i^{\mathrm{T}} \hat{R}_m \, {}^{m}_{m-1}\hat{\boldsymbol{\omega}}_m, \tag{2.31} $$

where ${}^{i}\boldsymbol{\Omega}_i$ is the ith gyro rate reading as given by (2.26). Here the term $\hat{\mathbf{b}}_{g_i}$ is introduced to cancel the bias in ${}^{i}\boldsymbol{\Omega}_i$. Conversely, the differentiation

$$ {}^{i}_{i-1}\hat{\boldsymbol{\alpha}}_i = {}^{i}_{i-1}\dot{\hat{\boldsymbol{\omega}}}_i \tag{2.32} $$

yields a bias-free estimate of the ith joint angular acceleration, although it is generally plagued by high-frequency perturbations as the differentiation amplifies noise. By replacing the true angular acceleration and angular velocity in (2.16) with (2.31) and

(2.32), an algebraic estimate of the instantaneous linear acceleration ${}^{i}\hat{\dot{\mathbf{v}}}_{P_i^0}$ may be calculated. The estimate can be characterised as

$$ {}^{i}\hat{\dot{\mathbf{v}}}_{P_i^0} = {}^{i}\dot{\mathbf{v}}_{P_i^0} + \mathbf{b}_v^i + \boldsymbol{\mu}_v^i, \tag{2.33} $$

where $\mathbf{b}_v^i$ is a bias term and $\boldsymbol{\mu}_v^i$ denotes additive noise accumulated from different sensors, each with its own error characteristics.

For an accelerometer (2.27) located at $\{P_i^0\}$, the above now yields

$$ {}^{i}\mathbf{a}_{P_i^0} - {}^{i}\hat{\dot{\mathbf{v}}}_{P_i^0} \approx -R_i^{\mathrm{T}}\mathbf{g} \tag{2.34} $$

for which the required estimates of angular velocity (2.31) and acceleration (2.32) can be obtained without complicated transforms as previously discussed.

As a key result, the finding (2.34) states that a 2-DOF estimate of the rotation of $\{B_i\}$ with respect to the inertial reference frame $\{I\}$ can be constructed from the gravitational field even when the manipulator links are in accelerative motion. This applies to small angle rotations occurring between successive real-time updates of the link-wise rotations. In other words, it is assumed that the previous estimate of R_i can be used to update the inclination estimate, i.e. the link rotations occurring between two samples are small. A sampling rate that is high enough is thereby required.

Moreover, the angular acceleration estimate using the direct algebraic solution (2.24) can be characterized in the familiar form as

$$ {}^{i}_{i-1}\hat{\boldsymbol{\alpha}}_i = {}^{i}_{i-1}\boldsymbol{\alpha}_i + \mathbf{b}_\alpha^i + \boldsymbol{\mu}_\alpha^i, \tag{2.35} $$

where $\mathbf{b}_\alpha^i$ is a low-frequency bias term and $\boldsymbol{\mu}_\alpha^i$ denotes higher frequency perturbations accumulated from different sensors. The low-frequency bias in (2.35) can be removed without unwanted delay with a complementary I-type control design

$$ \begin{cases} {}^{i}_{i-1}\hat{\boldsymbol{\alpha}}_i^{\mathrm{I}} = {}^{i}_{i-1}\hat{\boldsymbol{\alpha}}_i + \hat{\mathbf{b}}_\alpha^i \\ \dot{\hat{\mathbf{b}}}_\alpha^{\,i} = k_{\mathrm{I}}({}^{i}_{i-1}\dot{\hat{\boldsymbol{\omega}}}_i - {}^{i}_{i-1}\hat{\boldsymbol{\alpha}}_i^{\mathrm{I}}), \end{cases} \tag{2.36} $$

since the gyro-based estimate (2.32) is bias-free but plagued by high-frequency perturbations due to the differentiation. Assuming the gyroscopes are low-noise with identified bias values, computing the angular acceleration algebraically in circular

motion and omitting all the scale factor errors embedded in (2.35), the true ith joint angular acceleration is obtained by

$$\lim_{d_i^{y_1},\, d_i^{x_2}\to\infty} {}^{i}_{i-1}\hat{\boldsymbol{\alpha}}_i = {}^{i}_{i-1}\boldsymbol{\alpha}_i. \tag{2.37}$$

In view of the target application domain of heavy-duty hydraulic manipulators, which have considerable mass of inertia and low natural frequencies of motion, the axial components of angular velocities in (2.24) do not play a significant role. This leads to a second key theoretical finding, which states that the perturbation contributions $\mathbf{b}_\alpha^i$ and $\boldsymbol{\mu}_\alpha^i$ are mostly proportional to the physical distances between the z axis and the yz axial accelerometers at $\{P_i^1\}$ and $\{P_i^2\}$ with respect to the triaxial accelerometer at $\{P_i^0\}$. In practice, however, the sensing ranges, sensor misalignment and linearity affect the direct sensing (2.24) performance.

2.4 Complementary filtering

A low-delay filtered estimate of the true rotation R_i can be solved by combining the gyroscope readings with measurements from other inertial sensors or information sources, which typically have low resolutions. These measurements, which contain mostly high-frequency perturbations, are used as a long-term reference for real-time identification of the gyroscope bias values to produce smoothed real-time estimates of R_i.

Consider the problem of combining two redundant noisy measurements, accelerometer and gyroscope readings, of the same rotation in such a way that the individual error sources are minimised while avoiding any unnecessary delay or distortion in the filtering process. A classic two-input single-output linear complementary filter with unity gain simultaneously implements a low-pass and a high-pass filter. As shown in Figures 2.7(a) and 2.7(b), where $F(s)$ is the Laplace transform of the low-pass filter, the input x_1 is the measured rate signal containing low-frequency noise, the input x_2 is the algebraic estimate of angle with a high-frequency noise component and $\hat{y}$ is the filtered output in the body-fixed frame $\{B\}$ with respect to the inertial frame $\{I\}$. By choosing

$$F(s) = \frac{C(s)}{s + C(s)}, \tag{2.38}$$

the Laplace transform of the complementary filter output in Figure 2.7 is

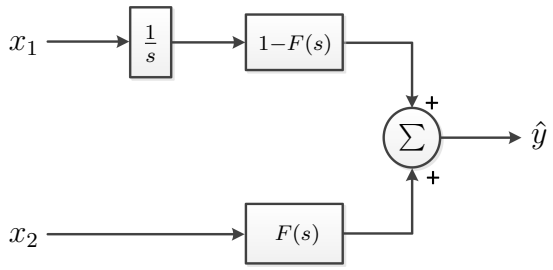

(a) Wiener filter structure.

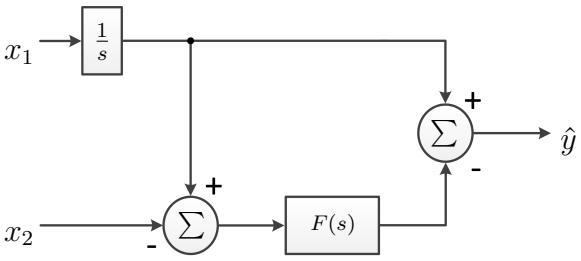

(b) Differencing and feed-forward configuration.

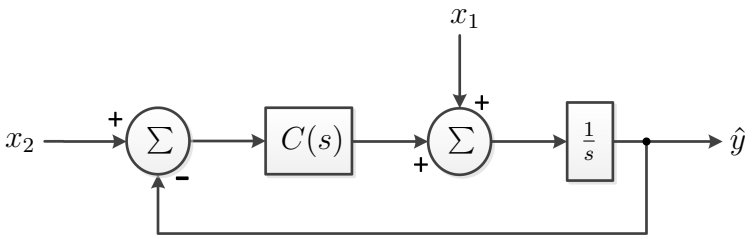

(c) Feedback complementary filter.

Figure 2.7: Complementary filter realizations.

$$\begin{aligned} \hat{y}(s) &= \frac{s}{s+C(s)}\frac{x_1(s)}{s} + \frac{C(s)}{s+C(s)}x_2(s) \\ &= (1-F(s))\frac{x_1(s)}{s} + F(s)x_2(s). \end{aligned} \tag{2.39}$$

Although all the filter realisation structures in Figure 2.7 are identical in theory and the configuration of the separate high- and low-pass filters is useful for understanding the basic concept of complementary filtering, most practical implementations exploit the complementary sensitivity structure of a linear feedback system subject to load disturbance. Thus, the feedback design illustrated in Figure 2.7(c) is chosen to maximize numerical stability and to ensure that the integrator process remains bounded by the accelerometer reference value, given that the accelerometer inclination reference provides a redundant measurement of the same rotation. Here the term $C(s)$ determines the controller type, which can be chosen according to classical control design techniques. The simplest choice is the proportional controller, i.e. $C(s) = k_P$, where the proportional gain k_P sets the cross-over frequency of the filters at k_P rad/s.

The frequency is chosen as a trade-off between the low-pass characteristics of x_2 and the low-frequency noise characteristics of x_1. See Higgins [85] for a detailed discussion about the relationship between the complementary filter designed in the frequency domain and the Kalman filter designed in the time domain.

If the gyroscope bias can be assumed constant or slowly time-varying, choosing

$$C(s) = k_{\mathrm{P}} + \frac{k_{\mathrm{I}}}{s} \tag{2.40}$$

yields a conventional proportional-integral (PI)-type control design. The filter can be given in state space form with the dynamics

$$\dot{\hat{y}} = x_1 + \hat{b} + k_{\mathrm{P}}(x_2 - \hat{y}) \tag{2.41}$$

$$\dot{\hat{b}} = k_{\mathrm{I}}(x_2 - \hat{y}). \tag{2.42}$$

Note that this linear proportional-integral type filter is well-suited for 1-DOF joint rotation angle estimation, which is a general problem in hydraulic manipulator control systems. For a full 3-DOF realisation, the above can be replaced with the quaternion representation, which is almost exclusively used in e.g. the attitude calculation of unmanned aerial vehicles and for expressing rotations and heading in the related geometry. This is mainly because although the Euler angles are intuitive as such, they may prove difficult to apply since their representation requires online algebraic manipulation and they are known to contain singularities.

Chapter 3

Experiments

This chapter presents the results of the experimental work done on the motion model verification as well as case examples of utilising the estimation model in the feedback loop of hydraulic manipulator closed-loop control systems. The following section summarises the initial experiments, in which the performance of a single MEMS sensor module for the motion sensing and closed-loop control of a single-link hydraulic boom was examined. In Section 3.2, the multi-body observation model performance is characterised on a three-link planar test bench, including the use of multiple MEMS sensors per link (see Figure 2.6). Finally, Section 3.3 summarises the closed-loop motion control experiments of multi-link hydraulic manipulators, with case examples of a suspended load anti-sway control system and hydraulic manipulator state feedback control.

3.1 Initial single-body experiments

In this section, the MEMS-based motion sensing is applied to the closed-loop motion control of a single-link hydraulic boom. In the experimental setup, the MEMS sensor module was placed very close to the rotation centre of the single joint, which keeps the motion acceleration components exerted on the sensor to a minimum. Thus, the key theoretical result (2.34) regarding the link rotation reconstruction from sensed gravity components can be directly applied here, assuming negligible linear acceleration components. The single-axis boom was controlled using the state feedback controller of Figure 1.3, with the single MEMS sensor module providing the full motion state feedback. The experimental work published in Honkakorpi et al. [74, 75] is summarised in the following.

In order to fulfil the requirements for a sensor fit for mobile machine use as previously discussed in Chapter 1, the MEMS sensor module must be robust and easy to install. For a straightforward surface installation onto hydraulic manipulators and interfacing to the control system, additional electronics and a sturdy enclosure are needed. The MEMS sensor chip used in this study is the model SCC1300-D02 by Murata [73] (formerly VTI Technologies), measuring 8.5 × 18.7 × 4.5 mm in size. It contains a digital three-axis $\pm 2g$ linear accelerometer integrated with a one x axis ±100 deg/s angular rate gyroscope. The digital output of the accelerometer has a resolution of 0.56 mg per least significant bit (LSB) which translates into a best-case inclination resolution of 0.032 deg when parallel to the ground. The MEMS gyroscope angular rate resolution is 0.02 deg/s. The frequency ranges of the MEMS components are 30 Hz for the accelerometer and up to 50 Hz for the gyroscope. Figure 3.1 illustrates the sensor module that has been constructed by combining the MEMS chip with a 16-bit hybrid signal microcontroller unit (MCU) and a line driver chip for implementing low-level data operations and controller area network (CAN) communication. Packaged into a 120 × 40 × 30 mm size dust- and waterproof robust aluminium enclosure, the module has tolerance against the harsh working conditions of mobile machines. Further shock and vibration resistance can be attained by filling the enclosure with epoxy. These characteristics make the sensor module easy to install and well suited for retrofit-type integration into existing control systems of mobile machines.

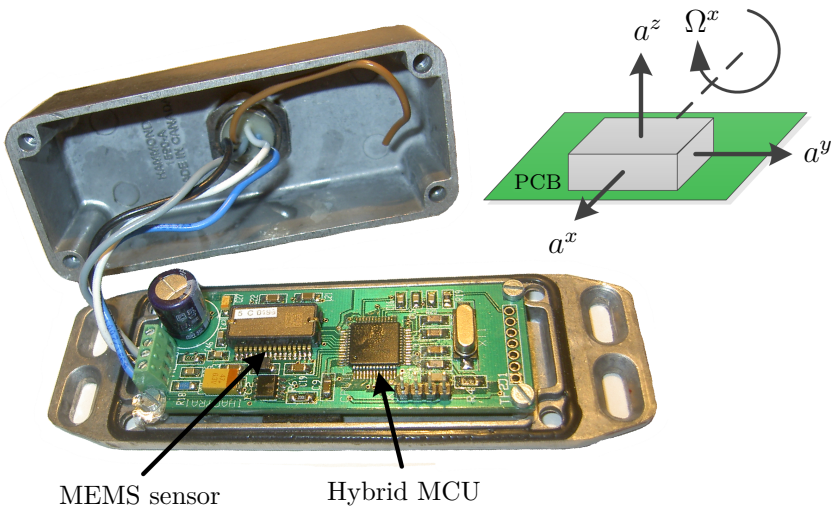

Figure 3.1: MEMS sensor module (without epoxy filling) with accelerometer and gyro sensitive axes shown.

The 1-DOF experiments for the closed-loop position control were performed on a

single-axis hydraulic boom shown in Figure 3.2. A test mass of 500 kg was used on the cylinder side of the boom during the experiments. A lift cylinder with a size of ø80/45-545 mm was controlled with a hydraulic closed-loop proportional valve that had a nominal flow rate of 24 L/min at a nominal pressure of 3.5 MPa (35 bar) per control notch. With a supply pressure of 21 MPa (210 bar), the cylinder produces a maximum force of 100 kN. A PowerPC-based dSpace DS1103 system was used as a real-time control interface to the servo valves and for feedback sampling at a rate of 500 Hz ($T_s = 0.002$ s), which was also the controller output update rate. To allow comparison and verification of the developed MEMS sensor performance, a highly accurate Heidenhain ROD 486 encoder outputting 5000 sine waves per revolution was installed directly on the rotating joint pin to provide a position reference. With each incremental pulse further sub-divided by four in the DS1103, the final encoder position resolution was 0.00018 deg. Therefore, it can be concluded that compared to the MEMS sensor, the Heidenhain encoder provides almost 200 times higher resolution position feedback. Interface to the MEMS sensor module was through the CAN-bus operating at 1 Mbit/s, which was also used to supply the power to the module.

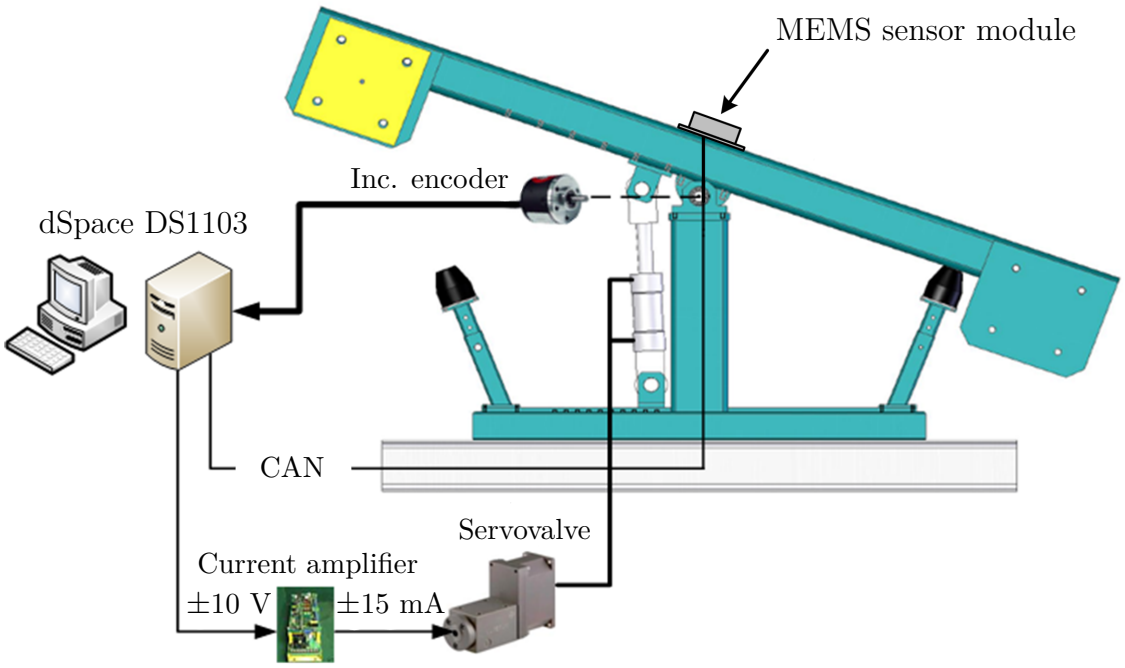

Figure 3.2: Single-axis test bench experimental setup.

The parameters of the experimental system in Figure 3.2 were experimentally identified as $w_n = 28$ rad/s and $\delta_n = 0.05$. The measured open-loop velocity gain K_{qa} was 21 deg/s. These measured values yield a theoretical value for the marginal stability

limit of the proportional feedback gain at $K_p = 0.13$ 1/s. This so-called critical proportional control gain value (see e.g. Dorf and Bishop [25]) was measured to be $K_{cr} = 0.1$ 1/s.

Now, consider supplying the required feedback of the boom position (inclination angle) and its derivatives, namely angular velocity and angular acceleration from the MEMS sensor mounted on the boom as illustrated in Figure 3.2. As the motion of the 1-DOF test bench is restricted to a vertical plane and the boom joint is 1-DOF rotary, the y and z axis outputs of the MEMS accelerometer attached to the boom can be given as a function of the inclination angle θ:

$$\begin{aligned} a^y &\approx |\mathbf{g}_0| \sin(\theta) \\ a^z &\approx |\mathbf{g}_0| \cos(\theta) \end{aligned} \tag{3.1}$$

when the accelerometer is stationary. Algebraic inclination through a 360-degree range relative to gravity vertical can then be calculated by applying

$$\hat{\theta} = \arctan(a^y, a^z), \tag{3.2}$$

where $\arctan(\cdot)$ is the four quadrant inverse tangent function. Note that (3.2) should not be affected by sensitivity changes due to temperature: the y and z direction scale factor non-linearities in the accelerometer output (2.27) should be the same. Although this inclination estimate is valid only when gravity alone acts on the accelerometer, as previously discussed in Section 1.1, mounting the accelerometer close to the joint centre limits the effects of motion accelerations on the inclination estimate. The estimate (3.2) and integrated angular velocity of the gyroscope can now be considered noisy redundant measurements of the same boom inclination. Because the bias in the gyroscope output (2.26) contains mostly low-frequency perturbations, any standalone integration of the angular velocity without high-pass filtering will be susceptible to drift. Additionally, because in this test setup the accelerometer output (2.27) contains mostly high-frequency perturbations, any accelerometer-based inclination estimate should be low-pass filtered. To fuse the accelerometer and gyroscope measurements in real-time, the complementary filter (2.39) is applied in discrete-form as

$$\begin{bmatrix} \hat{\theta}(t) \\ \hat{b}^x(t) \end{bmatrix} = \begin{bmatrix} 1 & T_\mathrm{s} \\ 0 & 1 \end{bmatrix} \begin{bmatrix} \hat{\theta}(t-1) \\ \hat{b}^x(t-1) \end{bmatrix} + \begin{bmatrix} T_\mathrm{s} & 0.5T_\mathrm{s}^2 \\ 0 & T_\mathrm{s} \end{bmatrix} \begin{bmatrix} k_\mathrm{P} \\ k_\mathrm{I} \end{bmatrix} \Big(x_2 - \hat{\theta}(t-1) \Big) + \begin{bmatrix} T_\mathrm{s} \\ 0 \end{bmatrix} x_1, \tag{3.3}$$

where t denotes time, T_s is the sampling time, and $\hat{b}^x$ is the estimated gyro bias. The first input can be given as

$$x_1 = \Omega^x, \tag{3.4}$$

and the second input as

$$x_2 = \hat{\theta}. \tag{3.5}$$

To estimate the gyro bias values in real-time, $k_\mathrm{P} = 0.2$ and $k_\mathrm{I} = 0.02$ were chosen for the proportional and integral gains. This means that (3.3) implements a PI-type complementary filter, in which the inclination estimate (3.2) from the accelerometer is used only as a long-term reference.

The filter operation is illustrated in Figure 3.3. Note that by placing the sensor module close to the joint rotation centre, the linear acceleration components are minimised and the relation (3.2) may be used directly as the input to the low-pass branch of the complementary filter. The small remaining linear acceleration effects contribute to the initial reverse direction dip of the accelerometer branch in Figure 3.3. However, the effect on the overall filter output is negligible. The average steady-state error of the complementary filter output was found to lie typically within ± 0.05 deg.

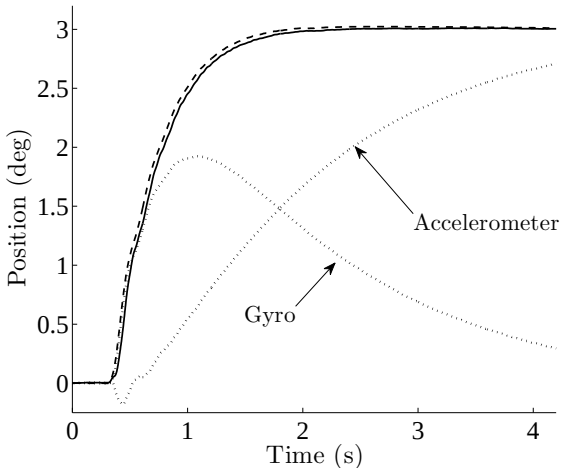

Figure 3.3: Complementary filter branch contributions (dotted lines) and the filter output (solid line) versus true position (dashed line).

Recall that directly differentiated angular acceleration estimate (2.32) is plagued by high-frequency perturbations. To improve its quality, two ideas underlie the

methodology presented below. The first idea is related to exponential weighting of measurements. The second is related to robust quantization and further suppression of higher-frequency noise, which poses a challenge considering the dynamics of the used hydraulic valve. The servovalve used in the experimental setup has a bandwidth of 60 Hz. Thus, the valve spool will react to any feedback signal noise within this bandwidth.

The differentiation of angular velocity is fundamentally of noise-amplifying nature. As the delay properties of the acceleration signal are also critical, it is of interest to use higher weights on recent measurements and lower weights on past ones. One way to relate the weights and measurements is through

$$g_k = \sum_{i=0}^{\infty} \rho_i u_{k-i}, \tag{3.6}$$

where u_k denotes the angular velocity measured at time k. If the weights ρ_i are exponential and given by

$$\rho_i = \gamma(1-\gamma)^i, 0 < \gamma \leq 1, \tag{3.7}$$

it is easy to show that the above weighting function can be rewritten in a recursive manner as (see Roberts [86])

$$g_k = (1-\gamma)g_{k-1} + \gamma\, u(k), \tag{3.8}$$

where $g_0 = \mu_0$ is the initial angular velocity typically set to zero. Now the parameter γ acts as a forgetting factor and the recursion, called geometric moving average (GMA), has weights decreasing as a geometric progression from the most recent point back to the first. As the value of γ decreases, the recursion becomes less sensitive to changes in the input, i.e. its *inertia* increases. The above makes the GMA an infinite impulse response filter, which is tuned for noise suppression at the cost of a small delay. The recursion impulse response is shown in Figure 3.4 for the parameter value of 0.75. It can be deduced that the filter delay is of class one sampling period. Generally, this type of filter has a memory length of $1/(1-\gamma)$. For $\gamma = 0.75$, the four most recent samples contribute significantly to the filter output.

The hydraulic valve dead-zone is a non-linearity that is among the key factors limiting the static and dynamic performance of a closed-loop control system. However, the valve used in the experiments has no dead-zone, but rather a small spool underlap, and as such, even the smallest non-zero values of the angular acceleration signal may make the boom react. A straightforward approach to addressing the problem is to

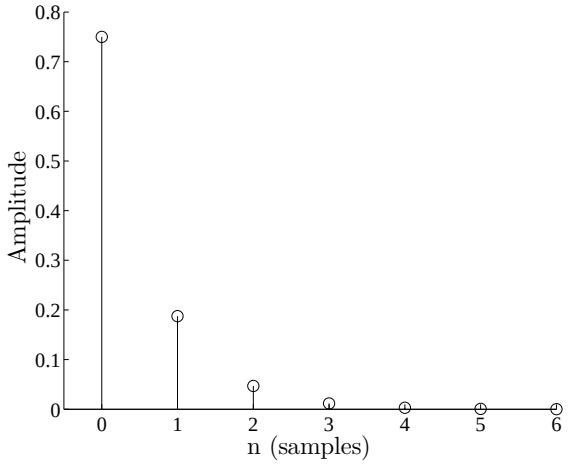

Figure 3.4: Impulse response of the GMA filter for $\gamma = 0.75$.

create an artificial dead-zone by implementing a quantization of close-to-zero values inside the controller. That is, all the GMA-filtered angular velocity values in range of ± 0.12 deg/s were set to zero in real-time. The range is application-dependent and was chosen empirically by monitoring the GMA-filtered signal typical steady-state variation. The result of this operation is shown in graph (b) of Figure 3.5.

Because robustness was desired, a median filter with a window length of seven samples was used for extra smoothing of the final differentiated angular acceleration. The output of the median filter

$$\text{median}\{g_k, \ldots, g_{k-6}\} \tag{3.9}$$

is the middle value after all the samples in the filtering window are sorted numerically. Figure 3.5(d) illustrates the angular acceleration signal after applying the median filter. The introduced non-linear filter effectively cancels small high-frequency zero-centred variation in the angular acceleration feedback and makes the control loop more stable.

The behaviour and performance of the control system was tested initially using stepwise control inputs. A step input is a disturbance to the system that ideally contains all possible excitation frequencies of equal portions according to Fourier analysis theory. While such excitation is impossible in any real physical system, step inputs are useful here for examining the stability and possible oscillatory behaviour of the test bench. The steady-state accuracy of the closed-loop control system can

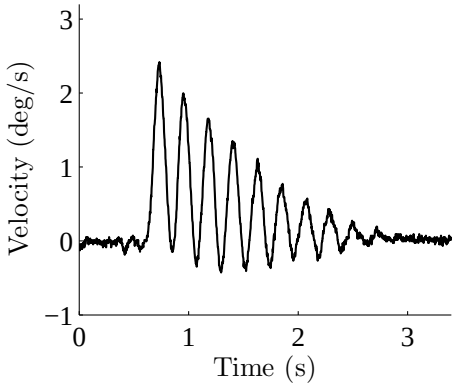

(a) Raw gyro output.

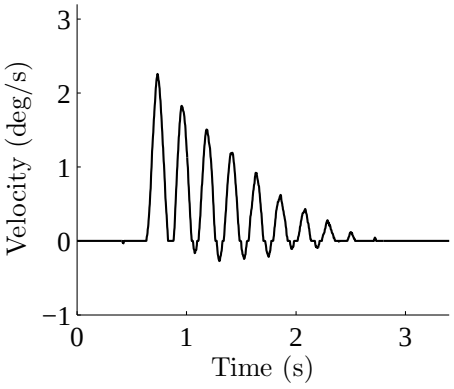

(b) After GMA-filter and dead-zone.

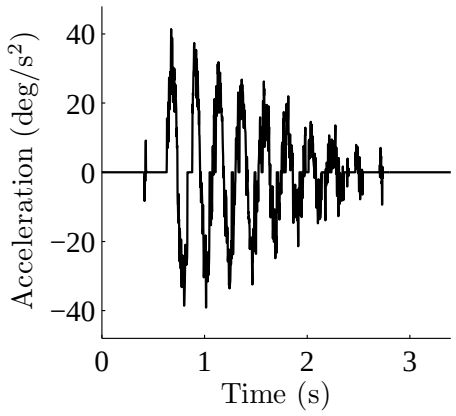

(c) Velocity differentiated into acceleration.

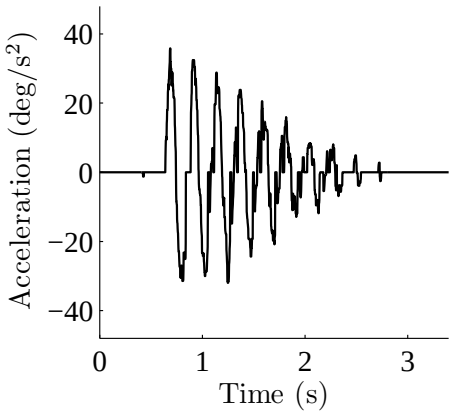

(d) After median filtering.

Figure 3.5: Derivation of angular acceleration from GMA-filtered angular velocity.

also be determined along with its rise time (90% of final value). The step sizes were determined to be in the range from 1 degree to 7 degrees.

The controller presented in Figure 1.3 was used for both proportional and state feedback control. The main aim in the experiments was to shown an increase in the system damping and control the boom oscillations with acceleration feedback, which here acts in the role of active inertia dampening the oscillations; see (1.3) and (1.4). Therefore, velocity feedback was omitted ($K_v = 0$) and only partial state feedback was implemented. When pure proportional position control was used, the acceleration feedback gain K_a was set to zero. The experiments were conducted using both encoder and MEMS sensor feedback. In the case of encoder feedback, the angular velocity was calculated from the encoder position reading with the difference

operator (2.32). The same procedure illustrated in Figure 3.5 was then used for generating the angular acceleration feedback.

Initial experiments on open-loop velocity performance were performed with a valve command input shown in Figure 3.6(a). With no acceleration feedback, the boom velocity exhibits considerable oscillation during the movement, as could be expected. The experimental valve command input profile in Figure 3.6(a) approximates a typical command input of a mobile machine operator in a working situation. That is to say, it is desired to accelerate the hydraulic actuator quickly to the travelling velocity.

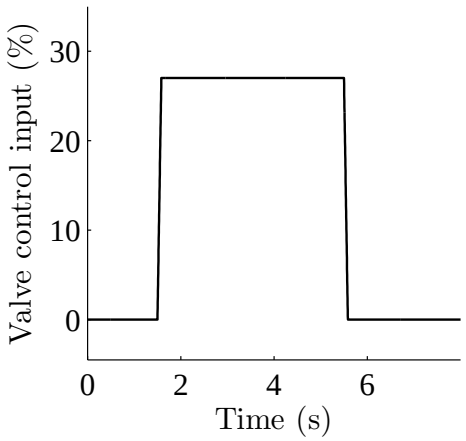

(a) Valve control input without acceleration feedback.

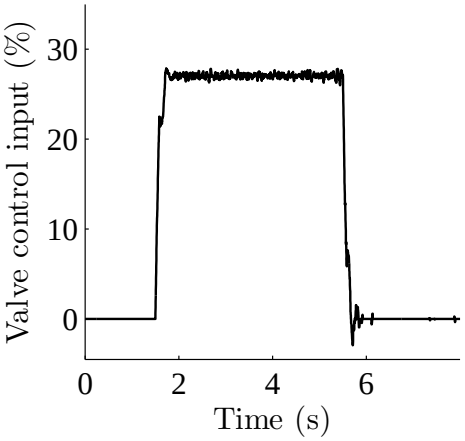

(c) Valve control input with acceleration feedback.

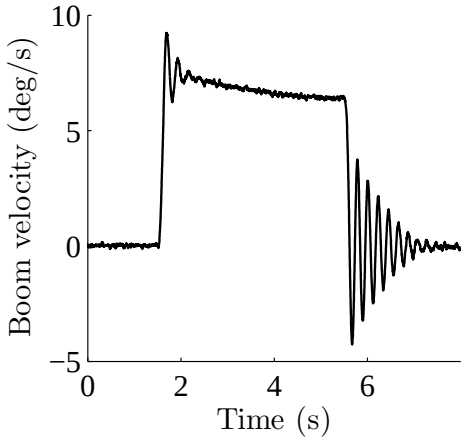

(b) Resulting boom velocity without acceleration feedback.

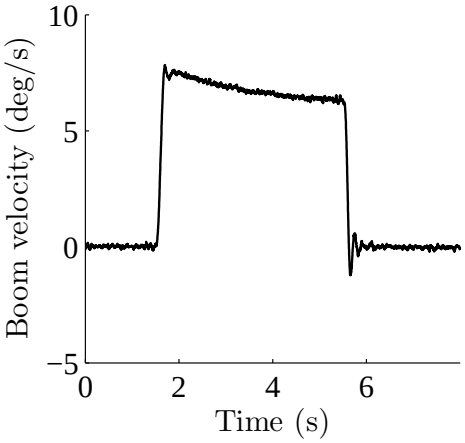

(d) Resulting boom velocity with acceleration feedback.

Figure 3.6: Effect of acceleration feedback on boom velocity.

The resulting notable velocity oscillation of the boom is shown in Figure 3.6(b). The velocity response in Figure 3.6(d) was achieved by including acceleration feedback to the valve control input, which can be observed in the command input shown in Figure 3.6(c). The response was tuned for maximum damping of velocity oscillations while keeping the acceleration feedback gain within stability limits. In this case, the acceleration feedback gain was $K_a = 0.0008$. As it can be seen from Figure 3.6(d), the use of acceleration feedback yields a substantial reduction of velocity oscillation especially during the deceleration phase of the movement.

The following figures present the results of closed-loop position control experiments, in which the feedback source was changed between the encoder and the MEMS module between experiments. For illustration purposes, the measured position values in all the figures are taken from the high-accuracy incremental encoder. Figure 3.7 shows the results for two different size step inputs when the proportional controller gain was $K_p = 0.05$, which is half of the measured critical gain K_{cr}. As can be seen, the overall dynamic performance with the two different feedback sources is quite similar. The 90% rise time is approximately 2.1 seconds for the 1-degree and 2.3 seconds for the 5-degree step.

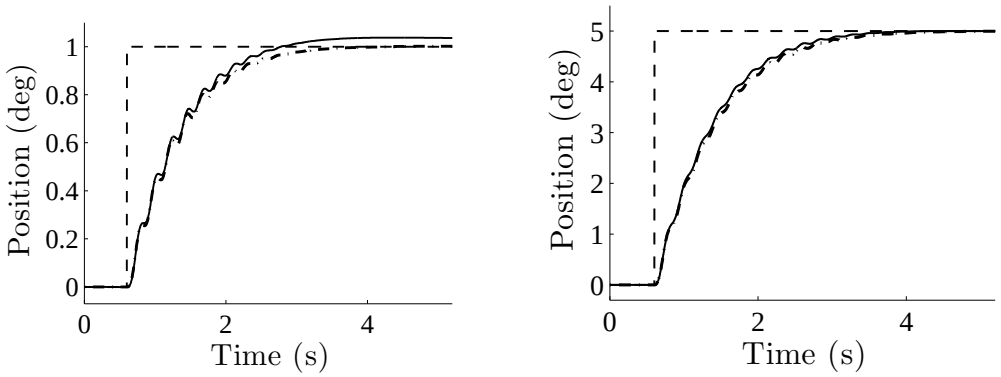

(a) 1 degree step; $K_p = 0.05$, $K_a = 0$. **(b)** 5 degree step; $K_p = 0.05$, $K_a = 0$.

Figure 3.7: P-control step responses using encoder feedback (dash-dot) and MEMS-feedback (solid line).

In state feedback control, the angular acceleration feedback gain K_a increases the damping of the closed-loop system. This allows the use of higher values for the proportional gain K_p, leading to more accurate and faster response time without overshooting, as can be seen from Figure 3.8. For the state feedback experiments, the proportional gain K_p was raised to the value of K_{cr}. A suitable value for K_a was found to be 0.00045. Values higher than this started causing instability in the control-loop as the boom behaviour became too sensitive to random variations in the filtered angular acceleration signal. The 90% rise times are approximately 1.5

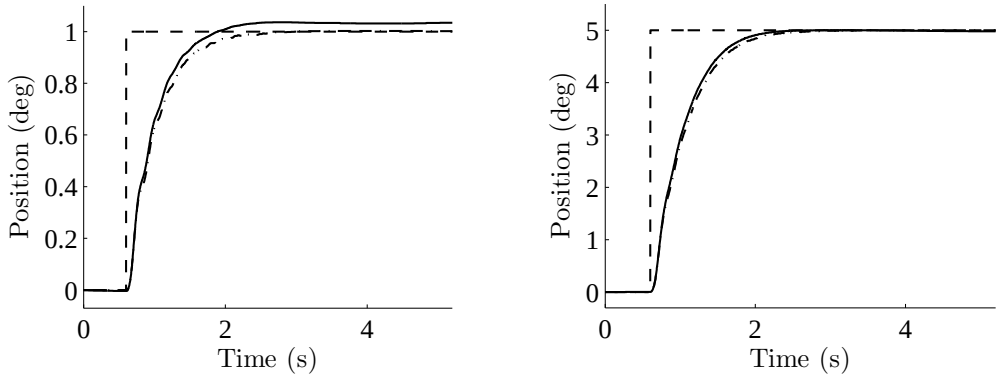

(a) 1-degree step; $K_p = 0.10$, $K_a = 0.00045$.

(b) 5-degree step; $K_p = 0.10$, $K_a = 0.00045$.

Figure 3.8: State feedback control step responses using encoder feedback (dash-dot) and MEMS-feedback (solid line).

seconds for the 1-degree step and 1.6 seconds for the 5-degree case. This is an average decrease of some 32% in the rise time, if compared with the case in Figure 3.7.

The steady-state position control errors of all test cases are summarised in Table 3.1. The error values for each step size are average values of five measurements, from which a further overall mean value is calculated. The steady-state error is defined as the difference between the position set point value and true position from encoder. As it is seen, for both feedback cases the state feedback control produces a smaller error. Recalling that the encoder has a resolution of 0.00018 degrees and it operates as a reference, the maximum errors in the table with the encoder feedback source may be considered as an approximation of the error induced by the control loop. These errors are ±0.006 deg and ±0.004 deg in the proportional (P-control) and state feedback control cases, respectively.

As previously discussed in Section 1.3, the complementary filter alone is sufficient for the inclination estimation of the boom in this experiment, as the placement of

Table 3.1: Steady-state positioning repeatability (±deg) for the indicated position step sizes and the overall mean error per control case.

Step size	1 deg	3 deg	5 deg	7 deg	mean
P-control, MEMS	0.035	0.15	0.02	0.06	0.066
P-control, encoder	0.002	0.005	0.005	0.006	0.005
State fb. control, MEMS	0.05	0.01	0.03	0.06	0.038
State fb. control, encoder	0.002	0.002	0.003	0.004	0.003

the MEMS sensor close to the joint centre keeps the transient linear accelerations low, and the perturbations are mostly caused by vibration. Hence, one can deduce that the measured MEMS steady-state positioning error, of class ±0.06 deg in both control cases, is almost solely due to the complementary filtering average steady-state error of class ±0.05 deg, which is affected by, for example, linearity and sensitivity errors of the accelerometer.

To conclude, the implemented MEMS-based state feedback control of the boom yielded an increase in damping and a corresponding improvement in positioning performance; the rise time decreased 32%, and the steady-state positioning error was on average 42% smaller compared to proportional position control. The state feedback control positioning repeatability was on average about 0.04 deg with a worst-case value of ±0.06 deg. The results also showed that despite the MEMS sensor's inherent disadvantage in accuracy, linearity, noise characteristics, and an almost 200-fold coarser angular resolution, the motion control results with the high-accuracy encoders are improved only by approximately a factor of 10. This means that the achievable motion control results are primarily limited only to the MEMS sensor output linearity and noise specifications.

3.2 Multi-body motion sensing

In order to rigorously test and verify the proposed MEMS-based motion state estimation model for multi-body systems, a mechanically simple vertical planar three-link test bench was constructed. With a small-scale test bench, which behaves like an ideal rigid multi-body assembly, the MEMS components can easily be subjected to motions which are close to their saturation limits, and the performance of the motion estimation model can be evaluated under varying conditions. Although the MEMS components allow 2-DOF inclination sensing based on the force of gravity, the planar vertical case is of theoretical and practical interest as previously discussed in Section 1.5. The experimental results published in the co-authored publications Vihonen et al. [78][1] and [79][2] are summarised in the following.

The mechanically simple vertically mounted three-link planar arm is shown in Figure 3.9. The first two joints are actuated with 70 W graphite brush DC-motors,

[1] In [78], Equation (19) should read $x_1 = \tilde{\Omega}^x$

[2] In [79], Table II second column should read

	Eq. (18)*		
	Joint 1	Joint 2	Joint 3
	2.00	5.41	5.89
	0.46	1.12	0.90

which are controlled by two dedicated digital EPOS 24/5 motor controllers. Coupled with planetary gear heads, each motor-gear assembly produces an output torque of about 20 Nm, which is transmitted via toothed belts to the first two joints of the arm. The third joint was moved freely.

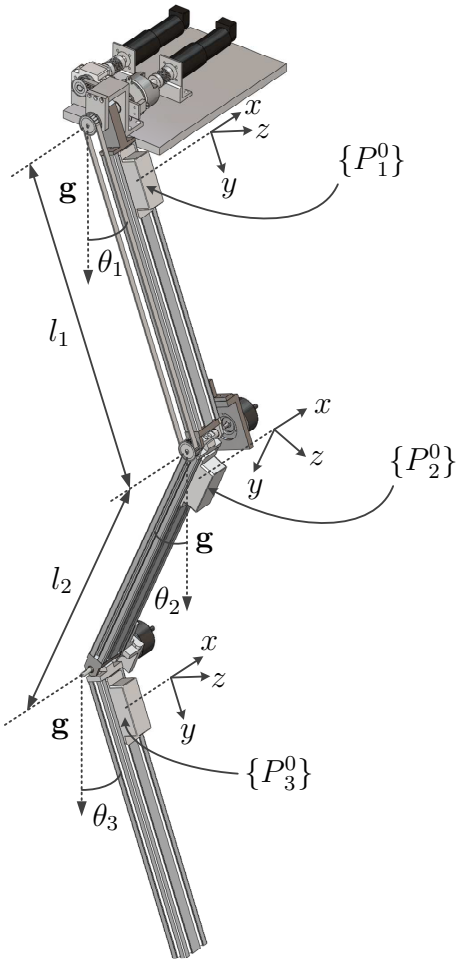

Figure 3.9: Mechanical three-link planar arm comparable to a rigid multi-body assembly. The MEMS sensor modules are located at ${}^1\mathbf{r}_{P_1^0} = [0\ 0.14\ 0.03]^{\mathrm{T}}$ m, ${}^2\mathbf{r}_{P_2^0} = [0\ 0.10\ 0.03]^{\mathrm{T}}$ m, and ${}^3\mathbf{r}_{P_3^0} = [0\ 0.13\ 0.03]^{\mathrm{T}}$ m. The link lengths are $l_1 = l_2 = 0.47$ m. Body frames $\{B_i\}$ are omitted for clarity.

Similarly to the experimental setup in Section 3.1, the dSpace DS1103 real-time platform was used for the motor control and motion state estimation at a rate of 500 Hz. The reference sensor for the first joint was a SICK DGS66 hollow-shaft encoder [87], outputting 10 000 pulses per revolution. Similar Heidenhain ROD 486

encoders used in the single-body experiments were installed on the second and third joints. Thus, the final encoder position resolutions were 0.009 deg for the SICK encoder and 0.00018 deg for the Heidenhain encoders.

In contrast to the single-body experiments of Section 3.1, the MEMS sensors on the second and third links are now subject to significant acceleration components during motion. To obtain smoothed low-delay estimates of the link rotations by using complementary filtering, estimated linear accelerations are removed from the accelerometer readings before filtering. That is to say, the complementary filter (2.39) may be directly generalised in discrete form as

$$\begin{bmatrix} \hat{\theta}_i(t) \\ \hat{b}_i^x(t) \end{bmatrix} = \begin{bmatrix} 1 & T_\mathrm{s} \\ 0 & 1 \end{bmatrix} \begin{bmatrix} \hat{\theta}_i(t-1) \\ \hat{b}_i^x(t-1) \end{bmatrix} + \begin{bmatrix} T_\mathrm{s} & 0.5T_\mathrm{s}^2 \\ 0 & T_\mathrm{s} \end{bmatrix} \begin{bmatrix} k_\mathrm{P} \\ k_\mathrm{I} \end{bmatrix} \Big(x_2 - \hat{\theta}_i(t-1) \Big) + \begin{bmatrix} T_\mathrm{s} \\ 0 \end{bmatrix} x_1. \quad (3.10)$$

The first input is given by

$$x_1 = {}^i\Omega_i^x \quad (3.11)$$

and the second input by

$$x_2 = \arctan({}^i a_i^y - {}^i\hat{v}^y_{P_i^0}, {}^i a_i^z - {}^i\hat{v}^z_{P_i^0}). \quad (3.12)$$

The motion compensation in (3.12) is required to prevent significant error accumulation in the gyroscope bias estimate. In other words, to ensure proper operation of the filter (3.10), it is necessary that the filter inputs represent redundant measurements of the same rotation. As the motion is planar, the rotation matrices R_i can be efficiently updated by writing

$$R_i \approx \hat{R}_i(\hat{\theta}_i) = \begin{bmatrix} 1 & 0 & 0 \\ 0 & \cos(\hat{\theta}_i) & -\sin(\hat{\theta}_i) \\ 0 & \sin(\hat{\theta}_i) & \cos(\hat{\theta}_i) \end{bmatrix}. \quad (3.13)$$

The algebraic representation of rotation is useful here because, though all the link inclination estimates (3.2), (3.12), and (3.10) are computed in different ways, any one of them may be written as

$$\hat{\theta}_i = \theta_i + b + \mu. \quad (3.14)$$

Here, b contains mostly low-frequency perturbations, such as accelerometers bias values; μ contains mostly high-frequency perturbations, such as component thermal noise; and θ_i is the true position of the ith link.

The three MEMS-based link inclination estimates using the standard method (3.2), motion compensation (3.12), and complementary filtering (3.10) were compared experimentally. The experiment consisted of a period of sinusoidal swaying motion mainly generated by the first joint and of a period of random joint motion in the range of ± 100 deg/s at most. To later demonstrate the difference between off-the-shelf and calibrated MEMS components, a calibration procedure was also carried out, in which the planar arm was used as a turn table to cover the inclination bias values that could not be expressed as a pure rotation, i.e. by determining the scale factor matrix and the bias values of the model (2.27). Calibration look-up tables for the MEMS accelerometer runtime bias compensation were implemented using a 3-degree grid with linear interpolation for in-between values. To identify experimental averages for the gyroscope scale factors, the planar arm was also used as a rate table providing an angular velocity reference from differentiated encoder readings. As a result, the MEMS rate gyroscopes located at $\{P_1^0\}$, $\{P_2^0\}$, and $\{P_3^0\}$ utilised 1.15%, 0.70%, and 0.85% x-axis calibration scale factors in (2.26), respectively.

Figure 3.10 illustrates the experimental results with reference link inclination angles θ_i on the left-hand side, and the differences of the inclination estimates with respect to the encoders on the right, which were calculated as

$$\Delta\theta_i = \theta_i - \hat{\theta}_i, \ i = 1, 2, 3. \tag{3.15}$$

Table 3.2 provides a comparison of the results between the standard (3.2) and the motion compensated (3.12) estimates in terms of the peak absolute error (PAE) and the root-mean-square error (RMSE). As can be expected, the standard estimate produces large errors, which increase link by link as the distances between the MEMS accelerometer and rotation axles generating the motion become larger. Conversely, the motion compensated generalisation (3.12) is mostly dominated by zero-centred high-frequency perturbations, which are amplified in a similar cascade manner. The difference with respect to the standard estimate is most clearly seen on the third link, for which the motion compensated estimate (3.12) yields a 64% smaller RMSE value.

A comparison of the complementary filtered inclination estimate (3.10) with and without calibration is given in Table 3.3. As previously discussed, this approach is in principle only susceptible to inclination-dependent accelerometer bias values and motion-dependent scale factor non-linearities. The calibration effectively targets these low-frequency components as shown. Composite input-output non-linearities, such as

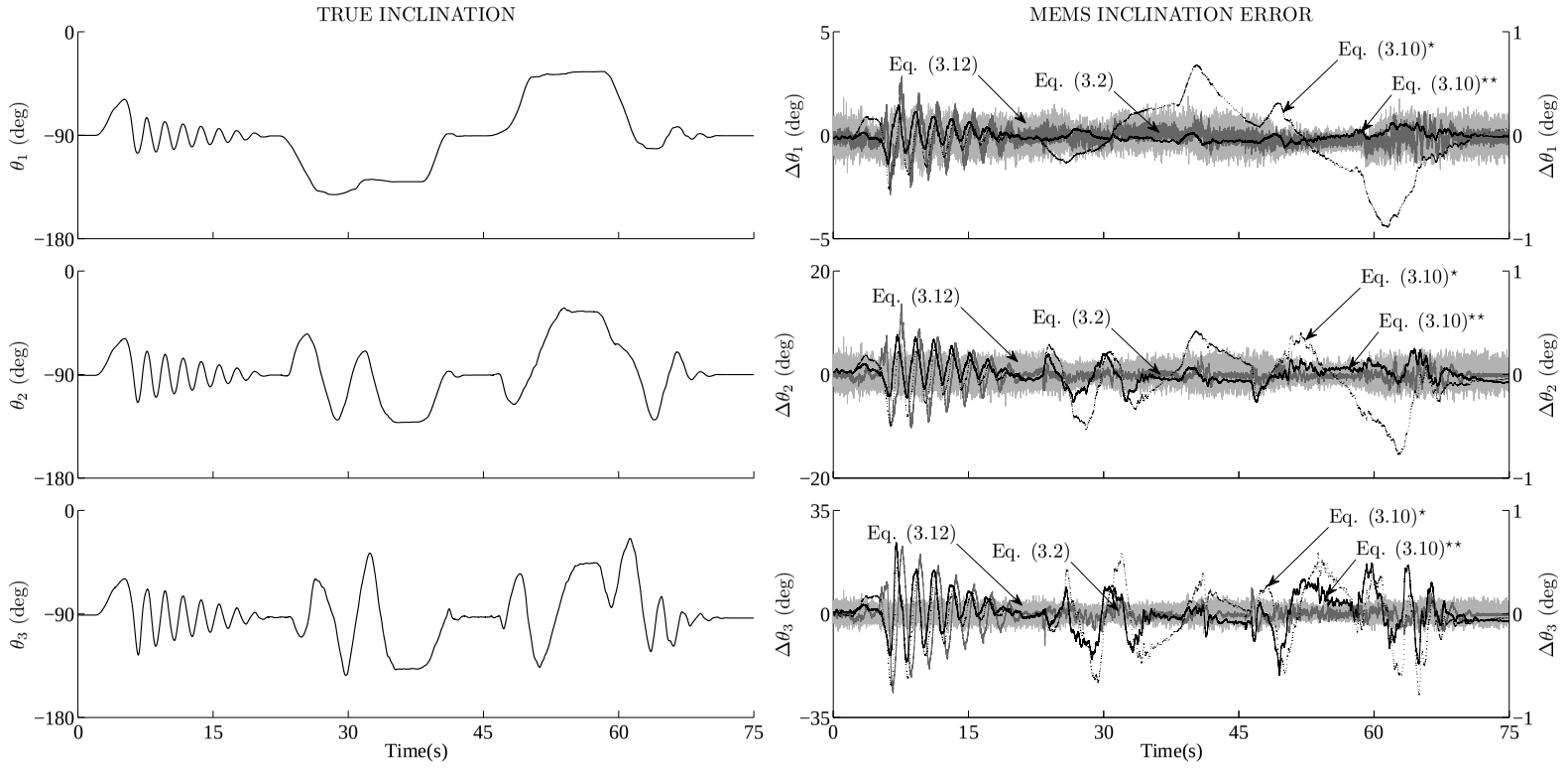

Figure 3.10: A comparison of the different link inclination sensing methods. Note the scales of the error graphs: the standard estimate (3.2) as well as its motion compensated equivalent (3.12) use the y axis on the left and the two PI-type complementary filters (3.10) use the y axis on the right. The superscripts * and ** distinguish between the off-the-shelf MEMS and the calibrated cases, respectively. See Table 3.2 and 3.3 for more detailed values.

the total sensitivity and hysteresis rated for the gyroscope (2.26) and accelerometer (2.27) by the MEMS manufacturer, play a role at high angular rates from ±60 to ±100 deg/s. Nonetheless, the complementary filter (3.10) yields a further 5−15-fold reduction in the peak and root-mean-square estimation errors compared to (3.12) when calibrated components are used.

Table 3.2: Link position estimate errors using standard (3.2) and motion compensated (3.12) inclination estimates.

	Eq. (3.2)		Eq. (3.12)	
	PAE (deg)	RMSE (deg)	PAE (deg)	RMSE (deg)
Link 1	2.89	0.49	2.00	0.46
Link 2	13.61	2.19	7.23	1.47
Link 3	26.71	4.88	10.93	1.76

Table 3.3: Complementary filtered link position estimate errors using off-the-shelf (3.10)* and calibrated (3.10)** MEMS components.

	Eq. (3.10)*		Eq. (3.10)**	
	PAE (deg)	RMSE (deg)	PAE (deg)	RMSE (deg)
Link 1	0.89	0.29	0.29	0.06
Link 2	0.78	0.23	0.39	0.10
Link 3	0.78	0.25	0.69	0.18

Under the assumption that the links of the assembly behave as rigid bodies, estimates of the joint positions are given by

$$\hat{\phi}_i = \hat{\theta}_i - \hat{\theta}_{i-1},\ i = 1, 2, 3, \tag{3.16}$$

where the base frame rotation around the x axis is simply included by using the horizontal position as the reference, i.e. $\hat{\theta}_0 = 0$ deg. Figure 3.11 illustrates the resulting joint position errors $\Delta\phi_i$, which were obtained from the encoder reference joint positions ϕ_i as

$$\Delta\phi_i = \phi_i - \hat{\phi}_i,\ i = 1, 2, 3. \tag{3.17}$$

By comparing the cases in Figures 3.10 and 3.11, it can be seen that common-mode errors of the link inclinations are largely removed by the application of (3.16). Tables 3.4 and 3.5 provide a summary of the joint sensing errors shown in Figure 3.11.

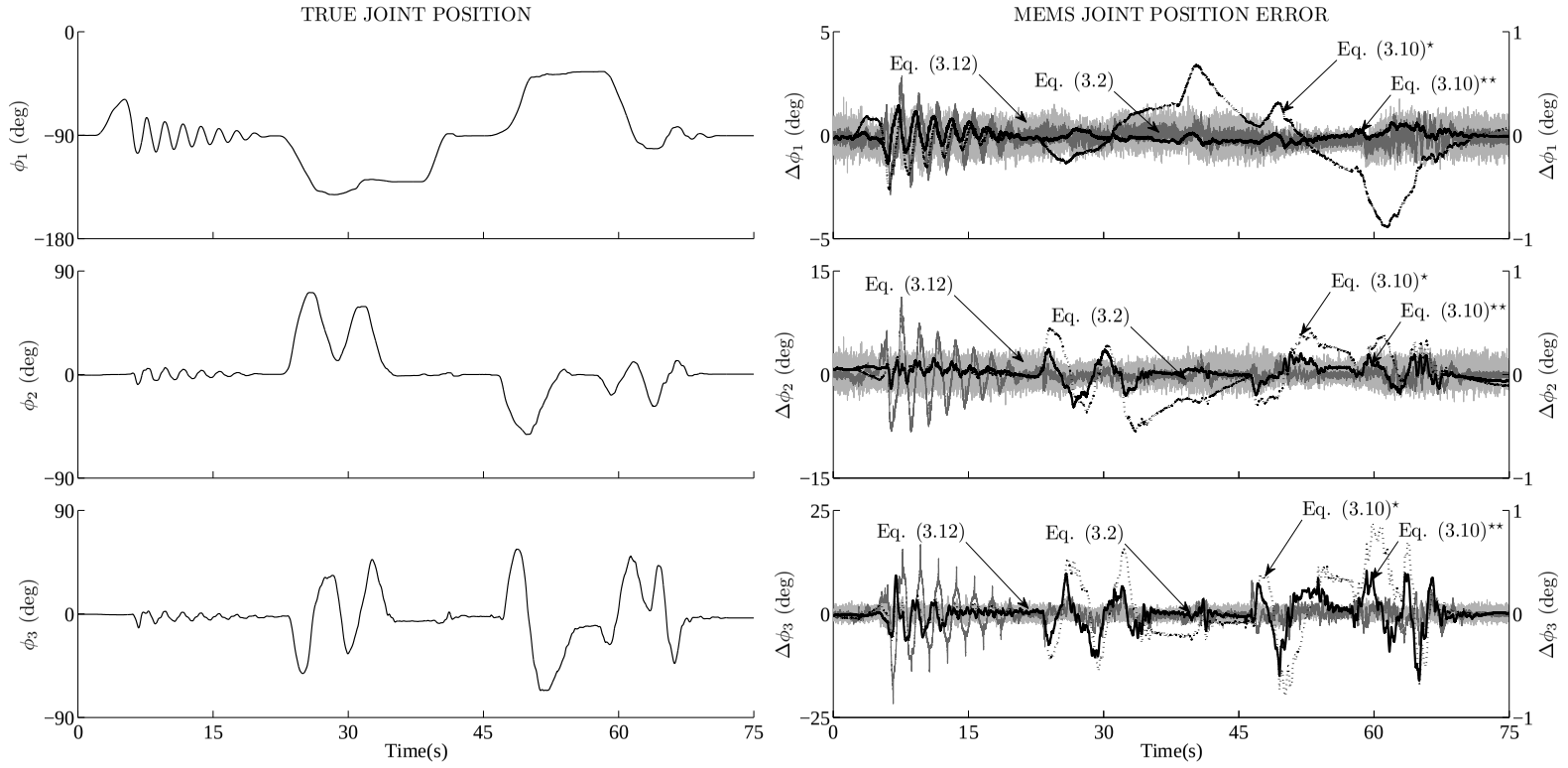

Figure 3.11: Joint position errors derived from the link inclinations. In the complementary filter cases using off-the-shelf (3.10)* and calibrated (3.10)** MEMS components, sensitivity residues of high rates from ± 60 to ± 100 deg/s and inclination-dependent accelerometer bias values in the off-the-shelf case reach notable levels. See Table 3.4 and 3.5 for more details.

Here the improvement by using the motion compensated estimate (3.12) is again clear. However, the complementary filtered inclinations based on (3.10) are in a league of their own. In view of (3.14), at least three factors guarantee their 10 – 20-fold superiority: i) high-frequency perturbations in the algebraic inclination (3.12) are attenuated by the embedded low-pass filter; ii) the gyroscope bias in (2.26) is removed by the complementary high-pass filter; and iii) any high-frequency perturbation in the angular rate (2.31), such as vibration of the test bench, is attenuated by the integrator in the filter architecture forward path (see Figure 2.7).

Table 3.4: Joint position estimate errors using standard (3.2) and motion compensated (3.12) inclination estimates.

	Eq. (3.2)		Eq. (3.12)	
	PAE (deg)	RMSE (deg)	PAE (deg)	RMSE (deg)
Joint 1	2.89	0.49	2.00	0.46
Joint 2	11.19	1.77	5.41	1.12
Joint 3	21.69	3.04	5.89	0.90

Table 3.5: Complementary filtered joint position estimate errors using off-the-shelf (3.10)* and calibrated (3.10)** MEMS components.

	Eq. (3.10)*		Eq. (3.10)**	
	PAE (deg)	RMSE (deg)	PAE (deg)	RMSE (deg)
Joint 1	0.89	0.29	0.29	0.06
Joint 2	0.55	0.20	0.32	0.09
Joint 3	0.87	0.27	0.65	0.14

The frequency response of the joint position estimate was also identified, as it is an important characteristic regarding the applicability of the proposed estimation approach to a closed-loop control system. Figure 3.12 illustrates the amplitude and phase responses in sinusoidal 1-DOF motion for the complementary filtered inclination estimate. Only the MEMS at $\{P_1^0\}$ was used for simplicity. The frequency f was increased in a linear fashion from 0.1 to 3.3 Hz so that the mechanical arm was inclined from the gravity vertical by approximately ± 2 deg; i.e., $A = \frac{2\pi}{180}$ and $\theta_0 = -\frac{\pi}{2}$. The motion of the first joint can be characterised by

$$\theta_1 = A\sin(2\pi f t) + \theta_0 \tag{3.18}$$

$$\dot{\theta}_1 = A\,2\pi f\cos(2\pi f t) \tag{3.19}$$

$$\ddot{\theta}_1 = -A(2\pi f)^2\sin(2\pi f t). \tag{3.20}$$

While the quadratic nature of (3.20) and MEMS scale factor errors might explain the build-up of marginal non-linearities at higher frequencies, the inclination gain is close to unity with only a 2−3 sample delay at most. About 1 ms of the delay comes from the MEMS electronics data acquisition cycle time at a 500 Hz sampling rate. The response demonstrates that the complementary filtered estimates (3.10) of the true rotation are stable and well described when associated with fast time-scales.

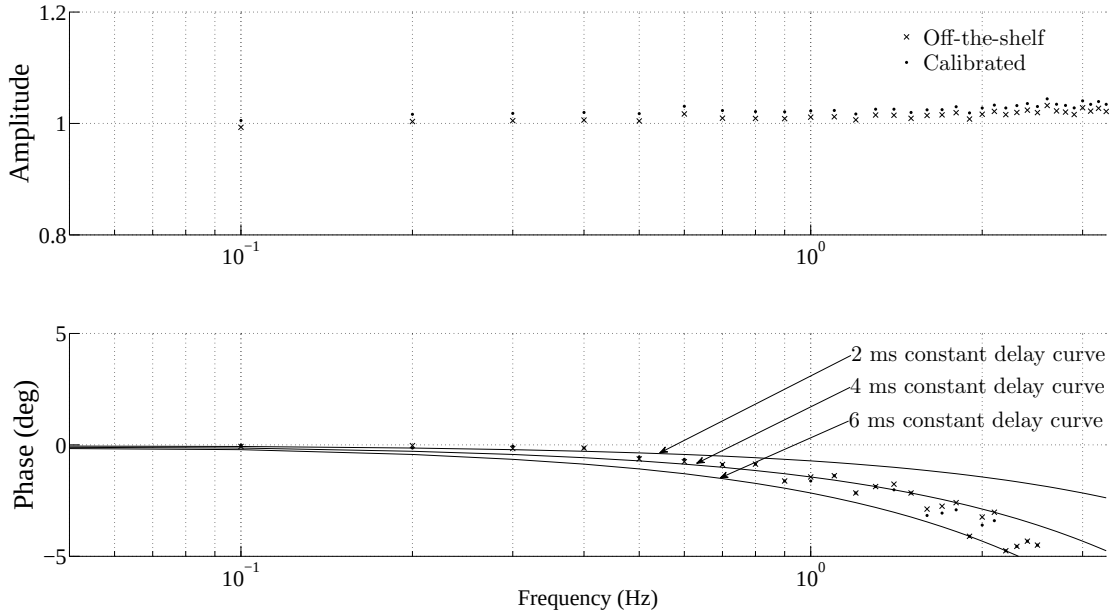

Figure 3.12: Frequency response of the complementary filter (3.10) in sinusoidal motion at 500 Hz sampling rate. The frequency of motion ranges from 0.1 to 3.3 Hz. The low delay response above without unwanted distortion is an important property from the control perspective.

Next, in order to experimentally verify the proposed angular acceleration direct algebraic solution (2.24), the same experimental setup of Figure 3.9 was used with three additional MEMS sensors installed on the links of the planar arm as shown in Figure 3.13. As the motion is vertically planar, the extra accelerometers at $\{P_i^2\}$ in the configuration of Figure 2.6 can be omitted. For ease of comparison, the experiment consisted of similar sinusoidal and random motions as illustrated on the left-hand side of Figure 3.10.

The angular acceleration needed for the linear acceleration estimate (2.33) was now computed using two MEMS sensors per link. For briefness, the performance was evaluated by only examining the resulting joint position estimate (3.16). Because the standard inclination estimate (3.2) yields identical results, only the motion compensated (3.12) and complementary filtered (3.10) inclination estimates are

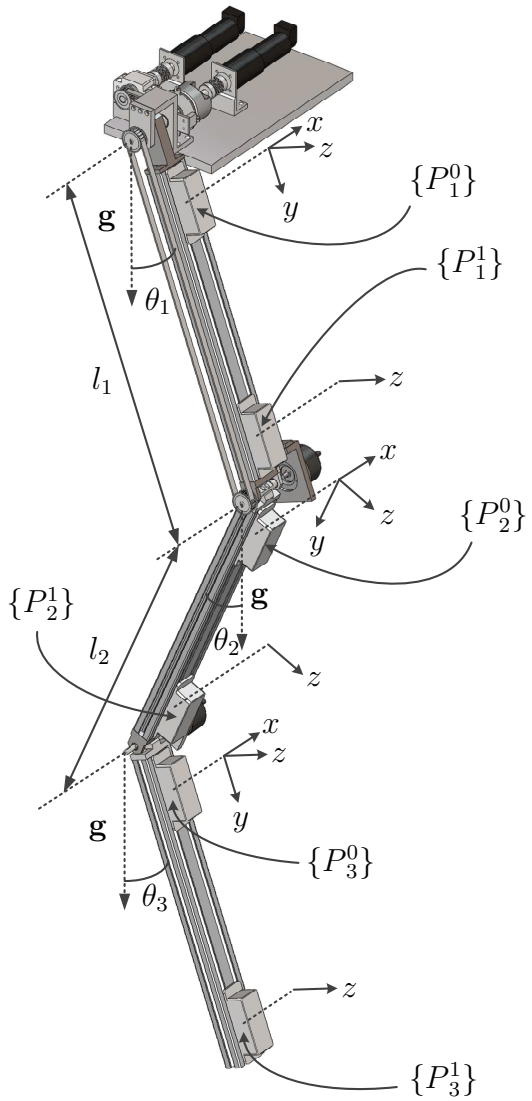

Figure 3.13: Three-link planar arm with two MEMS sensors per link. The MEMS sensor positions are ${}^1\mathbf{r}_{P_1^0} = [0\ 0.14\ 0.03]^{\mathrm{T}}$ m, ${}^1\mathbf{r}_{P_1^1} = [0\ 0.44\ 0.03]^{\mathrm{T}}$ m, ${}^2\mathbf{r}_{P_2^0} = [0\ 0.10\ 0.03]^{\mathrm{T}}$ m, ${}^2\mathbf{r}_{P_2^1} = [0\ 0.45\ 0.03]^{\mathrm{T}}$ m, ${}^3\mathbf{r}_{P_3^0} = [0\ 0.13\ 0.03]^{\mathrm{T}}$ m, and ${}^3\mathbf{r}_{P_3^1} = [0\ 0.45\ 0.03]^{\mathrm{T}}$ m. The link lengths are $l_1 = l_2 = 0.47$ m. Body frames $\{B_i\}$ are omitted for clarity.

examined. For visual reference, Figure 3.14 compares the performance to the configuration of Figure 3.9 with Table 3.6 summarising the key metrics. As illustrated in Figure 3.14, the reduction of the motion compensated estimate error is notable. If compared with the results in Table 3.4, the alternative direct angular acceleration

sensing reduces the peak and root-mean-square errors of the motion compensated estimate (3.12) on average by a factor of 2.5. The complementary filter performs almost identically in comparison with the values in Table 3.5 as expected, as the filter is in principle only susceptible to inclination-dependant accelerometer bias values and motion-dependent scale factor non-linearities.

Next, the bias-corrected angular velocity estimate (2.31) was compared to an optimal zero-bias differentiation designed for real-time control applications (see Harrison and Stoten [37]). An optimal estimate of the first-order derivative of joint i position estimate (3.16) with respect to time t is given by

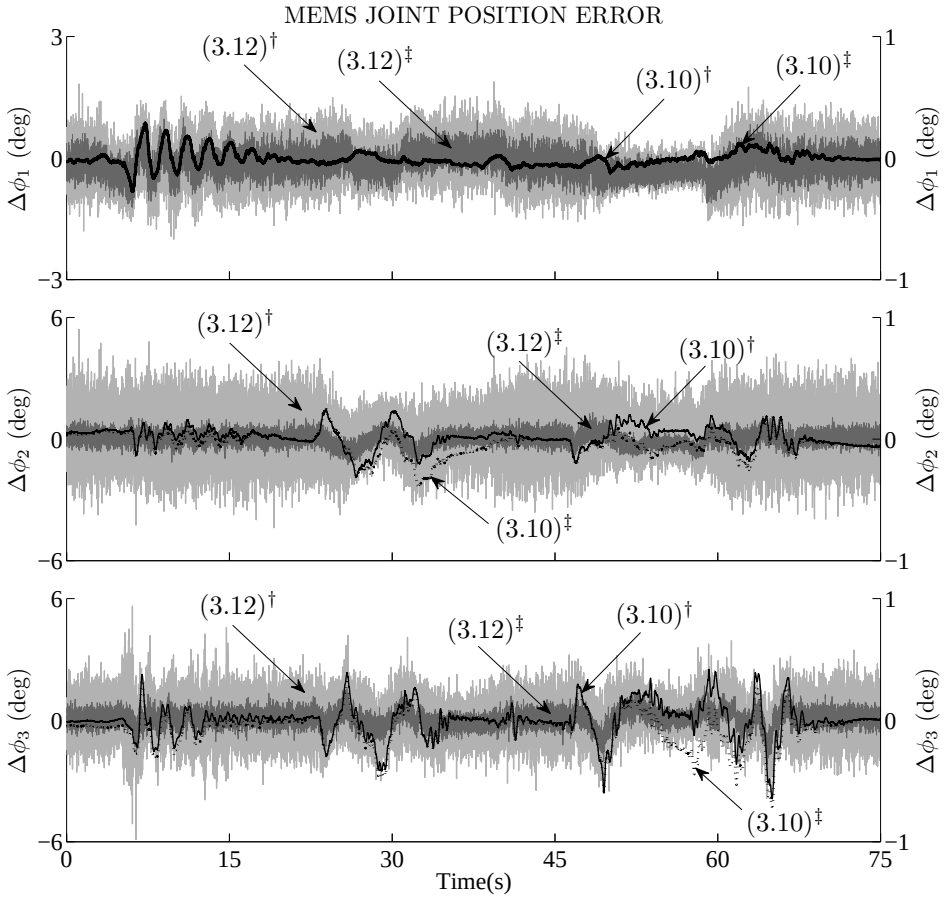

Figure 3.14: A comparison of joint position sensing configurations. Note that the motion compensated estimates (3.12) use the y axis on the left, and the two PI-type complementary filters (3.10) use the y axis on the right. The superscripts † and ‡ distinguish between the MEMS configurations illustrated in Figure 3.9 and Figure 3.13, respectively.

Table 3.6: Joint sensing errors using two MEMS per link. Estimation errors of the motion compensated (3.12) and complementary filtered position estimates (3.10) are given.

	Eq. (3.12)		Eq. (3.10)	
	PAE (deg)	RMSE (deg)	PAE (deg)	RMSE (deg)
Joint 1	1.21	0.30	0.29	0.06
Joint 2	1.40	0.32	0.39	0.10
Joint 3	2.16	0.40	0.74	0.16

$$\dot{\phi}_i(t) \approx \frac{1}{T_s} \sum_{k=0}^{n-1} A(k)\, \hat{\phi}_i(t - k\,T_s), \tag{3.21}$$

where the weights are $A = [5\ 3\ 1\ -1\ -3\ -5]/35$. Similarly, for a comparison with the directly differentiated angular acceleration (2.32) and the algebraic estimate (2.35), an optimal estimate of the joint i angular acceleration $\ddot{\phi}_i$ is obtained by applying a second-order difference operation to the joint position given by

$$\ddot{\phi}_i \approx \frac{1}{T_s} \sum_{k=0}^{n-1} B(k)\, \hat{\dot{\phi}}_i(t - k\,T_s) \approx \frac{1}{T_s^2} \sum_{k=0}^{n-1} C(k)\, \hat{\phi}_i(t - k\,T_s), \tag{3.22}$$

where the coefficients are: $B = [5\ 3\ 1\ -1\ -3\ -5]/35$ and $C = [5\ -1\ -4\ -4\ -1\ 5]/28$.

The complementary filtered high-bandwidth positions based on (3.10) were differentiated in the above optimum manner for a comparison. For a visual reference, a set of three estimates of the third joint angular acceleration is shown in Figure 3.15. A more detailed comparison is made in Tables 3.7 and 3.8. Because errors arise with the encoder references at high sampling rates from noise and quantization effects of derivatives, making accurate reference joint angular accelerations unobtainable, the tabulated values are calculated at standstill. The reported lags are indicative, but if the tabulated 1 ms delay of the MEMS electronics cycle time is excluded, the directly sensed MEMS motion derivatives (2.31) and (2.24) are lag-free. If a further reference is made with the optimum derivatives in Table 3.8, the results of the direct angular acceleration sensing (2.24) are clearly the best, and in excellent agreement with the primary theoretical finding (2.37), particularly if recalling the limited dimensions of the planar arm.

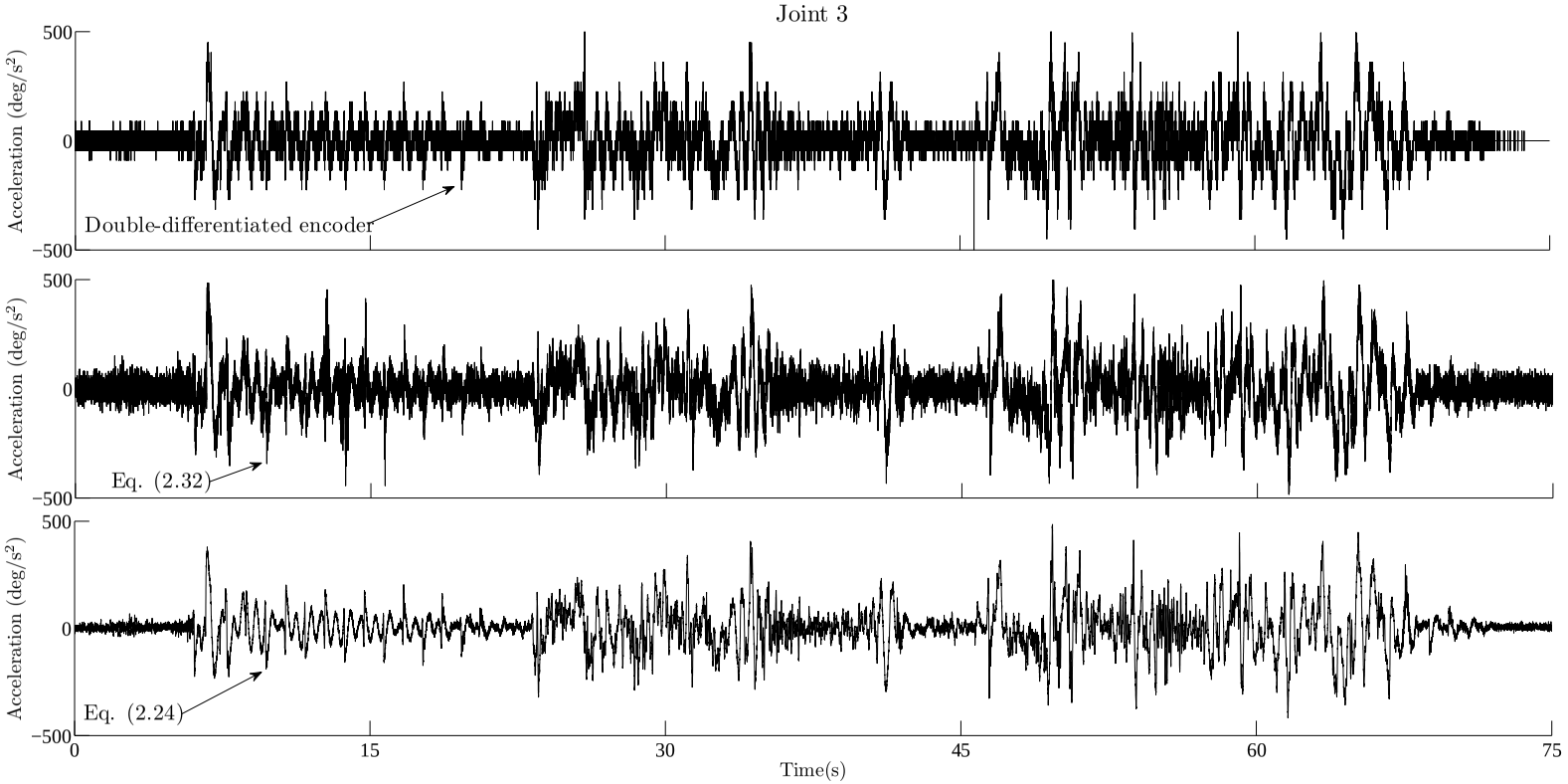

Figure 3.15: A plot illustrating double-differentiated encoder position, differentiated MEMS rate gyro (2.32), and MEMS accelerometer-based direct sensing (2.24) of angular acceleration. Whereas the encoder benchmark has a low noise density only at a perfect standstill, resolution of the proposed direct angular acceleration sensing (2.24) remains fine at low rates throughout the experiment.

Table 3.7: Standstill joint angular velocity errors of bias-corrected gyro (2.31) and optimal differential of position (3.21).

	RMSE (deg/s)	
	Eq. (2.31)	Eq. (3.21)
Joint 1	0.068	0.062
Joint 2	0.081	0.072
Joint 3	0.078	0.073
Lag (ms)	1	5–6

Table 3.8: Standstill joint angular acceleration errors of directly differentiated gyro (2.32), optimally differentiated position estimate (3.16) & (3.22), optimally differentiated gyro (2.31) & (3.22), and directly sensed angular acceleration (2.24).

	RMSE (deg/s^2)			
	Eq. (2.32)	Eqs. (3.16) & (3.22)	Eqs. (2.31) & (3.22)	Eq. (2.24)
Joint 1	31.38	13.57	8.64	6.78
Joint 2	35.74	15.78	10.25	8.74
Joint 3	33.50	16.05	9.86	8.38
Lag (ms)	2–3	5–6	5–6	1

Summary of multi-body motion sensing

Based on the experimental results, one may conclude that the proposed observation model captures the full motion state of the planar arm, making the geometry-aided link inclination sensing well defined during accelerative motions. However, as shown by the errors of the motion compensated estimate (3.12) in Figures 3.10 and 3.11, driving the motion disturbance effects close to a zero-mean random process amplifies high-frequency perturbations. In this respect, because of the complementary principle, the PI-type complementary filter (3.10) is very successful in high-bandwidth joint position reconstruction while keeping assumptions to a minimum. When considering the target application field of heavy-duty hydraulic manipulators having natural frequencies below 2 Hz, the complementary filter exceeded the required dynamics by producing close to ideal inclination responses up to some 3.3 Hz as shown in Figure 3.12. Although the MEMS may not be able to achieve the accuracy of encoder-type angular sensors, with orders of magnitude higher resolutions, the joint angle sensing with less than ± 1 deg worst-case position error in real-time is well comparable with previously published works, including the 10 – 20-fold improvements achieved

with the complementary filter, as detailed in Tables 3.2 – 3.5. Even though the choice between a gyro-aided 1-DOF and 3-DOF complementary filter is application-dependent, the typical similarity of a 3-DOF architecture (see Mahony et al. [61]) to that of the complementary filter (3.10) makes the theoretical result (2.34) of gravity-referenced inclination sensing broadly applicable.

Motivated by the fact that a low-cost angular acceleration sensor with good resolution for low angular rates is not available at present, the multi-sensor configuration of Figure 2.6 was applied to the direct sensing of the joint angular accelerations. In the 1-DOF experimental cases, only one additional accelerometer per link was required, if compared with the configuration Figure 2.5. Direct comparison to angular acceleration derived from an encoder position was found infeasible due to the large amount of superimposed noise and quantization effects in the reference acceleration. However, the benefit of the directly sensed angular acceleration estimate is clearly seen in the motion compensated inclination estimate (3.12), in which the errors were reduced by a factor of 2.5. In other words, this means that the angular acceleration estimated with the multi-sensor configuration is closer to the actual link acceleration than a differentiated angular velocity reading. This improvement is not as pronounced in the resulting complementary filtered joint position estimate, because the low-pass filter embedded in the complementary filter is very successful in removing the high-frequency perturbations from the motion compensated inclination estimate (3.12). As we shall see next, a high-quality angular acceleration estimate is however of critical importance for a closed-loop motion control system, in which acceleration feedback is required.

3.3 Multi-body motion control

As shown in the previous sections, the MEMS-based motion state estimation performs well with multiple rigid bodies as well as in the closed-loop control of a single-body system. What remains is to experimentally verify that the proposed motion state estimation can be used to supply feedback of joint positions, velocities, and accelerations in a multi-body manipulator motion control system. The following two sections summarise the experimental results for two motion control application examples, which were originally published in Honkakorpi et al. [76, 77].

3.3.1 Suspended load anti-sway control system

In this experiment a suspended load anti-sway control system is realised using the MEMS sensors for the manipulator motion state, suspended load inclination angle, and angular velocity estimation. The anti-sway control concept uses a semi-active approach, in which the desired load velocity is set by the manipulator operator via e.g. joystick input, and the underlying load oscillation damping control system creates the required manipulator end-effector velocity.

The motion control experiments were performed on a HIAB 031 hydraulic manipulator, which was installed on a rigid base. Figure 3.16 illustrates the MEMS configuration attached on the links of the manipulator as well as on the suspended load. The swinging load consisted of a rigid 13 kg arm, 1.7 m in length with a 50 kg load mass mounted on the tip. The fluid flow to the lift and tilt cylinders, both ø80/45-545 mm in size, were controlled by directly operated NG10-size servo solenoid valves. The nominal flow rates of the valves controlling the lift and tilt cylinders were 100 l/min ($\Delta p = 3.5$ MPa per control notch). The bandwidth of the valves was 100 Hz for a $\pm 5\%$ control input. The hydraulic power supply was set to 19.0 MPa supply pressure. To enable comparison with previous experiments, the same dSpace DS1103 real-time platform was used for controlling the valves. The Heidenhain ROD 486 encoders were used as the joint reference sensors. The reference angular velocities of the manipulator joints and of the suspended load were estimated with the optimal difference operator (3.21). Note that if the load is suspended from a cable and swinging in 3D, the sensing system can be modified in a manner described by Ouyang et al. [88] to sense the two dimensions of the cable swing with a more complex mechanical assembly. As given in (2.34), the MEMS-based inclination sensing is suitable for the estimation of two-dimensional cable swinging motion.

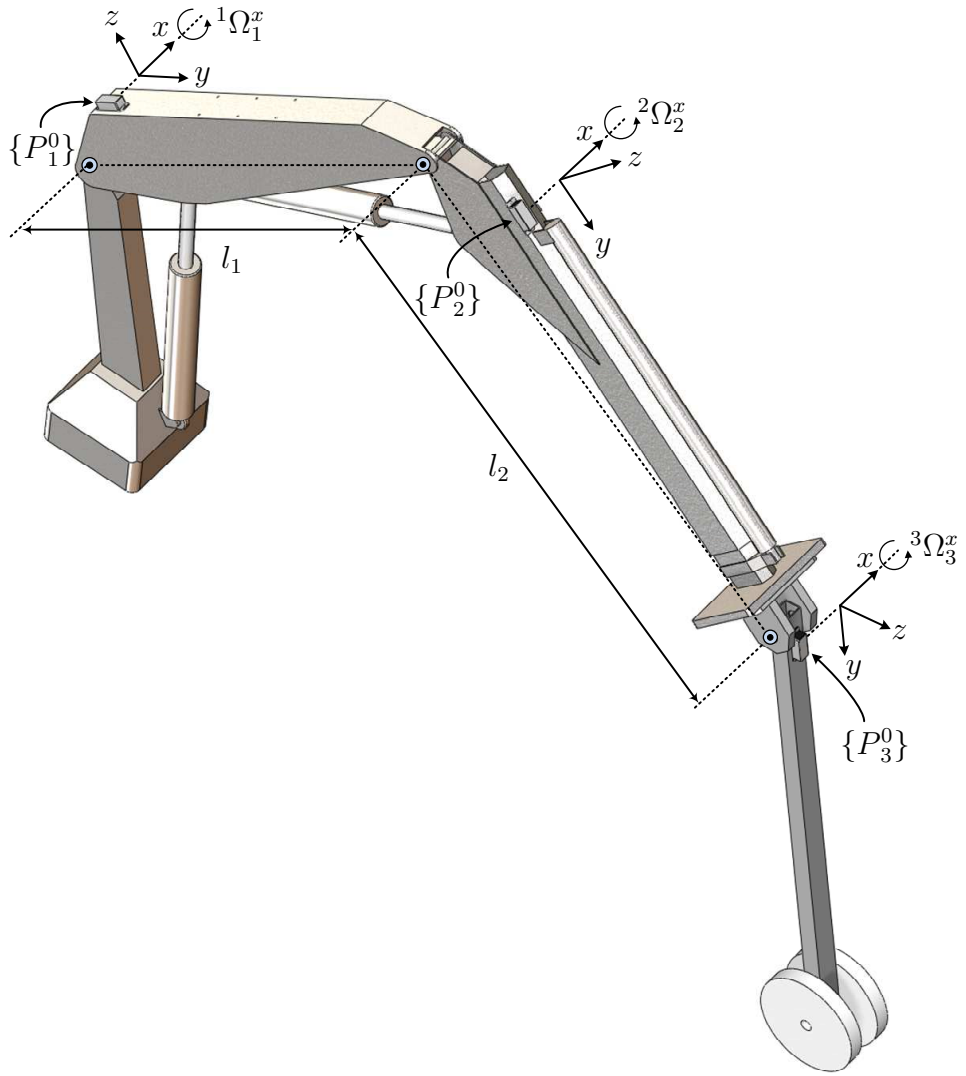

Figure 3.16: MEMS-sensor configuration on the hydraulic manipulator. The MEMS sensor positions are ${}^1\mathbf{r}_{P_1^0} = [0\ 0.21\ 0.23]^{\mathrm{T}}$ m, ${}^2\mathbf{r}_{P_2^0} = [0\ 0.24\ 0.22]^{\mathrm{T}}$ m, and ${}^3\mathbf{r}_{P_3^0} = [0\ 0.19\ 0.045]^{\mathrm{T}}$ m. The link lengths are $l_1 = 1.60$ m and $l_2 = 1.65$ m. Body frames $\{B_i\}$ are omitted for clarity.

Now, consider the kinematics representation of the hydraulic manipulator in Figure 3.17. The positions of the two actuated revolute joints are denoted by q_1 and q_2. A third prismatic joint is available, but it is unused, which sets the manipulator into non-redundant operation mode. The fourth revolute joint with the suspended load is unactuated. Examining the physical dimensions of the manipulator structure yields a fixed relationship between the manipulator angles $\theta_i, i = 1, 2$ and the actuated joint angles q_i as $\theta_i = q_i + \beta_i$, $\beta_i = [\,-56.43^\circ\ -155.25^\circ\,]$ (see Beiner and Mattila [89]).

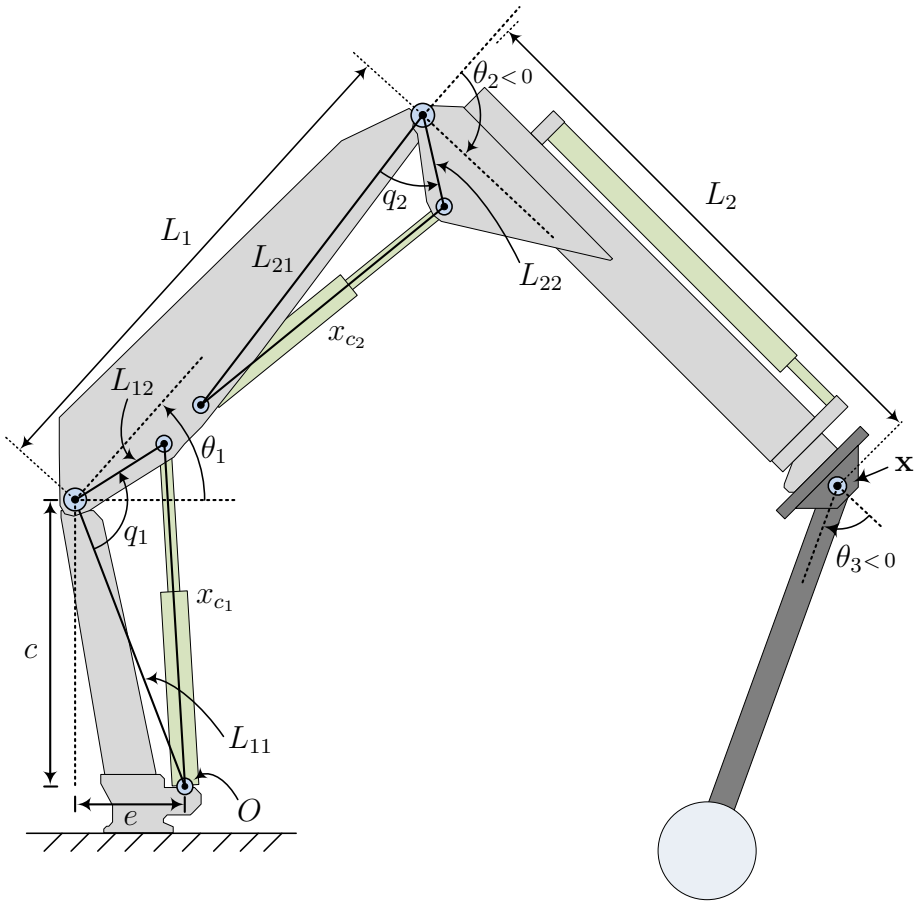

Figure 3.17: HIAB 031 manipulator kinematics.

The forward kinematics relating the manipulator joint variables $\mathbf{q} = [\, q_1 \; q_2 \,]^{\mathrm{T}}$ to the end effector position $\mathbf{x} = [\, x \; y \,]^{\mathrm{T}}$ are obtained as

$$x = L_1 \cos(q_1 + \beta_1) + L_2 \cos(q_1 + q_2 + \beta_1 + \beta_2) - e \tag{3.23}$$
$$y = L_1 \sin(q_1 + \beta_1) + L_2 \sin(q_1 + q_2 + \beta_1 + \beta_2) + c, \tag{3.24}$$

where $L_1 = 1.6$ m, $L_2 = 1.82$ m, $c = 0.96$ m, and $e = 0.23$ m. Expressed in a more compact form, the forward kinematics simplify to

$$\mathbf{x} = h(\mathbf{q}). \tag{3.25}$$

The widely known differential kinematics equation relating the manipulator joint velocities $\dot{\mathbf{q}}$ to the resulting end effector linear velocities $\dot{\mathbf{x}}$ is

$$\dot{\mathbf{x}} = J(\mathbf{q})\dot{\mathbf{q}}, \tag{3.26}$$

where the Jacobian matrix is

$$J(\mathbf{q}) = \frac{\partial h(\mathbf{q})}{\partial \mathbf{q}}. \tag{3.27}$$

Given a desired end-effector velocity $\dot{\mathbf{x}}^{ref}$, the required joint velocities $\dot{\mathbf{q}}^{ref}$ are conversely given by

$$\dot{\mathbf{q}}^{ref} = J^{-1}(\mathbf{q})\,\dot{\mathbf{x}}^{ref}, \tag{3.28}$$

as the manipulator in question is non-redundant and the Jacobian matrix **J** is square and directly invertible. To translate the required joint space motion into movement of the hydraulic cylinders in actuator space, the following transformation from joint angle to hydraulic cylinder position is applied:

$$\mathbf{x_c} = C(\mathbf{q}) \tag{3.29}$$

by defining

$$C(\mathbf{q}) = \begin{bmatrix} c_1 & 0 \\ 0 & c_2 \end{bmatrix}, \tag{3.30}$$

where c_i is a function of the joint angles

$$c_i(q) = \sqrt{L_{i1}^2 + L_{i2}^2 - 2L_{i1}L_{i2}\cos(q_i)} \tag{3.31}$$

and $L_{11} = 1.0$ m, $L_{12} = 0.38$ m, $L_{21} = 1.13$ m and $L_{22} = 0.31$ m.

Applying well-known rigid body motion dynamics, a non-linear description of the suspended load dynamics may be formulated. From the control perspective, it is however desirable to form a linearised model of the system under control. The state variable description of the suspended load system is defined as

$$\mathbf{x}_{SL} = [\, x_1 \; x_2 \; x_3 \; x_4 \,]^{\mathrm{T}} = [\, x_{cm} \; \dot{x}_{cm} \; \phi \; \dot{\phi} \,]^{\mathrm{T}}, \tag{3.32}$$

where x_{cm} denotes the horizontal position of the centre of mass, $\dot{x}_{cm}$ denotes its velocity, ϕ denotes the suspended load angle between gravity vertical, and $\dot{\phi}$ its

angular velocity. By using the small-angle approximation $\sin\phi \approx \phi$ and $\cos\phi \approx 1$, and restricting the motion of the manipulator end-effector to the horizontal direction, the motion state of the suspended load can be represented in state space form as (see Honkakorpi et al. [76] for details)

$$\begin{cases} \dot{x}_1 = x_2 \\ \dot{x}_2 = u + L_{cm}\,\ddot{\phi}_3 = u - \dfrac{m_P g L_{cm}^2}{I_{\mathbf{x}}} x_3 - \dfrac{L_{cm} b}{I_{\mathbf{x}}} x_4 - \dfrac{m_P L_{cm}^2}{I_{\mathbf{x}}} u \\ \dot{x}_3 = x_4 \\ \dot{x}_4 = -\dfrac{m_P g L_{cm}}{I_{\mathbf{x}}} x_3 - \dfrac{b}{I_{\mathbf{x}}} x_4 - \dfrac{m_P L_{cm}}{I_{\mathbf{x}}} u, \end{cases} \tag{3.33}$$

where L_{cm} denotes the distance between the load suspension point and its centre of mass, , m_P is the total mass of the suspended load assembly$b$ is a coefficient representing joint friction, $I_{\mathbf{x}}$ is the mass moment of inertia of the load respective to point $\mathbf{x}$, and the system input u is the horizontal acceleration of the manipulator end-effector $\ddot{x}$. In a more compact matrix form, the system dynamics are

$$\dot{\mathbf{x}}_{SL}(t) = A\mathbf{x}_{SL}(t) + B\mathbf{u}_{SL}(t), \tag{3.34}$$

where

$$A = \begin{bmatrix} 0 & 1 & 0 & 0 \\ 0 & 0 & -\frac{m_P g L_{cm}^2}{I_{\mathbf{x}}} & -\frac{L_{cm} b}{I_{\mathbf{x}}} \\ 0 & 0 & 0 & 1 \\ 0 & 0 & -\frac{m_P g L_{cm}}{I_{\mathbf{x}}} & -\frac{b}{I_{\mathbf{x}}} \end{bmatrix} \tag{3.35}$$

$$B = \begin{bmatrix} 0 & 1 - \frac{m_P L_{cm}^2}{I_{\mathbf{x}}} & 0 & -\frac{m_P L_{cm}}{I_{\mathbf{x}}} \end{bmatrix}^{\mathrm{T}} \tag{3.36}$$

and $\mathbf{u}_{SL} = u = \ddot{x}$.

The objective of the combined control system is to drive the suspended load mass to the position desired by the human operator without excessive oscillations. The underlying Cartesian velocity controller drives the manipulator end-effector at a required reference velocity, which in turn is generated by the load anti-sway controller based on the human operator inputs.

The structure of the Cartesian velocity controller is presented in Figure 3.18. The controller reference input is the desired Cartesian velocity $\dot{\mathbf{x}}^{ref}$, which is multiplied with the Jacobian inverse J^{-1} of the measured joint positions $\mathbf{q}$. The result is the

desired joint velocity vector $\dot{\mathbf{q}}^{ref}$. The desired joint velocities are integrated to give desired joint positions and transformed through $C(\mathbf{q})$ to desired cylinder positions $\mathbf{x_c}^{ref}$ giving the input to the cylinder position controller detailed below.

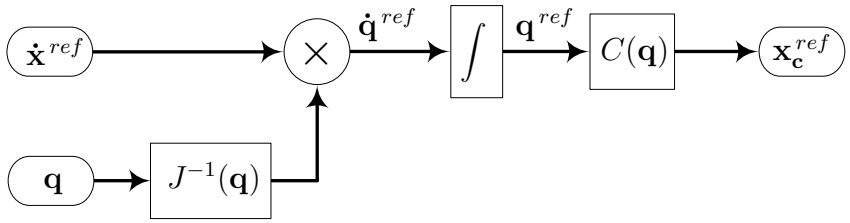

Figure 3.18: Manipulator end-effector Cartesian velocity controller.

The structure of the cylinder position controller is shown in Figure 3.19. The feedforward branch contains an experimentally identified look-up table based mapping F from desired cylinder velocity $\dot{\mathbf{x}}_\mathbf{c}^{ref}$ to required valve control output $\mathbf{u}_v$. The table values are obtained as averages from various manipulator postures, which induce variable loading levels on the cylinders. The use of the feedforward branch improves the dynamic response of the position controller and lessens the effects of plant non-linearities. The closed-loop feedback section uses a filtered proportional position control to correct for any remaining cylinder position error. The time constant τ was chosen as $\tau = 2/\omega_n$ (see Linjama [90]), where $\omega_n \approx 28.3$ rad/s is the lowest natural frequency of the manipulator around the operating point of the experiments. A suitably chosen time constant prevents undesirable high-frequency excitations of the manipulator without excessively sacrificing the control bandwidth.

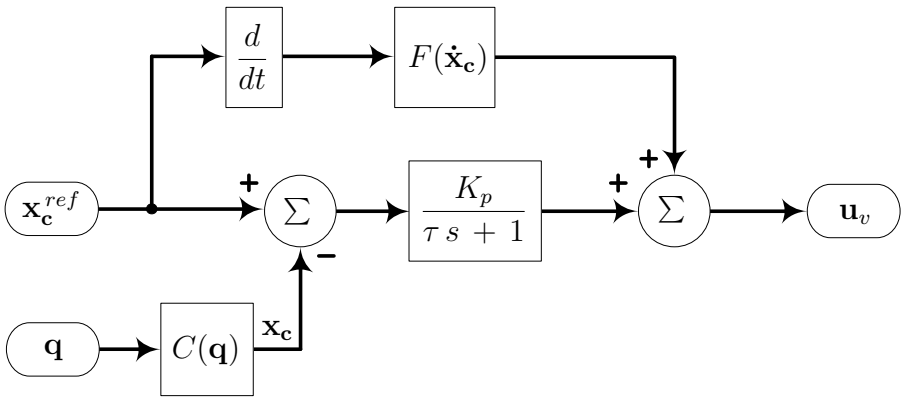

Figure 3.19: Cylinder position controller.

With the suspended load dynamics represented in state-space form, a state feedback controller can now be designed, which can be used to drive the system to a desired state. The state feedback controller gains can be derived using direct pole placement,

from position control settling time requirements or by using common criteria (e.g. ITAE) based on various error measurements between the desired and plant system model response. As the objective of the anti-sway controller is to stabilise the load while simultaneously driving the centre of mass to a desired position, the state feedback controller gain solution given by the linear quadratic regulator (LQR) is a natural choice in this situation. By introducing a position reference input for the centre of mass x_{cm}, the LQR controller aims to quadratically minimise the deviation of the load position from the reference, while driving the other states $\dot{x}_{cm}$ ϕ $\dot{\phi}$ to zero. The use of the weighting matrices R for the control input and Q for the state deviations keeps the expended control effort limited while allowing for the tuning of the closed-loop control stiffness. Solving the associated Riccati equation results in a full state feedback tracking controller with a control law in the typical form:

$$u = -K\mathbf{x}_{SL} + r = -K\mathbf{x}_{SL} + \bar{N}x_{cm}^{ref}, \tag{3.37}$$

where x_{cm}^{ref} is the reference position for the load centre of mass and the scalar $\bar{N}$ is chosen such that $K\mathbf{x}_{SL}$ equals r in steady state. To combine the anti-sway controller to the Cartesian velocity controller, the acceleration output from (3.37) is integrated over time to give the desired Cartesian velocity as illustrated in Figure 3.20. The resulting reference velocity is then given as the reference input for the velocity controller in Figure 3.18.

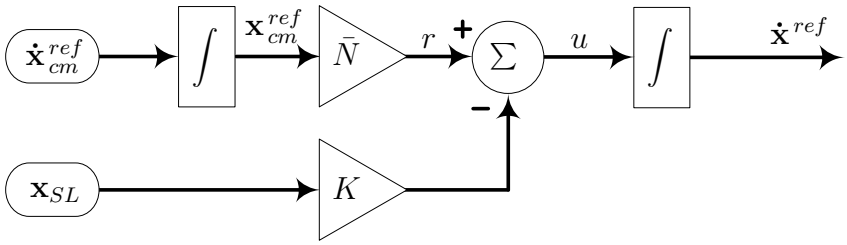

Figure 3.20: Suspended load Cartesian position controller with anti-sway control.

The Cartesian motion control experiments consisted of horizontal motion between two coordinate points. To enable repeatable experiments, the user-supplied Cartesian reference velocities were generated using a second-order polynomial. Figure 3.21 illustrates the resulting uncontrolled swinging of the load when the Cartesian velocity reference for the manipulator end-effector is directly the user input, i.e. $\dot{\mathbf{x}}^{ref} = \dot{\mathbf{x}}_{cm}^{ref}$. With no sway compensation active, the manipulator end-effector follows the user input reference, and the uncontrolled position of x_{cm} (dashed line) overshoots the reference position x_{cm}^{ref} (gray line) by 60%, followed by a slowly decaying oscillation back to equilibrium.

The positioning performance using the anti-sway controller with encoder feedback is represented by the solid black line in Figure 3.21 and correspondingly by the dash-dot line when using MEMS feedback. The two feedback sources yield almost identical control performance. The positioning response has an overshoot of only 6% and a settling time of approximately 3 seconds, which clearly demonstrates the effectiveness of the proposed control concept.

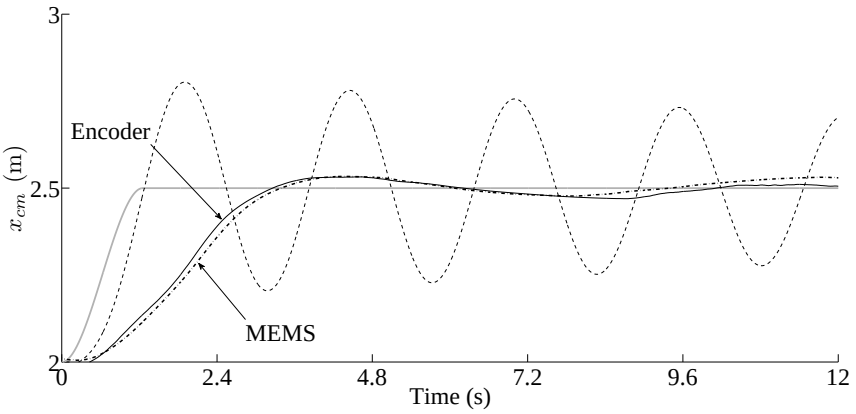

Figure 3.21: Suspended load centre of mass position without control (dashed line) and with load sway compensation using encoder and MEMS feedback.

As is evident from Figure 3.21, the price paid in oscillation damping is the increased settling time. To enable a fair comparison of the anti-sway controller performance, the Cartesian movement was also executed without load sway compensation with a transition time of 3 seconds. The resulting motion of the load centre of mass is illustrated in Figure 3.22 with the previously shown responses of the state feedback controller included for comparison. Even with a slower transition time, the uncontrolled position of the suspended load overshoots by 12% and exhibits oscillatory behaviour.

In general, state feedback control is a very effective approach for stabilising a control system and realising a rapid dynamic response with increased damping, provided that the linearised system model is accurate and the state feedbacks are close to ideal. By giving higher weights in the matrix Q for the states, the closed-loop response can be shaped as desired. In practice, however, the gains of the LQR controller cannot be set as high as would be desirable due to various error sources present in the actual system as well as in the state feedback signals. For the experiments presented above, the diagonal elements of Q were set to $Q_{i,i} = [5\ 6\ \ 0.1\ 0.1]$, which yielded the feedback gain vector $K = [\,7.07\ 11.05\ \ -33.2\ \ -9.4\,]$. Higher values in K quickly resulted in an unstable system despite being well within numerical stability limits. The major contributing sources limiting the anti-sway controller performance are

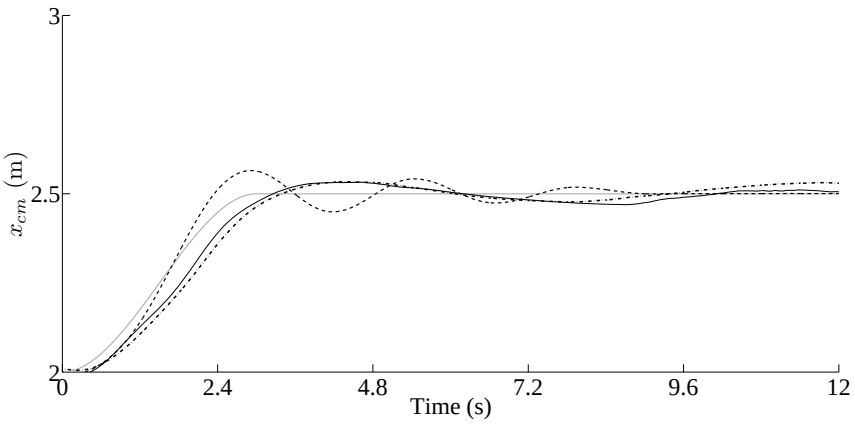

Figure 3.22: Uncontrolled response with 3-second ramp versus controlled response.

the non-linear friction effects in the joint of the suspended load, the non-ideal state feedback signals, and the errors in the manipulator end-effector Cartesian velocity controller.

To summarise, with the MEMS network providing full motion state feedback from the manipulator joints as well as the suspended load sway angle and angular velocity, the suspended load could be positioned with a 6% overshoot in position compared with a 60% overshoot and significant oscillation when no anti-sway control was used. The control concept was also shown to yield a better positioning response of the suspended load, even if the load is simply moved at a slower speed. Similar to the 1-DOF experiments, here the results indicate again that despite the significant disadvantage of low-cost MEMS sensors in accuracy, linearity, the positioning results obtained using the high-accuracy encoders are almost identical.

3.3.2 Hydraulic manipulator state feedback control

As previously discussed, state feedback control is an effective approach for increasing closed-loop system damping, which leads to a faster, more accurate dynamic response. By using state feedback in the control of the hydraulic actuators of an articulated crane, an improvement in the closed-loop positioning performance of the manipulator end-effector can be achieved. In the previous application, filtered proportional position control was used for controlling actuators of the hydraulic crane. This section presents closed-loop control of the hydraulic crane, for which state feedback control is used instead. The increased closed-loop positioning performance is shown by comparing state feedback control with standard (non-filtered) proportional control using Cartesian path tracking experiments. Additionally, a comparison of the control performance between encoder and MEMS-based motion state feedback is given.

As shown by the experiments of Section 3.2, the direct angular acceleration sensing using the multi-MEMS configuration of Figure 2.6 yields an improved estimate of the angular acceleration in comparison with the differentiated gyro rate (2.32). Thus, the estimate calculated using (2.24) is used to supply the angular acceleration feedback to the state feedback controller. Figure 3.23 illustrates the HIAB 031 manipulator installed on a rigid base with a load mass of 475 kg attached to the end of the manipulator as well as the MEMS sensor configuration. Because the motion is planar, the additional accelerometers at $\{P_i^2\}$ (see Figure 2.6) can be omitted. A similar test setup to Section 3.3.1 concerning the hydraulic valves, cylinder sizes, reference sensors, and real-time control interface was used.

The state feedback controller shown in Figure 1.3 was applied individually to both joints of the manipulator. All coupling effects between the joints were treated as external disturbances to the joint controllers and were subsequently left out of the scope of the experimental study. Although a state-space-based representation similar to the previous experiment might be adopted here for individual actuator control, considering the required extra modelling and measurements of e.g. cylinder chamber pressures, the controller design based on the linear representation of Figure 1.3 is equally applicable. Table 3.9 gives the system parameters for the transfer function (1.1), which were experimentally identified for both joints in the operating region during the motion control experiments. The natural frequency was identified

Table 3.9: HIAB 031 manipulator system parameters.

	ω_n (rad/s)	δ_n (-)	K_{qa} (rad/s)
Joint 1	18	0.05	1.3
Joint 2	18	0.05	1.9

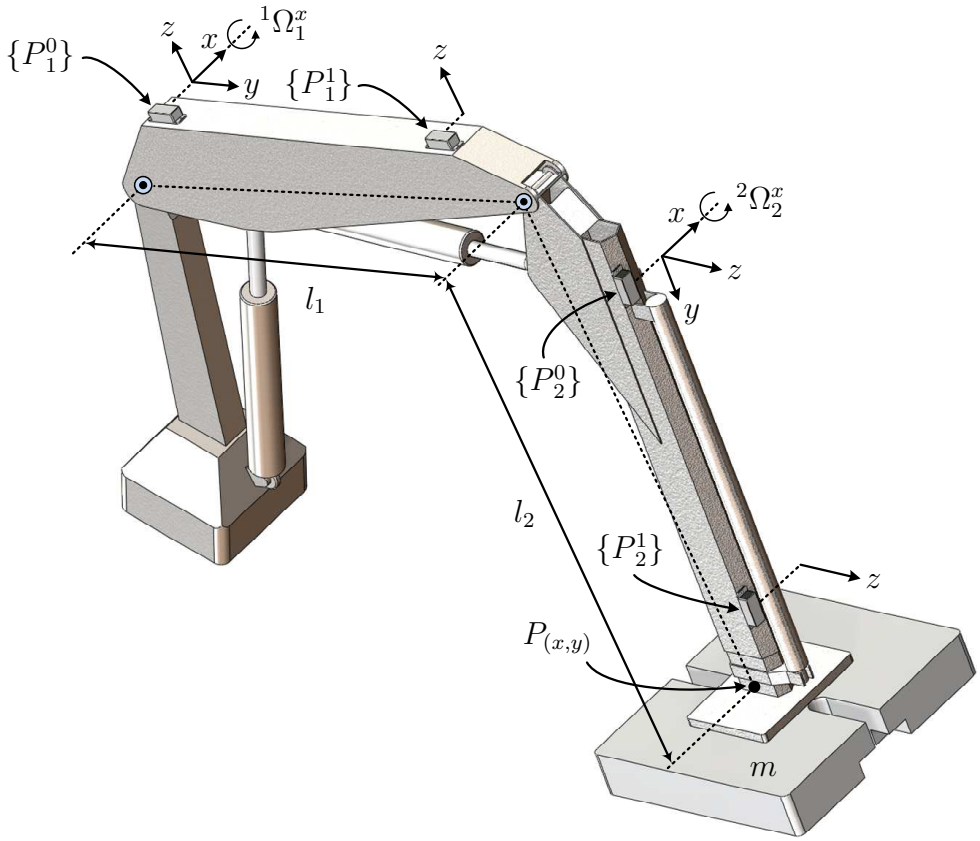

Figure 3.23: MEMS sensor configuration on the hydraulic manipulator. The MEMS sensor positions are ${}^1\mathbf{r}_{P_1^0} = [0\ 0.21\ 0.23]^{\mathrm{T}}$ m, ${}^1\mathbf{r}_{P_1^1} = [0\ 1.33\ 0.16]^{\mathrm{T}}$ m, ${}^1\mathbf{r}_{P_2^0} = [0\ 0.24\ 0.22]^{\mathrm{T}}$ m, and ${}^1\mathbf{r}_{P_2^1} = [0\ 1.32\ 0.145]^{\mathrm{T}}$ m. The link lengths are $l_1 = 1.6$ m and $l_2 = 1.65$ m. The mass is $m = 475$ m. Body frames $\{B_i\}$ are omitted for clarity.

by observing the period of oscillation when the joints were controlled in open-loop and brought to a sudden halt. The natural damping ratio was identified from the decay rate of the oscillation.

As the rated frequency response of the MEMS components extends up to some 50 Hz, several higher-frequency phenomena such as structural vibrations and pressure ripple in the fluid propagating from the hydraulic power unit are present in the accelerometer outputs. Considering the relatively low frequencies of motion of the hydraulic manipulator under study, these high-frequency effects can be safely filtered from the angular acceleration feedback signals without causing control loop instability. For this task the moving average filter with exponentially decaying weights (3.8) was used, for which the value $\gamma = 0.04$ was experimentally identified to yield a suitable compromise between disturbance attenuation and low phase lag. To enable

comparison, the same filter was also applied to the angular acceleration estimated from encoder position with the optimal derivative (3.22).

Figure 3.24 illustrates the resulting acceleration feedback signals when using encoders and MEMS sensors. As can be seen, due to the high sampling rate in relation to the slow angular speeds of the heavy-duty hydraulic manipulator joints, the angular acceleration estimated from the encoder position contains significant noise- and impulse-type perturbations despite the moving average filtering. Additionally, an artificial dead-zone was introduced to the MEMS acceleration signal as the used hydraulic valve has a high bandwidth up to 100 Hz for a $\pm 5\%$ control input, and thus the noise floor of the acceleration signal is translated into valve spool movement. The used angular acceleration dead-zone was set to ± 0.2 rad/s^2, which was also applied to the angular acceleration estimated from encoder position. Recall that these two techniques, the simple geometric moving average noise suppression filtering and the introduction of an artificial dead zone, were found robust in the initial experiments of Section 3.1.

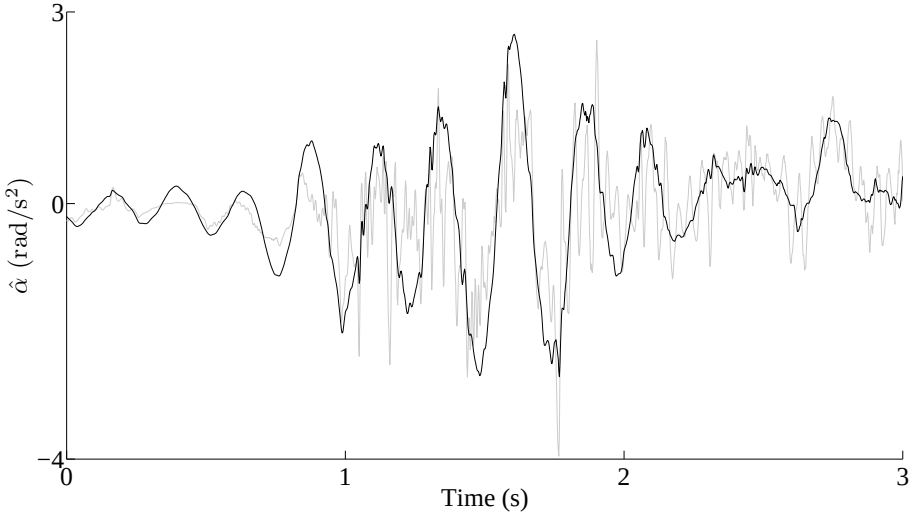

Figure 3.24: Estimated joint angular acceleration $\hat{\alpha}$ during arbitrary motion using encoder feedback (grey line) and MEMS feedback (black line).

As the purpose of the experiments was to demonstrate the usability of low-cost MEMS sensors in hydraulic manipulator motion control, specific controller performance criteria were not defined. Thus, the state controller gains K_p, K_v, and K_a were tuned iteratively by first finding the position gain value K_p for which oscillation begins. Then the gain K_a was increased until the oscillation was removed. After this, the gain K_p could be increased again until the stability limit was reached. However, as shown in (1.3), the use of velocity feedback gain decreases the system damping, and

as the aim is to increase the system damping and control the motion oscillations, the use K_v was omitted. The resulting controller gains are given in Table 3.10. Note that with MEMS-based acceleration feedback, the final value of the feedback gain $K_{a\,\mathrm{mems}}$ is more than doubled compared to the encoder feedback gain $K_{a\,\mathrm{enc}}$. Despite applying the optimal difference operator (3.22) and the moving average filter with exponentially decreasing weights (3.8), the resulting encoder-based angular acceleration still contains large disturbances, as indicated by Figure 3.24. The disturbances limit the maximum stable value of $K_{a\,\mathrm{enc}}$. In view of (1.3), the values in Table 3.10 produce new theoretical values for the natural damping ratios with MEMS feedback as $\delta_{n_1\,mems} \approx 0.64$ and $\delta_{n_2\,mems} \approx 0.39$ for the first and second joint closed-loop transfer function, respectively. With encoder feedback the corresponding damping ratios were $\delta_{n_1\,enc} \approx 0.34$ and $\delta_{n_2\,enc} \approx 0.24$.

Table 3.10: State feedback controller gains.

	K_p	K_v	$K_{a\,\mathrm{enc}}$	$K_{a\,\mathrm{mems}}$
Joint 1	15	0.0	0.025	0.05
Joint 2	10	0.0	0.011	0.02

To be able to determine the effectiveness of state feedback control, a proportional position controller was also implemented, for which the structure is identical to that of Figure 1.3 with the gains K_v and K_a set to zero. The maximum stable gain K_p for the proportional control was identified as $K_p = 5.75$, which was used for both joint controllers and both feedback cases.

The position $P_{(x,y)}$ of the manipulator corresponding to given joint angles ϕ_1 and ϕ_2 can be obtained through the familiar forward kinematics as previously discussed in Section 3.3.1. Figure 3.25 depicts the manipulator workspace allowed by ϕ_1 and ϕ_2 along with the Cartesian path used for the closed-loop motion control experiments. The required manipulator joint angles for the point $P_{(x_d,y_d)}$ travelling along the illustrated path are determined using inverse kinematics in a similar fashion to Section 3.3.1.

The path of the desired point $P_{(x_d,y_d)}$ during each line segment along the rectangular Cartesian path follows the fifth-order polynomial:

$$x_d(t) = r_0^x + r_1^x t + r_2^x t^2 + r_3^x t^3 + r_4^x t^4 + r_5^x t^5 \tag{3.38}$$

$$y_d(t) = r_0^y + r_1^y t + r_2^y t^2 + r_3^y t^3 + r_4^y t^4 + r_5^y t^5, \tag{3.39}$$

which is a rest-to-rest type path (see e.g. Jazar [80]). That is to say, there is no acceleration at the rest points along the path. The polynomial coefficients r_i^x and

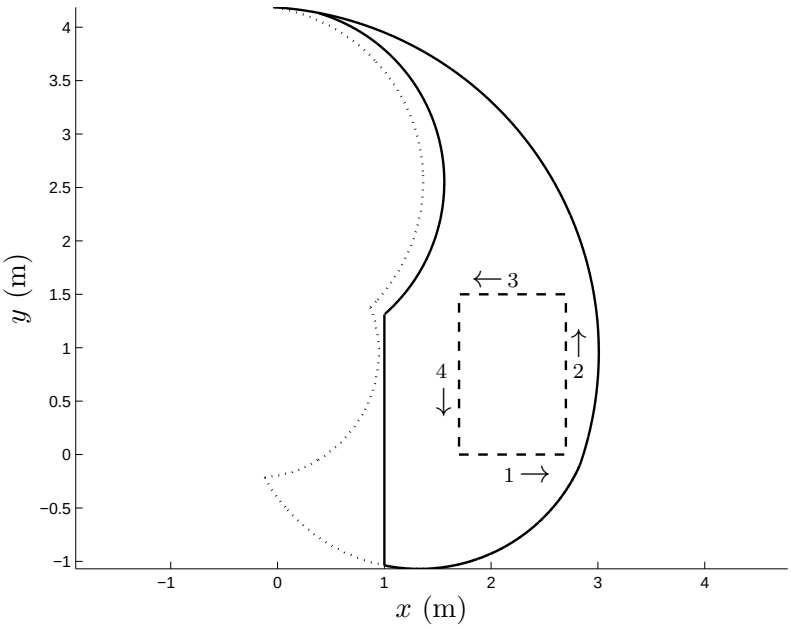

Figure 3.25: HIAB 031 manipulator theoretical workspace (dotted line), available workspace with mass m attached (solid line), and driven Cartesian motion path (dashed line).

r_i^y were calculated to yield a path transition time of $t_d = 3.25$ s between each path segment. Figure 3.26 illustrates the resulting Cartesian velocities of the driven path when using proportional (P) control and state feedback control along with the desired velocity profile of the trajectory. The effect of the acceleration feedback is especially evident in the last segment of the path, during which the considerable velocity oscillation is effectively dampened. The path tracking accuracy of the control schemes can be evaluated using the distance

$$e_c = \sqrt{(x_d - x)^2 + (y_d - y)^2} \tag{3.40}$$

as the tracking error measurement, where x, y is the manipulator position calculated from the encoder joint position readings. The resulting dynamic path following errors are shown in Figure 3.27. Note that despite the nearly 200-fold advantage of the encoders in position resolution, the tracking performance using MEMS position feedback is practically identical. Similarly to state feedback control, the difference in tracking performance between the high-accuracy encoder and the low-cost MEMS approach is very small, with the MEMS feedback yielding occasionally even smaller errors.

The effectiveness of state feedback control is evident in the Cartesian path tracking

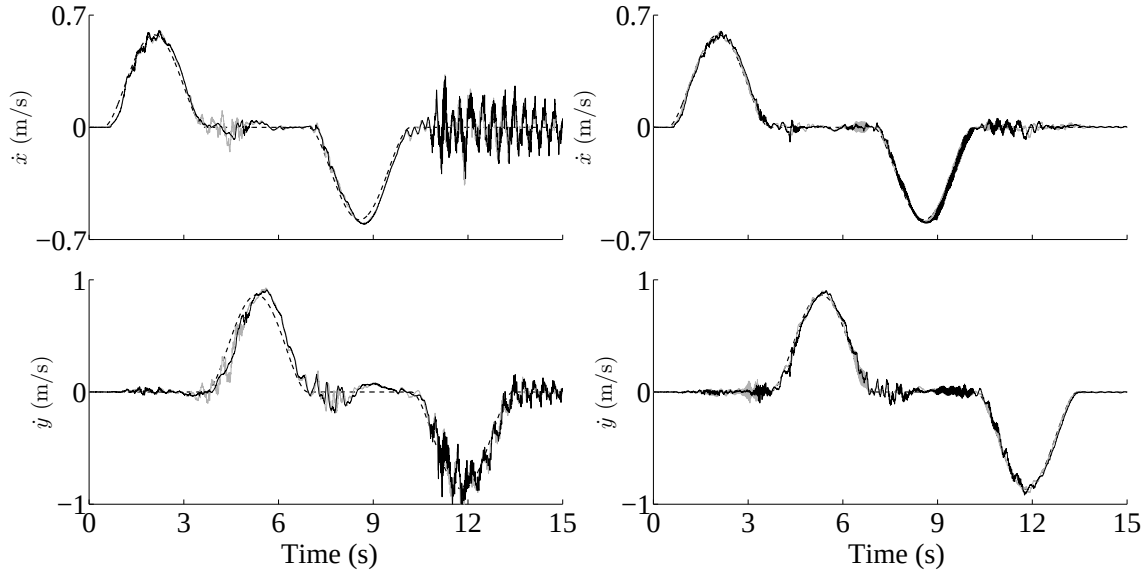

Figure 3.26: Desired Cartesian path x and y velocity (dotted line) with estimated path velocities using P-control (left column) and state feedback control (right column). The feedback source was encoder (grey line) or MEMS (black line).

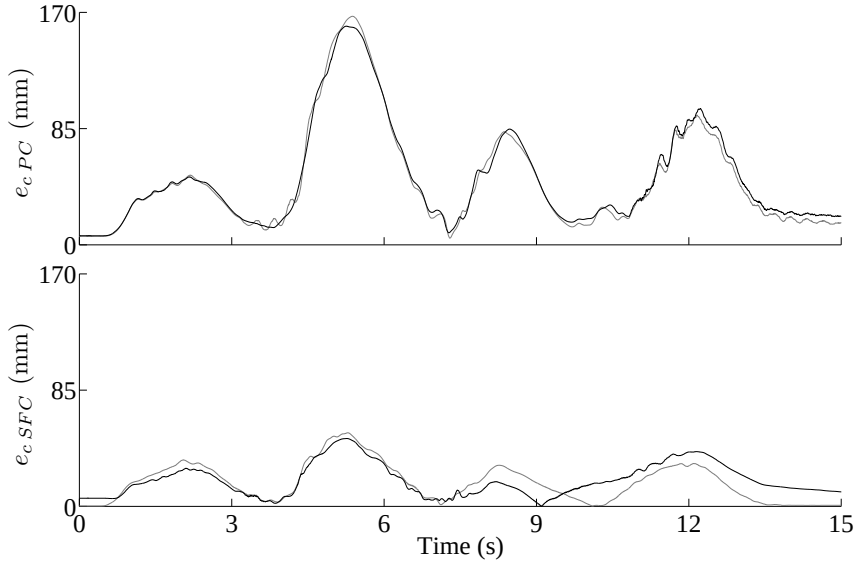

Figure 3.27: P-control Cartesian path tracking error $e_{c\,PC}$ and state feedback control tracking error $e_{c\,SFC}$ using encoder feedback (grey line) and MEMS feedback (black line).

error, which was reduced up to 70% with state feedback control. As indicated by the values in Table 3.10, state feedback allows a considerable increase to the position gain

K_p if compared with proportional position control. This enables a faster dynamic response and a better positioning accuracy. With MEMS feedback, the damping ratio of the hydraulic system was improved by a factor of 7 – 12. Due to the inferior quality of the encoder motion state feedback leading to smaller usable values of K_a, the damping ratio could only be improved by a factor of 5 – 7 when using encoder feedback. As a key result, the tracking accuracy of manipulator position control with the low-cost MEMS motion state estimation approach gives closely comparable results to those of using expensive high-accuracy encoders.

Chapter 4

Discussion

The exclusive original experimental results have shown conclusively that despite the disadvantages of low-cost MEMS sensors in resolution, accuracy, and linearity, they provide a feasible solution to the full motion state sensing of multi-link hydraulic manipulators, and most notably, that high-cost rotary encoders with orders of magnitude higher angular resolutions provide only a marginal improvement in closed-loop control performance. In particular, the ability of MEMS inertial sensors to provide low-noise and low-delay feedback of angular velocity and acceleration, which is essential for high-performance manipulator motion control, cannot be easily matched with traditional encoder-type sensors. It should restated though, that due to the noise characteristics and motion induced artefacts of raw untreated MEMS inertial sensor readings, sensor fusion and kinematic modelling are a prerequisite for using MEMS inertial sensors to supply smoothed, low-delay, and low-noise motion state feedback for a serial-link manipulator control system. However, the required manipulator-specific kinematic parameters consist merely of link lengths and the positions of the MEMS sensors with respect to the joint centres, making the solution easily applicable to various manipulator types. This also means that the motion state estimation is not limited to hydraulic manipulators, but is equally applicable to manipulators with electric or pneumatic actuators, for example. Moreover, because the motion state estimation does not rely on dynamic modelling, as would be the case with state observer-type approaches, the solution is invariant to system parameter variation and changes in the operating point.

The performance characterisation of the MEMS-based motion state estimation model in a three-link test bench showed sensing errors for all three joints positions well within ± 1 degree with an RMS value of 0.16 degrees when the components were subjected to dynamic motions close to their saturation limits. Although a component-dependent value, the results indicate a high degree of correspondence between the motion state

estimation model and the kinematics of a multi-link manipulator system, and that the complementary filter is very successful in combining the redundant noisy inertial measurements. The results can be seen as a notable improvement to existing works on MEMS-based motion sensing, of which for example Brigante et al. [52], Wang et al. [69], Ghassemi et al. [71], and El-Gohary and McNames [21] report peak joint sensing errors from 2.5 to 10 degrees. Conversely, RMS error values ranging from 1 to 5.5 degrees are reported by Quigley et al. [20], Lee et al. [53], Roan et al. [66], Dejnabadi et al. [68], and Petruska and Meek [57]. The improved results can be largely explained by the kinematic modelling underlying the motion compensation of the accelerometer readings – a process which effectively drives the motion disturbance effects close to a zero-mean random process. Although the motion compensated accelerometer readings contain an increased amount of high-frequency perturbations as a result, together with the gyroscope angular velocity measurements they represent redundant noisy measurements of the same rotation. The complementary filter is then able to successfully reconstruct the joint position, while making no assumptions about the statistics or linearity of its input signals. Conversely, this means that without kinematic modelling the accelerometer-based inclination references would become corrupted by motion, and if allowed to enter the complementary filter, would nullify the principle of complementary readings of the same rotation. In this case the filter output (position) would give highly erroneous readings and exhibit drift. The feedback type complementary filter structure adopted in this thesis ensures that the integrated gyroscope angular velocity does not drift unbounded, given that the accelerometer inclination reference provides a redundant measurement of the same rotation. Thus, if only accelerometers are used as a complementary sensor for the gyroscope, the only limitation is that the joint axis of rotation must not become parallel to gravity.

As case examples of applicability for control systems, the MEMS-based full motion state estimation, which contains the first- and second-order time derivatives of motion, was applied to the state feedback control of a hydraulic single-axis boom and a three-link manipulator, and to realising a suspended load anti-sway control system. The preliminary single-axis experiments indicated that the MEMS-based state feedback control performs in a stable manner and yields an increase in control performance, which is mainly limited only by the MEMS sensor output linearity and noise specifications. The state feedback control results on the three-link manipulator showed only a marginal difference in positioning accuracy between the low-cost MEMS-sensors and the high-cost, high-accuracy rotary encoders. Similar to the initial single-axis experiments, clear improvement in control performance was shown, when acceleration feedback was used. This suggests, that the proposed direct angular acceleration sensing is a feasible solution for control systems requiring acceleration feedback, and that it effectively avoids the problems of e.g. noise amplification and

quantization, which Han et al. [29] and Sirouspour and Salcudean [32], among others, report as grounds for avoiding acceleration feedback altogether. With the anti-sway control system, the results showed substantial reduction of uncontrolled load oscillation with a simultaneous capability for load positioning control. In comparison with high-cost rotary-type encoders, the control results were almost identical. Notably, the bias-corrected gyroscope reading provided a direct, differentiation-free solution for the suspended load angular velocity sensing, which has been reported as a main hindrance to the realisation of such systems (see e.g. Neupert et al. [42]). Generally speaking, the combined results point clearly towards the conclusion, that the restrictions encountered by e.g. Keskinen et al. [13] and Cheng et al. [14] in applying traditional encoder-type sensors to hydraulic manipulators can be effectively circumvented.

Although the experimental verification of the motion estimation model was limited to 1-DOF rotary joint motion, in a full 3-DOF case the MEMS error propagation is founded on the exact same principles without loss of generality. In other words, the complementary filtering principle can readily be extended to encompass all three degrees of rotational freedom (see Mahony et al. [61]). Note, however, that with a completely generic multi-DOF manipulator system, two fundamental challenges arise. Firstly, with a typical setup consisting of a low-cost three-axis linear accelerometer and a three-axis gyroscope, only 2-DOF gravity-referenced attitude sensing of a body is feasible. This is to say that only two of the three degrees of rotational freedom are typically defined as, for example, optional sensors such as magnetometers are often of little use in built environments and in the immediate vicinity of metallic manipulator structures (see Caruso [64]). However, using a supplementary absolute positioning system extends the 2-DOF gravity-referenced kinematics to fully defined 3-DOF rotation estimation by applying the previously discussed data fusion principles. Whether or not the force of gravity is used as a reference, the performance of angular rate gyroscopes becomes vital for producing smoothed rotation feedback. Secondly, estimating the linear motion of manipulator links connected by prismatic joints is extremely challenging with low-cost inertial sensors. Even though this area of research is not typically associated with inertial sensors, the possibility of formulating an inverse problem for estimating an unknown link length from sensed linear accelerations exists (see Vihonen et al. [91]). Generally speaking, regardless of the underlying technological solution, resolving the unique instantaneous 3-DOF link rotation or a prismatic joint position without a direct contact to sliding mechanisms is fundamentally dependent on the utilisation of an auxiliary reference measurement, which may come from virtually any type of complementary source.

Chapter 5

Conclusion

Low-cost, low-power, and relatively low-resolution miniature MEMS inertial sensors can be successfully applied to the motion state sensing and motion control of heavy-duty manipulators when the solution is founded on a solid theoretical framework of motion kinematics and signal processing. The proposed motion state estimation model has been shown to yield results comparable to traditional high-cost rotary-type encoders, and to excel in particular in the estimation of the first- and second-order motion derivatives. The experiments on full-scale heavy-duty hydraulic manipulators also demonstrate that a closed-loop motion control system based on the proposed estimation model performs in a stable manner with very similar tracking performance in comparison with traditional sensing solutions. Due to the generic nature of the estimation model, it is easy to apply to a variety of manipulator geometries by adjusting the kinematic parameters. From the control perspective, the results indicate that the gap between traditional encoder-type and surface-mountable inertial sensors may well fade away in the near future. In practice, this also strongly suggests that advanced robotic motion control systems for heavy-duty hydraulic manipulators may be constructed using low-cost inertial components, if the components are merely integrated to the manipulator structure in robust enclosures. This is of great practical relevance, because the design constraints imposed by traditional encoder-type sensors may now be excluded from manipulator joint design. This allows the focus to shift back to exerted forces and torques while excluding the needs of external shielding for axial sensors, for example.

For mobile machine manufacturers the results imply reduced design effort, lower cost, easy replacement of damaged motion sensors, and increased sensor robustness against the harsh environmental working conditions of mobile working machines. More robust sensors decrease the likelihood of experienced production down-time, and make the introduction of new advanced safety- and productivity-boosting robotic

features feasible. As a consequence, Finnish mobile machine manufacturers will be able to realise innovative solutions for advanced robotic control, condition monitoring, and fault diagnostic systems using low-cost, easy-to-install motion sensors to gain an advantage on the increasingly competitive global market. Additionally, a particular benefit of the novel technology is the possibility for developing more intuitive heavy-duty hydraulic manipulators control systems, which assist the operator while simultaneously making the manipulator operation less prone to human errors.

In the pursuit of increased productivity and efficient manipulator use, the goal is to attain optimal operation speed and loading configuration of the manipulator for each material handling task while maintaining operational safety. Combining low-cost surface mountable inertial sensors with supplementary ranging/positioning or even imaging solutions may be the next important step in this direction. The adoption of these technologies fits particularly well with current research and development interests, which are strongly geared towards the adaptation of wireless technologies for manipulator motion state sensing. For instance, a key objective is to phase out the failure-prone cable assemblies and routings needed for traditional wired sensors. Further research objectives can be seen in the ever-increasing demands for energy-efficiency, which ultimately call for the development of energy self-sufficient, wireless sensing solutions, which rely on various forms of energy-harvesting. As far as the author believes, this constitutes a foreseeable key research area in the field of heavy-duty mobile manipulators.

Bibliography

[1] A. K. Jardine, D. Lin, and D. Banjevic, "A review on machinery diagnostics and prognostics implementing condition-based maintenance," *Mechanical Systems and Signal Processing*, vol. 20, no. 7, pp. 1483–1510, Oct. 2006.

[2] Y. Peng, M. Dong, and M. J. Zuo, "Current status of machine prognostics in condition-based maintenance: a review," *The International Journal of Advanced Manufacturing Technology*, vol. 50, no. 1–4, pp. 297–313, Sep. 2010.

[3] R. Lovgren, "Radical improvements in crane safety," *ISO Focus*, vol. 1, no. 7, pp. 21–23, Jul./Aug. 2004.

[4] J. Saarinen, J. Suomela, and A. Halme, "The concept of future worksite - towards teamwork-centered field robotic systems," in *18th International Federation of Automatic Control World Congress (IFAC)*, Milano, Italy, Aug./Sep. 2011, pp. 14 952–14 957.

[5] E. Halbach and A. Halme, "Job planning and supervisory control for automated earthmoving using 3d graphical tools," *Automation in Construction*, vol. 32, pp. 145–160, Jul. 2013.

[6] I. Bergkvist, B. Nordén, and H. Lundström, "Innovative unmanned harvester system," Skogforsk (the forestry research institute of Sweden), Skogforsk Results 2, 2006.

[7] U. Hallonborg, "Unmanned forestry machines can be competitive," Skogforsk (the forestry research institute of Sweden), Skogforsk Results 4, 2003.

[8] J. Billingsley, A. Visala, and M. Dunn, "Robotics in agriculture and forestry," in *Springer Handbook of Robotics*, B. Siciliano and O. Khatib, Eds. Berlin Heidelberg: Springer, 2008, ch. 46, pp. 1065–1077.

[9] O. Ringdahl, "Automation in forestry: development of unmanned forwarders," Ph.D. dissertation, Umeå University, 2011.

[10] T. Hellström, P. Lärkeryd, T. Nordfjell, and O. Ringdahl, "Autonomous forest

vehicles: Historic, envisioned, and state-of-the-art," *International Journal of Forest Engineering*, vol. 20, no. 1, pp. 31–38, Jan. 2009.

[11] K. Berns, K.-D. Kuhnert, and C. Armbrust, "Off-road robotics - an overview," *KI - Künstliche Intelligenz*, vol. 25, no. 1, pp. 109–116, May 2011.

[12] C. Zhang and A. Hammad, "Improving lifting motion planning and re-planning of cranes with consideration for safety and efficiency," *Advanced Engineering Informatics*, vol. 26, no. 2, pp. 396–410, Apr. 2012.

[13] E. Keskinen, S. Launis, and M. Cotsaftis, "Performance analysis of drive-line steering methods in excavator-mounted sheet-piling systems," *Computer-Aided Civil and Infrastructure Engineering*, vol. 16, no. 4, pp. 229–238, Jul. 2001.

[14] P. Cheng, B. Oelmann, and F. Linnarsson, "A local positioning system for loader cranes based on wireless sensors - a feasibility study," *IEEE Transactions on Instrumentation and Measurement*, vol. 60, no. 8, pp. 2881–2893, Aug. 2011.

[15] Dr. Johannes Heidenhain GmbH, "Rotatory encoders," www.heidenhain.de, Nov. 2011.

[16] *Transducer Catalog - Linear Position Transducers*, Balluff GmbH, 2013, www.balluff.com.

[17] D. Giansanti, G. Maccioni, and V. Macellari, "The development and test of a device for the reconstruction of 3-D position and orientation by means of a kinematic sensor assembly with rate gyroscopes and accelerometers," *IEEE Transactions on Biomedical Engineering*, vol. 52, no. 7, pp. 1271–1277, Jul. 2005.

[18] H. Luinge and P. Veltink, "Measuring orientation of human body segments using miniature gyroscopes and accelerometers," *Medical & Biological Engineering & Computing*, vol. 43, no. 2, pp. 273–282, 2005.

[19] H. Luinge, P. Veltink, and C. Baten, "Ambulatory measurement of arm orientation," *Journal of Biomechanics*, vol. 40, no. 1, pp. 78–85, 2007.

[20] M. Quigley, R. Brewer, S. P. Soundararaj, V. Pradeep, Q. Le, and A. Y. Ng, "Low-cost accelerometers for robotic manipulator perception," in *IEEE/RSJ International Conference on Intelligent Robots and Systems*, Taipei, Taiwan, Oct. 2010, pp. 6168–6174.

[21] M. El-Gohary and J. McNames, "Shoulder and elbow joint angle tracking with inertial sensors," *IEEE Transactions on Biomedical Engineering*, vol. 59, no. 9, pp. 2635–2641, Sep. 2012.

[22] Novatron Oy, "Novatron excavator control systems," www.novatron.fi/en, Nov. 2013.

[23] Scanlaser Oy, "Scanlaser machine control solutions," http://www.scanlaser.fi/, Nov. 2013.

[24] J. Watton, *Fluid Power Systems : modelling, simulation, analog and microcomputer control*. New York: Prentice Hall, 1989.

[25] R. Dorf and R. Bishop, *Modern Control Systems*. Upper Saddle River, NJ: Pearson, 2011.

[26] M. Jelali and A. Kroll, *Hydraulic Servo Systems: modelling, identification and control*, ser. Advances in industrial control. London: Springer, 2003.

[27] K. Åström and T. Hägglund, *PID Controllers: Theory, Design, and Tuning*, 2nd ed. Instrument Society of America, 1995.

[28] R. Rahmfeld and M. Ivantysynova, "An overview about active oscillation damping of mobile machine structure," *International Journal of Fluid Power*, vol. 5, no. 2, pp. 5–25, 2004.

[29] J. Han, Y. He, and W. Xu, "Angular acceleration estimation and feedback control: An experimental investigation," *Mechatronics*, vol. 17, no. 9, pp. 524–532, Nov. 2007.

[30] A. Muhammad, J. Mattila, T. Virvalo, and M. Vilenius, "Improved positioning accuracy for a water hydraulic manipulator with state feedback controller," in *Service Robotics and Mechatronics*. Springer, 2010, pp. 347–352.

[31] Z. Jabbour, S. Moreau, A. Riwan, J. V. Rhijn, and G. Champenois, "Influence of speed estimation methods and encoder resolutions on the stiffness of a haptic interface," in *IEEE International Symposium on Industrial Electronics (ISIE)*, Jul. 2010, pp. 1883–1888.

[32] M. R. Sirouspour and S. E. Salcudean, "Nonlinear control of hydraulic robots," *IEEE Transactions on Robotics and Automation*, vol. 17, no. 2, pp. 173–182, Apr. 2001.

[33] L. Zhai, "Modelling and robust control of hydraulic manipulators," Ph.D. dissertation, Tampere University of Technology, 2012.

[34] Y. Pi and X. Wang, "Trajectory tracking control of a 6-DOF hydraulic parallel robot manipulator with uncertain load disturbances," *Control Engineering Practice*, vol. 19, no. 2, pp. 185–193, Feb. 2011.

[35] R. J. E. Merry, M. J. G. van de Molengraft, and M. Steinbuch, "Velocity and acceleration estimation for optical incremental encoders," *Mechatronics*, vol. 20, no. 1, pp. 20 – 26, Feb. 2010.

[36] S. J. Ovaska and S. Väliviita, "Angular acceleration measurement: A review," *IEEE Transactions on Instrumentation and Measurement*, vol. 47, no. 5, pp. 1211 – 1217, Oct. 1998.

[37] A. J. L. Harrison and D. P. Stoten, "Generalized finite difference methods for optimal estimation of derivatives in real-time control problems," *Proc. Inst. Mech. Eng. Part I - Journal of Systems and Control Engineering*, vol. 209, no. 2, pp. 67 – 78, May 1995.

[38] M. K. Bak, M. R. Hansen, and H. R. Karimi, "Robust tool point control for offshore knuckle boom crane," in *Proc. of the 18th IFAC World Congress*, Milano, Italy, Aug./Sep. 2011, pp. 4594 – 4599.

[39] M. B. Kjelland, I. Tyapin, G. Hovland, and M. R. Hansen, "Tool-point control for a redundant heave compensated hydraulic manipulator," in *Proc. of the 2012 IFAC Workshop on Automatic Control in Offshore Oil and Gas Production*, Trondheim, Norway, May/Jun. 2012, pp. 299 – 304.

[40] M. B. Kjelland, M. R. Hansen, I. Tyapin, and G. Hovland, "Tool-point control of a planar hydraulically actuated manipulator with compensation of non-actuated degree of freedom," in *12th Int. Conf. on Control, Automation and Systems (ICCAS)*, Jeju Island, Korea, Oct. 2012, pp. 672 – 677.

[41] Y.-S. Kim, H. Shim, H. Yoshihara, N. Fujioka, H. Kasahara, and S.-K. Sul, "A new vision-sensorless anti-sway control system for container cranes," in *Conference Record of the Industry Applications Conference, 38th IAS Annual Meeting*, Oct. 2003, pp. 262 – 269.

[42] J. Neupert, E. Arnold, K. Schneider, and O. Sawodny, "Tracking and anti-sway control for boom cranes," *Control Engineering Practice*, vol. 18, no. 1, pp. 31 – 44, Jan. 2010.

[43] K. L. Sorensen, W. Singhose, and S. Dickerson, "A controller enabling precise positioning and sway reduction in bridge and gantry cranes," *Control Engineering Practice*, vol. 15, no. 7, pp. 825 – 837, Jul. 2007.

[44] S. Garrido, M. Abderrahim, A. Giménez, R. Diez, and C. Balaguer, "Anti-swinging input shaping control of an automatic construction crane," *IEEE Trans. Automation Science and Engineering*, vol. 5, no. 3, pp. 549 – 557, Jul. 2008.

[45] M. A. Ahmad, R. M. T. R. Ismail, and M. S. Ramli, "Input shaping techniques for anti-sway control of a 3-D gantry crane system," in *Proc. of the IEEE Int. Conf. on Mechatronics and Automation*, China, Aug. 2009, pp. 2876 – 2881.

[46] J. Vaughan, A. Karajgikar, and W. Singhose, "A study of crane operator performance comparing PD-control and input shaping," in *American Control Conference*, San Fransisco, CA, USA, Jun./Jul. 2011, pp. 545 – 550.

[47] S. Łuczak, W. Oleksiuk, and M. Bodnicki, "Sensing tilt with MEMS accelerometers," *IEEE Sensors Journal*, vol. 6, no. 6, pp. 1669 – 1675, Dec. 2006.

[48] I. Frosio, F. Pedersini, and N. A. Borghese, "Autocalibration of MEMS accelerometers," *IEEE Transactions on Instrumentation and Measurement*, vol. 58, no. 6, pp. 2034 – 2041, Jun. 2009.

[49] J. K. Bekkeng, "Calibration of a novel MEMS inertial reference unit," *IEEE Transactions on Instrumentation and Measurement*, vol. 58, no. 6, pp. 1967 – 1974, Jun. 2009.

[50] P. Aggarwala, Z. Syed, X. Niu, and N. El-Sheimy, "A standard testing and calibration procedure for low cost MEMS inertial sensors and units," *Journal of Navigation*, vol. 61, no. 2, pp. 323 – 336, Apr. 2008.

[51] A. Amirsadri, J. Kim, L. Petersson, and J. Trumpf, "Practical considerations in precise calibration of a low-cost MEMS IMU for road-mapping applications," in *IEEE/RSJ International Conference on Intelligent Robots and Systems*, Montréal, Canada, Jun. 2012, pp. 881 – 888.

[52] C. M. N. Brigante, N. Abbate, A. Basile, A. C. Faulisi, and S. Sessa, "Towards miniaturization of a MEMS-based wearable motion capture system," *IEEE Transactions on Industrial Electronics*, vol. 58, no. 8, pp. 3234 – 3241, Aug. 2011.

[53] J. K. Lee, E. J. Park, and S. N. Robinovitch, "Estimation of attitude and external acceleration using inertial sensor measurement during various dynamic conditions," *IEEE Transactions on Instrumentation and Measurement*, vol. 61, no. 8, pp. 2262 – 2273, Aug. 2012.

[54] R. Zhu and Z. Zhou, "A real-time articulated human motion tracking using tri-axis inertial/magnetic sensors package," *IEEE Transactions on Neural Systems and Rehabilitation Engineering*, vol. 12, no. 2, pp. 295 – 302, 2004.

[55] R. Zhu, D. Sun, Z. Zhou, and D. Wang, "A linear fusion algorithm for attitude determination using low cost MEMS-based sensors," *Measurement*, vol. 40, no. 3, pp. 322 – 328, 2007.

[56] J. Leavitt, A. Sideris, and J. Bobrow, "High bandwidth tilt measurement using

low-cost sensors," *IEEE/ASME Transactions on Mechatronics*, vol. 11, no. 3, pp. 320 – 327, Jun. 2006.

[57] A. J. Petruska and S. G. Meek, "Non-drifting limb angle measurement relative to the gravitational vector during dynamic motions using accelerometers and rate gyros," in *IEEE/RSJ International Conference on Intelligent Robots and Systems*, San Francisco, CA, USA, Sep. 2011, pp. 3632 – 3637.

[58] R. G. Brown and P. Y. C. Hwang, *Introduction to random signals and applied Kalman filtering.* New York, NY: Wiley, 1997.

[59] M. S. Weinberg, C. Wall, J. Robertsson, E. O'Neil, K. Sienko, and R. Fields, "Tilt determination in MEMS inertial vestibular prosthesis," *Journal of Biomechanical Engineering*, vol. 128, no. 6, pp. 943 – 956, Dec. 2006.

[60] D. Kubus, C. G. L. Bianco, and F. M. Wahl, "A sensor fusion approach to improve joint angle and angular rate signals in articulated robots," in *IEEE/RSJ International Conference on Intelligent Robots and Systems*, Vilamoura, Algarve, Portugal, Oct. 2012, pp. 2736 – 2741.

[61] R. Mahony, T. Hamel, and J.-M. Pflimlin, "Nonlinear complementary filters on the special orthogonal group," *IEEE Transactions on Automatic Control*, vol. 53, no. 5, pp. 1203 – 1218, Jun. 2008.

[62] M. Euston, P. Coote, R. Mahony, J. Kim, and T. Hamel, "A complementary filter for attitude estimation of a fixed-wing UA," in *IEEE/RSJ International Conference on Intelligent Robots and Systems*, Nice, France, Sep. 2008, pp. 340 – 345.

[63] H. Fourati, N. Manamanni, L. Afilal, and Y. Handrich, "Complementary observer for body segments motion capturing by inertial and magnetic sensors," *IEEE/ASME Transactions on Mechatronics*, 2014, (to appear).

[64] M. J. Caruso, "Applications of magnetic sensors for low cost compass systems," in *IEEE Position Location and Navigation Symposium*, San Diego, CA, USA, Mar. 2000, pp. 177 – 184.

[65] D. Roetenberg, H. J. Luinge, C. T. M. Baten, and P. H. Veltink, "Compensation of magnetic disturbances improves inertial and magnetic sensing of human body segment orientation," *IEEE Transactions on Neural Systems and Rehabilitation Engineering*, vol. 13, no. 3, pp. 395 – 405, Sep. 2005.

[66] P. Roan, N. Deshpande, Y. Wang, and B. Pitzer, "Manipulator state estimation with low cost accelerometers and gyroscopes," in *IEEE/RSJ International*

Conference on Intelligent Robots and Systems, Vilamoura, Algarve, Portugal, Oct. 2012, pp. 4822 – 4827.

[67] P. Cardou, G. Fournier, and P. Gagnon, "A nonlinear program for angular-velocity estimation from centripetal-acceleration measurements," *IEEE/ASME Transactions on Mechatronics*, vol. 16, no. 5, pp. 932 – 944, Oct. 2011.

[68] H. Dejnabadi, B. M. Jolles, and K. Aminian, "A new approach to accurate measurement of uniaxial joint angles based on a combination of accelerometers and gyroscopes," *IEEE Transactions on Biomedical Engineering*, vol. 52, no. 8, pp. 1478 – 1484, Aug. 2005.

[69] Y. Wang, W. Chen, and M. Tomizuka, "Extended kalman filtering for robot joint angle estimation using mems inertial sensors," in *Proceedings of the 6th IFAC Symposium on Mechatronic Systems*, Hangzhou, China, Apr. 2013, pp. 406 – 413.

[70] P. Cheng and B. Oelmann, "Joint-angle measurement using accelerometers and gyroscopes - a survey," *IEEE Transactions on Instrumentation and Measurement*, vol. 59, no. 2, pp. 404 – 414, Feb. 2010.

[71] F. Ghassemi, S. Tafazoli, P. Lawrence, and K. Hashtrudi-Zaad, "Design and calibration of an integration-free accelerometer-based joint-angle sensor," *IEEE Transactions on Instrumentation and Measurement*, vol. 57, no. 1, pp. 150 – 159, Jan. 2008.

[72] M. M. Aref, R. Ghabcheloo, A. Kolu, M. Hyvönen, K. Huhtala, and J. Mattila, "Position-based visual servoing for pallet picking by an articulated-frame-steering hydraulic mobile machine," in *The 6th IEEE International Conference on Robotics, Automation and Mechatronics (RAM)*, Manila, Philippines, Nov. 2013.

[73] Murata Electronics Oy, "SCC1300-D02 combined x-axis gyroscope and 3-axis accelerometer with digital SPI interfaces," www.muratamems.fi, Aug. 2012.

[74] J. Honkakorpi, J. Vihonen, and J. Mattila, "MEMS sensor module for hydraulic boom state feeedback control," in *The Twelfth Scandinavian International Conference on Fluid Power (SICFP'11)*, Tampere, Finland, May 2011, pp. 393 – 404.

[75] J. Honkakorpi, J. Vihonen, and J. Mattila, "Sensor module for hydraulic boom state feedback control," *International Journal of Fluid Power*, vol. 13, no. 3, pp. 15 – 23, Nov. 2012.

[76] J. Honkakorpi, J. Vihonen, and J. Mattila, "MEMS sensor network based anti-sway control system for articulated hydraulic crane," in *ASME/BATH 2013*

Symposium on Fluid Power & Motion Control, Sarasota, Florida, USA, Oct. 2013.

[77] J. Honkakorpi, J. Vihonen, and J. Mattila, "MEMS-based state feedback control of multi-body hydraulic manipulator," in *IEEE/RSJ International Conference on Intelligent Robots and Systems (IROS)*, Tokyo, Japan, Nov. 2013, pp. 4419–4425.

[78] J. Vihonen, J. Honkakorpi, J. Mattila, and A. Visa, "Geometry-aided MEMS motion state estimation for multi-body manipulators," in *IEEE/ASME International Conference on Advanced Intelligent Mechatronics (AIM)*, Wollongong, Australia, Jul. 2013, pp. 341–347.

[79] J. Vihonen, J. Honkakorpi, J. Mattila, and A. Visa, "Geometry-aided angular acceleration sensing of rigid multi-body manipulator using MEMS rate gyros and linear accelerometers," in *IEEE/RSJ International Conference on Intelligent Robots and Systems (IROS)*, Tokyo, Japan, Nov. 2013, pp. 2514–2520.

[80] R. N. Jazar, *Theory of Applied Robotics: Kinematics, Dynamics, and Control*, 2nd ed. Springer, 2010.

[81] L. Sciavicco and B. Siciliano, *Modeling and Control of Robot Manipulators*. London: Springer, 2000.

[82] J. Denavit and R. Hartenberg, "A kinematic notation for lower-pair mechanisms based on matrices," *Journal of Applied Mechanics*, vol. 22, no. 2, pp. 215–221, Jun. 1955.

[83] A. J. Padgaonkar, K. W. Krieger, and A. I. King, "Measurement of angular acceleration of a rigid body using linear accelerometers," *Journal of Applied Mechanics*, vol. 42, no. 3, pp. 552–556, Sep. 1975.

[84] F. L. Markley, "Attitude determination using vector observations and the singular value decomposition," *Journal of the Astronautical Sciences*, vol. 38, no. 3, pp. 245–258, 1988.

[85] W. T. Higgins, "A comparison of complementary and Kalman filtering," *IEEE Transactions on Aerospace and Electronic Systems*, vol. 11, no. 3, pp. 321–325, 1975.

[86] S. Roberts, "Control charts based on geometric moving averages," *Technometrics*, vol. 1, no. 3, pp. 239–250, 1959.

[87] SICK AG, "DGS60, DGS65 and DGS66: Incremental encoders for rough environmental conditions," www.mysick.com, Sep. 2006.

[88] H. Ouyang, N. Uchiyama, and S. Sano, "Suppression of two-dimensional load-sway in rotary crane control using only horizontal boom motion," *Journal of System Design and Dynamics*, vol. 5, no. 4, pp. 535–546, 2011.

[89] L. Beiner and J. Mattila, "An improved pseudoinverse solution for redundant hydraulic manipulators," *Robotica*, vol. 17, no. 2, pp. 173–177, Mar. 1999.

[90] M. Linjama, "The modeling and actuator space control of flexible hydraulic cranes," Ph.D. dissertation, Tampere University of Technology, 1998.

[91] J. Vihonen, J. Honkakorpi, J. Mattila, and A. Visa, "Geometry-aided inversion of manipulator telescopic link length from MEMS accelerometer and rate gyro readings," in *IEEE International Conference on Robotics and Automation (ICRA)*, Hong Kong, China, May/Jun. 2014, (accepted for publication).

Tampereen teknillinen yliopisto
PL 527
33101 Tampere

Tampere University of Technology
P.O.B. 527
FI-33101 Tampere, Finland

ISBN 978-952-15-3310-5
ISSN 1459-2045